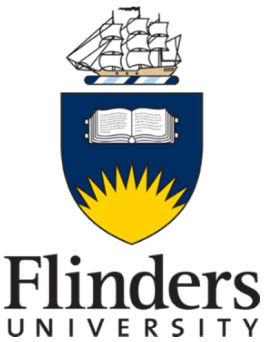

An assessment of transient seawater intrusion processes: physical experiments and numerical modelling

Sugiarto
B.Eng., M.Eng.

School of the Environment
Faculty of Science and Engineering
Flinders University

A thesis submitted for the degree of
Doctor of Philosophy
February, 2017

Table of Contents

LIST OF FIGURES

LIST OF TABLES

SUMMARY

Coastal aquifers are important sources of freshwater for domestic, agricultural and industrial purposes in many countries. Currently, coastal aquifers worldwide are under increasing threat of seawater intrusion (SWI). SWI is a phenomenon where seawater intrudes into a coastal aquifer and contaminates fresh groundwater. The occurrence of SWI is predominantly a human-induced process due to groundwater overexploitation, although natural factors such as sea-level rise (SLR) may also contribute to SWI problems. Other transient factors such as seasonality in recharge and land use change may also affect SWI.

Previous studies identify two different types of SWI: passive and active. Where passive SWI arises from a reduction in the watertable elevation, there will be an accompanying decrease in the depth of freshwater discharging at the shoreline and SWI occurs despite persistent freshwater discharge to the sea, and the seawater wedge intrudes rather slowly. At a certain condition where freshwater discharge to the sea ceases, a transition occurs from passive SWI to active SWI at the shoreline. Active SWI is driven by the combined effects of the density difference between freshwater and seawater, and the inland-sloping hydraulic gradient, whereas under passive SWI, these forces are opposed. The processes associated with active SWI have received considerably less attention compared to situations of passive SWI despite several investigations demonstrating that active SWI is occurring in many areas. It is hypothesized that there will be an extensive salinization under active SWI not only at the lower domain of coastal aquifer but also at the upper domain of coastal aquifer.

In this thesis, numerical modelling and physical experiments are combined to quantitatively and systematically examine transient SWI processes under passive and active SWI situations triggered by a freshwater head decline (FHD). This includes geometry of the freshwater-saltwater interface, width of the mixing zone, flow processes and related effects (e.g., watertable salinization (WTS), advection and density). Investigations consider only the effects of FHD on WTS, because these are expected to develop faster and be larger in magnitude than SLR, and are expected to generate more aggressive SWI situations. Currently, no experimental or numerical

studies exist that provide an assessment of transient active SWI processes while exploring interface characteristics in terms of freshwater-saltwater interface geometry. Consequently, this study provides new insight into transient SWI processes in response to FHD and aims to be a comprehensive guide to active SWI behaviour.

This thesis comprises four sections (Chapters 2-5) that investigate different aspects of the transient SWI processes. Firstly, in Chapter 2, physical experiments and numerical modelling are combined to examine the occurrence of WTS associated with SWI in response to an inland FHD. A comparison of laboratory and numerical modelling results offers insight into both the veracity of the laboratory set up and assumptions of the numerical code. WTS is examined in the absence of tidal effects with a focus on the influence of watertable decline on WTS. An important outcome of this work is SWI can cause WTS in unconfined coastal aquifer setting and may induce unsaturated zone soil salinization in the vicinity of the sea boundary. Numerical models of the laboratory experiments show that significant WTS can occur under active SWI caused by the associated cessation of seaward freshwater discharge while under passive SWI, minor WTS can occur under conditions of increased dispersivity, greater hydraulic conductivity and reduced freshwater discharge to the sea.

Secondly, Chapter 3 includes a SWI study where vertical leakage in layered coastal aquifers is investigated using both a sharp and dispersive interface numerical model in conjunction with a physical model. Here the sharp-interface numerical model examines three cases of SWI in layered aquifers with upward freshwater leakage through aquitards. Case 1 involves freshwater bypassing any overlying saltwater, Case 2 assumes no upward freshwater leakage where there is overlying saltwater and Case 3 converts upward freshwater leakage into saltwater. Steady-state and transient predictions using both sharp-interface and dispersive models are assessed, and compared to the results of sand-tank experiments. Case 1 (i.e., freshwater bypassing any overlying saltwater) produces optimal matches to both numerical simulation results and sand-tank observations in terms of saltwater wedge locations relative to the two other cases. However, sharp-interface models over-predict the extent of saltwater under both steady-state and transient conditions. Streamlines from the

numerical model show that upward freshwater leakage tends to flow around and bypass overlying saltwater.

Thirdly, the work is extended in Chapter 4 by systematically investigating characteristics of active SWI at larger scales, using numerical simulation. This body of work shows that the active SWI response time-scales are affected by both the initial and final boundary head differences between the inland and the sea boundary. The freshwater-saltwater interface is found to be steeper under stronger advection (i.e., caused by the inland FHD), higher dispersivity and hydraulic conductivity, and lower aquifer thickness, seawater density and porosity. The interface movement is faster and the mixing zone is wider with larger hydraulic conductivity, seawater-freshwater density difference and aquifer thickness, and with lower porosity. Advection effects become more dominant on the interface movement relative to density effects as SWI becomes more active. The results also show that dimensionless parameters (Peclet number and mixed convection ratio) from previous steady-state analyses offer only limited application to the controlling factors of passive SWI, and are not applicable to active SWI.

Finally, the analysis of SWI is expanded in Chapter 5 by conducting a regional three-dimensional modelling investigation of a real-world SWI case. In this work, SEAWAT is used to model the coastal aquifer conditions that occur in Uley South Basin (USB), South Australia. Numerical experiments are performed with a regional three-dimension SWI model of USB that adopts spatial heterogeneity parameters obtained from a prior calibration effort using a single-density model. The aim of this work is to examine the individual relative contribution of climate variability and anthropogenic stresses on the extent of seawater in USB. Also, the effects of buoyancy and seawater extent on groundwater head behaviour near the coast are explored. The experiments reveal that aquifer pumping has greater impact on the extent of SWI in the Quaternary Limestone (QL) and Tertiary Sand (TS) layers of USB, in comparison to SWI arising from climate variability. The numerical simulations further demonstrate that inclusion of seawater in the model modifies the groundwater behaviour near the coast where the effects of aquifer stresses on groundwater head response are larger compared to those where seawater is absent.

DECLARATION OF ORIGINALITY

I certify that this thesis does not incorporate without acknowledgment any material previously submitted for a degree or diploma in any university; and that to the best of my knowledge and belief it does not contain any material previously published or written by another person except where due reference is made in the text.

.....
Sugiarto Badaruddin
27 - 02 - 2017

STATEMENT OF CONTRIBUTIONS TO A JOINTLY AUTHORED WORK CONTAINED IN THE THESIS

Mehdizadeh, S. S., A. D. Werner, F. Vafaie, and S. Badaruddin (2014). Vertical leakage in sharp-interface seawater intrusion models of layered coastal aquifers. Journal of Hydrology 519: 1097-1107. – S. Sadjad Mehdizadeh was responsible for 75% of conception and design, 75% of laboratory experiments, 75% of numerical simulation's execution, 75% of analysis and interpretation of data and 75% of drafting and writing; Adrian D. Werner was responsible for for 10% of conception and design, 5% of laboratory experiments, 0% of numerical simulation's execution, 10% of analysis and interpretation of data and 15% of drafting and writing; Freydoon Vafaie was responsible for 5% of conception and design, 0% of laboratory experiments, 0% of numerical simulation's execution, 5% of analysis and interpretation of data and 0% of drafting and writing; Sugiarto Badaruddin was responsible for 10% of conception and design, 20% of laboratory experiments, 25% of numerical simulation's execution, 10% of analysis and interpretation of data and 10% of drafting and writing.

ACKNOWLEDGEMENTS

My acknowledgement begins with my gratitude to my God for giving me a chance to finish my PhD at Flinders University. Secondly, I would like to acknowledge my mother (Hj. Hasnah Sinring), my father (H. Badaruddin Kamming), and of course my wife (Asniar Hafid), my children (Salwa Shofiyah and Syahid Abdillah), my siblings (Hj. Fitriani Badaruddin, Ariyanto Badaruddin and Muriyanto Badaruddin) for giving me a limitless support throughout this tough PhD journey.

I must also humbly acknowledge and thank my principal supervisor, Prof. Adrian D. Werner, my co-supervisors, Dr Leanne K. Morgan and Prof. Craig T. Simmons. Adrian Werner and Leanne Morgan have provided me not only with continuous support and guidance, but also with a model professionalism and humanity that I felt throughout this research project. Craig Simmons, for his great support and guidance at initial stages of my PhD. I would also like to thank all my colleagues (Dr Tariq Laattoe, Andrew Knight, Hannah Sharp and Jason Thomann) for the good time we spent together during my PhD at Flinders University.

And lastly, I would like to thank Australia Awards Scholarships for funding my study and thanks also to AusAid liaison officers (especially to Jane Horgan, Jose Paulino, Cassie Bach and Jo) who continuously supported me during my study at Flinders University.

1. INTRODUCTION

1.1. Background and objectives

In many countries, coastal aquifers have served as major sources of freshwater for domestic, agricultural, and industrial uses (Lu et al., 2009; Custodio, 2010; Webb and Howard, 2011; Morgan et al., 2012; Werner et al., 2012). Currently, coastal aquifers worldwide are threatened by seawater intrusion (SWI) phenomenon, where seawater moves into coastal aquifers and pollutes fresh groundwater.

The occurrence of SWI is usually associated with human-induced effects, such as groundwater over-exploitation (Bear et al., 1979; Ferguson and Gleeson, 2012), although natural factors such as sea-level rise (SLR) and drought may also contribute to SWI problems (Sherif and Singh, 1999; Werner and Simmons, 2009; Chang et al., 2011). Other transient factors such as seasonality in recharge (Michael et al., 2005; Koussis et al., 2012), and land use change (Koch and Zang, 1998) may also affect SWI.

Previous studies identified two different modes of SWI, i.e., passive and active (Bear and Dagan, 1964; Mahesha, 1995; Werner et al., 2012). In passive SWI, seawater moves inland in areas where fresh groundwater flows towards the sea, and the seawater wedge intrudes rather slowly. Active SWI occurs when the freshwater-saltwater interface moves inland and it is accompanied by freshwater flow in the inland direction. Active SWI is driven by the combined effects of seawater buoyancy, and the inland-sloping hydraulic gradient, whereas in passive SWI, these forces are opposed (Mahesha, 1995; Werner et al., 2012). Active SWI is expected to be more aggressive than passive SWI.

A potential destructive impact of SWI is groundwater salinization at the watertable in an unconfined coastal aquifer (e.g., Werner and Lockington, 2006). Watertable salinization (WTS) phenomenon is important since this may produce soil salinization through capillary rise (Prathapar et al., 1992; Werner and Lockington, 2006). Werner and Lockington (2006) investigated the likelihood of SWI in increasing the groundwater salinity at the watertable in an estuary-aquifer system. They showed that

estuarine tidal fluctuations combined with aquifer pumping may force the salts to move into the upper aquifer and shift landward accompanying a reduction of watertable elevation. In this thesis, we presume that under certain conditions (i.e., active SWI), WTS may occur even in a non-tidal unconfined coastal aquifer setting.

The processes associated with active SWI have received considerably less attention compared to situations of passive SWI despite several investigations demonstrating that active SWI is occurring in many areas (Fetter, 2001; Morgan et al., 2013b; Werner and Gallagher, 2006; Yakirevich et al., 1998). For example, Fetter (2001) reported that active SWI during the 1930s polluted the coastal aquifer underlying Brooklyn (New York, USA), where the watertable declined 9 to 15 m below sea level due to heavy industrial pumping. Yakirevich et al. (1998) simulated SWI in the Gaza Strip (Palestine) coastal aquifer using SUTRA code (Voss and Souza, 1987). They showed that active SWI arose from excessive pumping, which resulted in groundwater levels that were 2.3 m and 6.6 m below sea level in 1996 and 2006, respectively. They found that the rate of SWI during 1997-2006 was around 20-45 m/y. Werner and Gallagher (2006) also reported active SWI in the Pioneer Valley, produced by excessive aquifer depletion and resulting in increased electrical conductivity (EC) at the fringe of the aquifer's seawater extent in 2004. They argued that the mobility of SWI in the Pioneer Valley indicated that an equilibrium condition has not been reached, and that the interface was unlikely to stabilise at a sustainable location. Recently, Morgan et al., (2013b) reported that the aquifers in the Willunga basin (South Australia) are incurring active SWI driven by groundwater heads that are 2 m lower than the coastal head. A simplified two-dimensional real scale transient SWI simulation of Willunga basin using SEAWAT code (Guo and Langevin, 2003) was conducted to demonstrate that under current conditions active seawater intrusion is likely to continue for at least 450 years.

There are limited theoretical investigations of the processes accompanying transient active SWI available (i.e., Bear and Dagan, 1964 and Mahesha, 1995). Bear and Dagan (1964) compared Hele-Shaw experimental results with the prediction obtained from a moving sharp-interface analytical solution due to SWI, triggered by a sudden change in the rate of freshwater seaward flow in a confined coastal aquifer. Mahesha (1995) examined the transient interface problem under passive and active SWI conditions. A

sharp-interface finite element model was used to perform a systematic numerical characterization of advancing interfaces in response to gradual freshwater head decline (FHD) in a phreatic coastal aquifer. Even though Bear and Dagan (1964) and Mahesha (1995) considered active SWI, but their study only provided a preliminary analysis of the critical characteristic of transient SWI behaviour, and the flow processes and the related effects (e.g., WTS, advection and density) associate with active SWI situations were not examined.

This thesis comprises a comprehensive assessment of transient SWI where characteristics of passive and active SWI, and any new phenomenon related to these types of SWI are explored using physical and numerical models. Investigating the occurrence of active SWI in the real world is beyond the scope of this body of research. Chapters 2, 3, 4 and 5 are formatted as journal papers with a concise literature review of active and/or passive SWI in each introduction.

In Chapter 2, physical and numerical models (SEAWAT) are used to examine the occurrence of WTS associated with SWI response to an inland FHD in the absence of tidal effects in unconfined coastal aquifers. Chapter 3 comprises an investigation of SWI in layered coastal aquifers with upward freshwater leakage using a sharp and dispersive interface numerical model. Steady-state and transient predictions from the models are evaluated, and compared to the results of sand-tank experiments. Three alternative sharp-interface modelling strategies are assessed for treating upward freshwater leakage. Case 1 involves freshwater bypassing any overlying saltwater, Case 2 assumes no upward freshwater leakage where there is overlying saltwater and Case 3 converts upward freshwater leakage into saltwater. Chapter 4 presents a systematic investigation of active SWI characteristics at larger scales, using numerical simulations. Relationships between key features of active SWI (e.g., interface characteristics and SWI response time-scales) and the parameters of the problem (e.g., inland FHD, freshwater-seawater density contrast, dispersivity, hydraulic conductivity, porosity, aquifer thickness) are explored. Finally, Chapter 5 extends the previous work with 3D numerical simulations of a real world SWI case. A regional 3D SWI model of Uley South Basin (USB) is developed that adopts spatial heterogeneity in parameters obtained from a prior calibration effort using a single-density model. The investigation

aims to examine individual impacts of climate variability and anthropogenic stresses on the extent of seawater in USB and to investigate the seawater effects on the groundwater head behaviour near the coast. There is a possibility that SWI may influence the groundwater head response around the coast and making it different to the groundwater behaviour further inland within the basin.

Chapter 2 and 3 are papers published in Water Resources Research and Journal of Hydrology, respectively, while Chapters 4 and 5 were recently submitted to the Journal of Hydrology. The papers are as follows:

Badaruddin, S., A. D. Werner and L. K. Morgan (2015). Watertable salinization due to seawater intrusion. Water Resources Research 51: 8397-8408.

Mehdizadeh, S. S., A. D. Werner, F. Vafaie, and S. Badaruddin (2014). Vertical leakage in sharp-interface seawater intrusion models of layered coastal aquifers. Journal of Hydrology 519: 1097-1107.

Badaruddin, S., A. D. Werner and L. K. Morgan (under review). On the characteristic of active seawater intrusions. Submitted to Journal of Hydrology.

Badaruddin, S., A. D. Werner and M. K. Knowling (under review). Contribution of seawater intrusion to aquifer depletion: Uley South Basin (South Australia). Submitted to Journal of Hydrology.

1.2. Outline of remaining chapters

The following abstracts are directly extracted from the aforementioned journal papers, and provide an outline of the content in each of the four main chapters.

Chapter 2: Watertable salinization due to seawater intrusion

SWI is a significant threat to freshwater resources in coastal aquifers around the world. Previous studies have focused on SWI impacts involving salinization of the lower

domain of coastal aquifers. However, under certain conditions, SWI may cause salinization of the entire saturated zone of the aquifer, leading to WTS in unconfined aquifers by replacing freshwater within the upper region of the saturated zone with seawater, thereby posing a salinity threat to the overlying soil zone. There is presently limited guidance on the extent to which WTS may occur as a secondary impact of SWI. In this study, physical experiments and numerical modelling were used to explore WTS associated with SWI in various non-tidal, unconfined coastal aquifer settings. Laboratory experiments and corresponding numerical simulations show that significant WTS can occur under active SWI (i.e., the freshwater hydraulic gradient slopes towards the land) because the cessation of freshwater discharge to the sea and the subsequent landward flow across the entire sea boundary eventually lead to watertable salinities approaching seawater concentration. WTS during active SWI is larger under conditions of high hydraulic conductivity, rapid SWI, high dispersivity and for deeper aquifers. Numerical modelling of four published field cases demonstrates that rates of WTS of up to 60 m/y are plausible. Under passive SWI (i.e., the hydraulic gradient slopes towards the sea), minor WTS may arise as a result of dispersive processes under certain conditions (i.e., high dispersivity and hydraulic conductivity, and low freshwater discharge). Our results show that WTS is probably widespread in coastal aquifers experiencing considerable groundwater decline sustained over several years, although further evidence is needed to identify WTS under field settings.

Chapter 3: Vertical leakage in sharp-interface seawater intrusion models of layered coastal aquifers

Previous sharp-interface studies of SWI adopt various approaches to the treatment of vertical fluxes in regions where alternating saltwater and freshwater are found in overlying aquifers. In this study, we compare dispersive modelling and sand-tank experiments to the results of sharp-interface models to evaluate assumptions regarding vertical fluxes in coastal multi-aquifer systems. The sand-tank experiments (one transient and two steady-states cases) consist of two coarse sand layers separated by a lower-permeability layer of fine sand. Vertical freshwater leakage in sharp-interface models is treated in one of three ways. Case 1: upward freshwater leakage flows only into freshwater in the aquifer above, bypassing any overlying saltwater; Case 2: no

upward freshwater leakage occurs if there is overlying saltwater; Case 3: freshwater leaks into any overlying saltwater without modifying the saltwater salinity. Sharp-interface models over-predicted the toe position of the saltwater wedge in both the experiments and numerical models (regardless of the vertical leakage assumption), in agreement with previous studies. Nonetheless, Case 1 produced improved prediction of the sand-tank results relative to Cases 2 and 3. Freshwater leakage fluxes in areas where the interface was absent were reasonably well represented by all three sharp-interface leakage assumptions, compared to those of the dispersive model. In regions where saltwater overlies freshwater, the upward freshwater fluxes predicted by dispersive modelling were found to be consistently closest to the upward freshwater flux of Case 1, compared to Cases 2 and 3. Saltwater-to-saltwater leakages from the dispersive models were poorly represented by the sharp-interface models. Vertical flux assumptions were then evaluated for idealized field-scale situations, and Case 1 again best matched the dispersive modelling results. Streamlines from dispersive modelling show that upward freshwater leakage tends to flow around and bypass overlying saltwater. This matches optimally the assumption of Case 1. We conclude that Case 1 is the ideal approach to the treatment of upward freshwater fluxes in sharp-interface models of multiple-aquifer systems, whereas Cases 2 and 3 may create unrealistic SWI predictions, especially for situations where overlying aquifers are separated by a layer of low conductance.

Chapter 4: On the characteristics of active seawater intrusion

The inland migration of seawater in coastal aquifers, known as SWI, can be categorised as passive or active, depending on whether the hydraulic gradient slopes downwards towards the sea or the land, respectively. Despite active SWI occurring in many locations, it has received considerably less attention than passive SWI. In this study, active SWI caused by an inland FHD is characterised using numerical modelling of various idealised unconfined coastal aquifer settings. Relationships between key features of active SWI (e.g., interface characteristics and SWI response time-scales) and the parameters of the problem (e.g., inland FHD, freshwater-seawater density contrast, dispersivity, hydraulic conductivity, porosity and aquifer thickness) are explored for the first time. Sensitivity analyses show that the SWI response time-scales under active

SWI situations are influenced by both the initial and final boundary head differences. The interface is found to be steeper under stronger advection (i.e., caused by the inland FHD), higher dispersivity and hydraulic conductivity, and lower aquifer thickness, seawater density and porosity. The interface movement is faster and the mixing zone is wider with larger hydraulic conductivity, seawater-freshwater density difference, and aquifer thickness, and with lower porosity. Dimensionless parameters (Peclet number and mixed convection ratio) from previous steady-state analyses offer only limited application to the controlling factors of passive SWI, and are not applicable to active SWI. The current study of active SWI highlights important functional relationships that improve the general understanding of SWI, which has otherwise been founded primarily on steady-state and passive SWI.

Chapter 5: Contribution of seawater intrusion to aquifer depletion: Uley South Basin (South Australia)

Understanding the relationship between climate variability, anthropogenic stresses and the extent of seawater intrusion (SWI) is critical for developing effective groundwater management strategies. Previous studies of regional SWI have mainly focused on exploring the effects of aquifer stresses in general and do not isolate or compare individual causal factors of SWI. This study isolates the individual contributions of human stresses (groundwater pumping) and climate variability (recharge) to the extent of SWI within a basin setting: the Uley South Basin (USB; South Australia). A regional three-dimension SWI model of USB is developed that adopts the spatial heterogeneity in parameters obtained from a prior calibration effort using a single-density model. Previous studies of USB have shown that, relative to recharge variability, groundwater pumping has a higher contribution to groundwater decline in this area. Nonetheless, whether the same contribution of these two factors to the extent of SWI has occurred is unclear and remains the subject of ongoing debate. In this context, the link between seawater movement and groundwater head behaviour near the coast is critical, and is also examined. No SWI studies to date have explored these effects, even though the density-dependent processes accompanying SWI may alter the groundwater head response. The modelling results show the effects of climate and pumping on the extent of SWI are highly varied in time and space. In 2012 (the end of the simulation period),

the effects of pumping on the extent of SWI (in terms of 0.05 relative salt concentration) is 5.8 and 4.1 times more extensive in USB's Quaternary and Tertiary aquifers, respectively, relative to SWI arising from climate variability. The modelling results also show that slightly increased pumping effects (0.2 to 1.4 cm of additional drawdown) were obtained when seawater and the accompanying density effects were included in the model. This study demonstrates that field-scale coastal aquifer modelling investigations may under-represent the impacts of pumping on freshwater losses if single-density models are employed, and quantifies the importance of seawater in evaluating depletion in a case study setting.

2. WATERTABLE SALINIZATION DUE TO SEAWATER INTRUSION

2.1. Introduction

Currently, coastal aquifers worldwide are under increasing threat of seawater intrusion (SWI) (Ferguson and Gleeson, 2012; Werner et al., 2013). SWI is a phenomenon where seawater encroaches into a coastal aquifer and contaminates fresh groundwater (Bear, 1979). The occurrence of SWI is most commonly associated with the penetration of seawater within the lower domain of a coastal aquifer, due to the higher density of seawater relative to the ambient groundwater. However, Werner and Lockington (2006) identified the potential for SWI to induce watertable salinization (WTS) within unconfined aquifer settings. This occurs when SWI causes salinization of the entire saturated profile of the aquifer, leading to saline water occurring at the watertable of unconfined coastal aquifers. Werner and Lockington (2006) focussed on the effects of tides and rapid decline in the watertable elevation as important factors leading to WTS, although their investigation of WTS was limited to a single situation involving estuarine SWI. The occurrence of WTS may have significant implications for unsaturated zone water quality and productivity, since WTS may lead to soil salinization (Prathapar et al., 1992; Werner and Lockington, 2004; Werner and Lockington, 2006; Ibrahimi et al., 2014). WTS due to SWI has not been documented in real-world settings or under controlled laboratory situations, and hence the occurrence, extent and causes of WTS remain unclear.

In this study, physical experiments and numerical modelling are combined to examine the occurrence of WTS associated with SWI in response to an inland freshwater head drop. Comparing the laboratory and numerical modelling results offers insight into both the veracity of the laboratory set up and the assumptions of the numerical code. WTS is examined in the absence of tidal effects, and the analysis focuses on the influence of watertable decline on WTS. We anticipate that more aggressive SWI will lead to WTS, in accordance with Werner and Lockington's (2006) prediction of WTS during rapid watertable decline. The effects of freshwater head declines (rather than sea-level rise) on WTS are considered in this study, because these are expected to develop faster and

be larger in magnitude than sea-level rise, and are therefore more likely to generate more aggressive SWI situations (IPCC, 2008; Werner et al., 2013).

2.2. WTS conceptual models: active and passive SWI

Previous studies identify two different modes of SWI: passive and active (Bear and Dagan, 1964; Mahesha, 1995; Werner et al., 2012). In the former, SWI occurs despite persistent freshwater discharge to the sea, and the seawater wedge intrudes rather slowly. Where passive SWI arises from a reduction in the watertable elevation, there will be an accompanying decrease in the depth of freshwater discharging at the shoreline (Werner et al., 2012; Morgan et al., 2012), referred to here as the freshwater outflow face (O_f [L]) as shown in Figure 2.1a. Where the discharge face is not vertical, there will nonetheless be a depth of freshwater discharge at the shoreline that separates seawater from the watertable (in the absence of tidal effects) (Bakker, 2006; Benson et al., 1998). It is hypothesised that, in the case of non-tidal passive SWI, there may be an increase in watertable salinities accompanying a reduction in O_f, largely due to dispersive effects and the closer proximity of the seawater wedge to the watertable. Here, we define WTS as the distance from the shoreline to the "tip" of the seawater wedge (x_{tip} [L]; Figure 2.1b), which is designated by a particular salinity. The seawater wedge "toe" is the extent of seawater along the aquifer basement (x_{toe} [L]; Figure 2.1). Following previous SWI literatures (i.e., Watson et al., 2010; Jakovovic et al., 2011; Mehdizadeh et al., 2014), x_{tip} and x_{toe} are calculated using 5% of seawater salinity. By connecting the toe and the tip of the interface with a straight line, the interface alignment (θ) is defined as shown in Figure 2.1a and 2.1b.

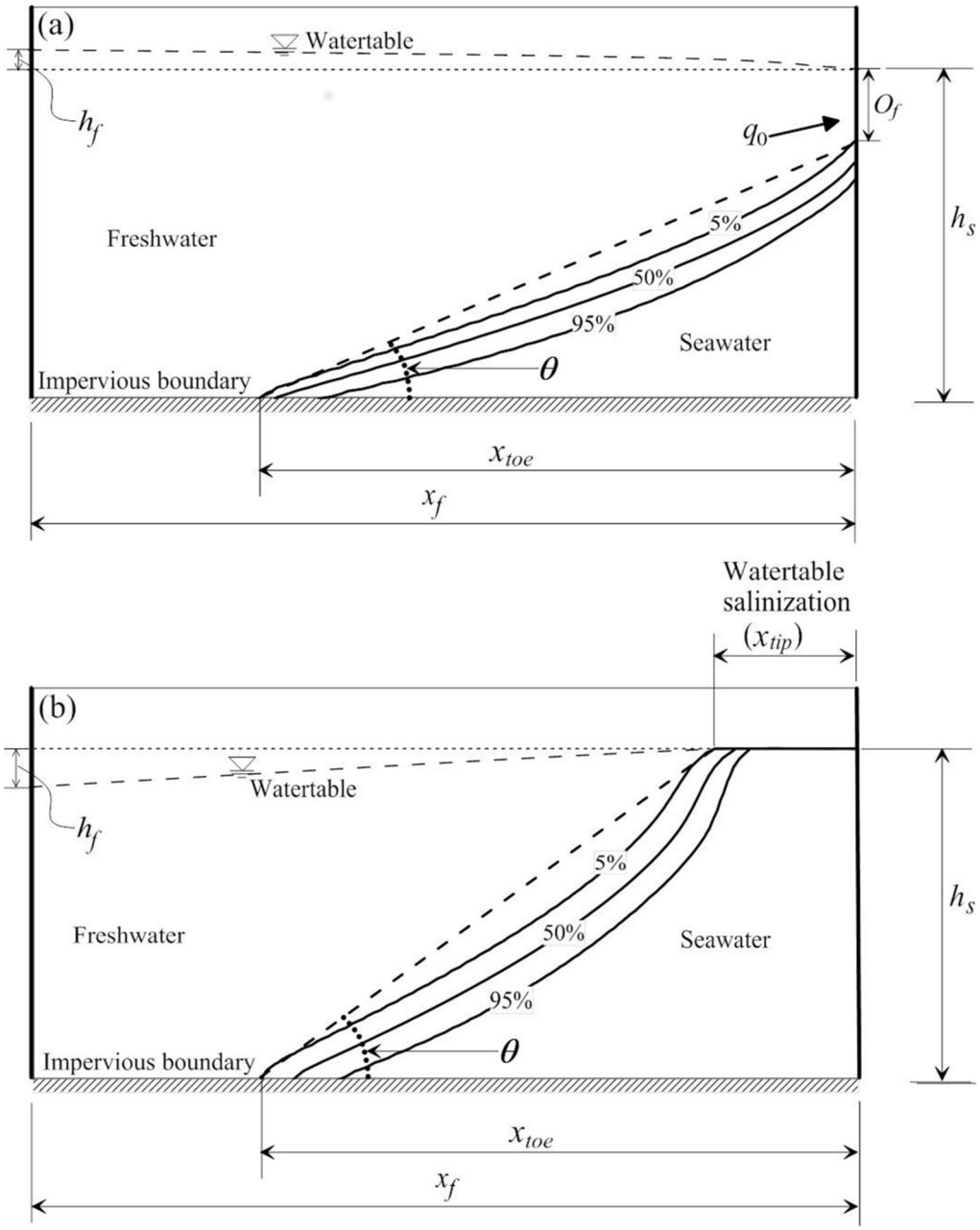

Figure 2.1. Conceptual schematic of: (a) passive SWI and (b) active SWI. h_f is the height of the watertable at the inland boundary measured from sea level, and is negative for active SWI cases, x_f is the distance to the inland boundary condition [L], and h_s is the depth of the horizontal base of the aquifer below sea level [L].

In the limiting condition where freshwater discharge to the sea (q_0 [L^2/T]) ceases, a transition occurs from passive SWI to active SWI at the shoreline. The cessation of q_0 reduces O_f to zero, which causes the freshwater-saltwater interface tip to occur at, rather than below, the watertable. Active SWI is driven by the combined effects of the density difference between freshwater and seawater, and the inland-sloping hydraulic gradient,

whereas in passive SWI, these forces are opposed. We expect significantly more extensive WTS under active SWI. The rate of WTS under both active and passive SWI is likely to be a non-linear function of several parameters given the complex nature of the density-dependent flow and transport relationships accompanying transient SWI (Lu and Werner, 2013).

2.3. Experimental methods and materials

2.3.1. Laboratory experiments

Laboratory experiments were undertaken using the same apparatus as that used by Mehdizadeh et al. (2014). The sand tank has internal dimensions of 117.0 cm (length), 5.2 cm (width), and 60.0 cm (height), and is constructed of 10 mm thick transparent plate glass supported by a stainless steel frame. We acknowledge the small scale of the sand tank, relative to real-world conditions, as a limitation of the laboratory experiments. However there is a lack of field-based investigations of WTS, and hence, these are the only physical modelling observations of this phenomenon that are presently available. The tank was filled with sand to a height of 52.0 cm. Twelve plastic inflow and outflow ports are installed at 5.0 cm intervals along the sides of the tank. A schematic of the experimental set up is shown in Figure 2.2.

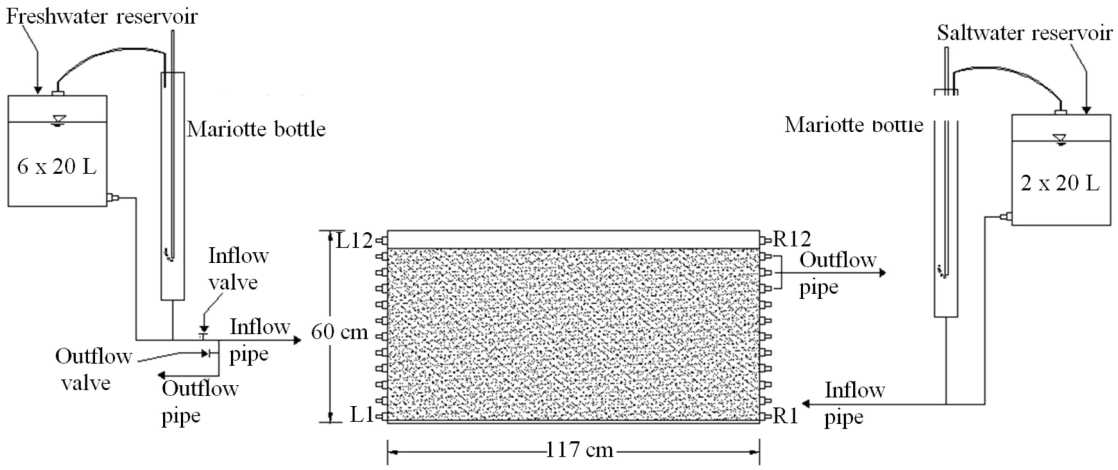

Figure 2.2. Schematic of the sand-tank set up. The inland and seaside boundaries are the left and right sides of the tank, respectively.

Head boundaries of the tank (inland and seaside) were controlled using Mariotte bottles connected to the inflow-outflow taps. The water and gas components of the Mariotte bottles were inter-connected, following Klute and Dirksen (1986). In steady-state experiments, saltwater entered the tank through taps R2 to R7, freshwater entered through taps L2 to L11, and taps R9 to R11 provided mixed-water discharge (Figure 2.2). A specified-head condition was applied to the entire right boundary of the sand tank (sea boundary) to represent seawater hydrostatic heads.

The tank arrangement allowed for either inflow or outflow of freshwater through the inland boundary, depending on whether passive or active SWI conditions were being explored. Taps R9 to R11 in Figure 2.2 were closed when the head at the inland boundary dropped lower than the sea boundary in order to prevent mixed water being drawn into the sand tank under active SWI conditions. Three manometers were attached to taps L1, R1 and R8 to monitor the head at both the inland and sea boundaries (see Figure 2.2).

A saltwater solution was produced using 1400 g of calcium chloride dehydrate ($CaCl_2.2H_2O$) dissolved in 40 L of tap water (freshwater). Following Werner et al. (2009), Rhodamine WT (fluorescent FWT Red dye, ENVCO, Australia) with concentration of 500 mg/L was used as a visual tracer of saltwater movement in the tank. Rhodamine WT has been widely and successfully used in sand-tank models previously (e.g., Schincariol and Schwartz, 1990; Werner et al., 2009; Jakovovic et al., 2011; Shi et al., 2011; Jakovovic et al., 2012). Saltwater density (ρ_s [M/L^3]) and freshwater density (ρ_f [M/L^3]) were 1018.3 kg/m^3 and 998.1 kg/m^3, respectively (determined using a pycnometer and mass-volume measurements), and a saltwater concentration (C_s [M/L^3]) of 26.4 kg/m^3 was calculated. The saltwater concentration value of 26.4 kg/m^3 indicates the total mass of salt per unit volume of water. The density of saltwater used in the physical experiment (1018.3 kg/m^3) is relatively low compared to typical seawater density (1025 kg/m^3). This increased the amount of time and space available within sand-tank experiments to observe the interface movement under active SWI conditions, before the interface toe reached the inland boundary. SEAWAT modelling indicated that using a lower saltwater density of 1018.3 kg/m^3 instead of 1025 kg/m^3 increased the physical modelling duration from 10 min to 20 min

(the results are not shown for brevity). In addition, a lower saltwater density (i.e., 1015.1 kg/m^3) has been successfully used previously by Morgan et al. (2013c) to explore SWI transient effects in physical experiments. The experiments were recorded using an 8 mega-pixel digital camera and pictures were taken at 15 min intervals for passive SWI experiments and at 0.5 min intervals for active SWI experiments.

Medium-grained sand (i.e., '16-30' grade sands, Sloan Sands P/L, Dry Creek, South Australia) was the porous medium used in the experiments. A wet-packing method was adopted to obtain a relatively uniform level of compaction and minimal entrapped air (Ojuri and Ola, 2010). Porosity (n [-]) of the sand was measured by the water saturation method (Fetter, 2001) and found to be 0.41. The sand hydraulic conductivity (K [L/T]) was estimated by two different methods: (1) constant head (Darcy column test), and (2) sieve/grain-size analysis combined with the Kozeny-Carman formula (Freeze and Cherry, 1979). Darcy column tests used a 37 cm long, 5 cm internal diameter acrylic cylinder, and were conducted three times. The sand was packed under saturated conditions in a similar fashion to the sand-tank experimental set up. The average K obtained from Darcy column tests was 269 m/d. The grain-size distribution curve from the sieve analysis gave values for d_{10}, d_{50}, and d_{60} of 0.57, 0.64 and 0.78 mm, respectively, and 1.37 for the uniformity coefficient (d_{60}/d_{10}). Applying these values to the Kozeny-Carman formula provided a K of 308 m/d. Since the same wet packing method was adopted in filling both the sand tank and the Darcy column, the value of 269 m/d was used for horizontal and vertical K in the numerical model of laboratory experiments. The saturation and drainage method described by Johnson (1967) was used to obtain a specific yield (S_y [-]) of 0.32 for the sand.

Prior to commencing the transient experiment, h_f and h_s were maintained at 2.2 cm and 48.2 cm, respectively (refer to Figure 2.1), for several hours in order to establish steady-state conditions. Steady-state conditions were confirmed by monitoring both the toe position and the discharge flux for 4 hours, after which time no changes were observed. Passive SWI in response to a freshwater head decline (FHD) was induced by lowering h_f from 2.2 to 1.2 cm instantaneously (refer to Figure 2.1). After 210 min of passive SWI, the interface toe reached about half of the aquifer length (i.e., 62.0 cm). Numerical modelling indicated that the interface was still moving at this time. Steady-

state conditions would require an additional 840 min to reach a stable x_{toe} of 73.3 cm from the sea boundary (the results are not shown for brevity). After 210 min, h_f was instantaneously dropped from 1.2 to -4.8 cm (refer to Figure 2.1) to induce active SWI. The experiment continued until the wedge almost reached the inland boundary (i.e., after 18 min of active SWI). The position of the toe and the tip of the interface were estimated from visual inspection of the experimental photography, which captured the distribution of the visual tracer. In-situ salinity measurements were not possible using the current sand tank, and therefore salt distributions were explored only through a comparison of numerical modelling and visual inspection of physical experiments.

2.3.2. Numerical model

The variable-density groundwater flow and transport code SEAWAT version 4 (Langevin et al., 2008) was used to simulate transient SWI in laboratory experiments and at the field scale. SEAWAT has been validated using several benchmark problems (e.g., Langevin et al., 2003; Brovelli et al., 2007; Goswami and Clement, 2007), and is widely used, and thus the governing equations from the user manual (Guo and Langevin, 2002) are not re-written here for brevity.

The model domain used in the numerical model was in accordance with the dimensions of the sand tank as shown in Figure 2.2. Dirichlet conditions for head were used to represent the sand tank side boundaries, and no-flow conditions were assigned to the bottom of the model. In SEAWAT simulations, a specified-head condition was assigned to the vertical coastal boundary to represent the density-dependent head distribution of the ocean (Langevin, et al., 2008). The concentration boundary condition at the coastal boundary is one where inflowing water has the concentration of seawater, whereas outflowing water is assigned the ambient concentration of groundwater at the boundary. In this way, inflow causes the coastal boundary cells to approach seawater concentration, and discharge through the boundary generally causes a reduction in the boundary salinity. At the coastal boundary, the equivalent freshwater head remains unchanged throughout the simulation, despite that the solute concentration at the boundary varies depending on the direction of flow. The CHD package of SEAWAT was used to represent the instantaneous inland FHD. Numerical modelling adopted a

molecular diffusivity D_m [L^2/T] of 10^{-9} m^2/s, and longitudinal dispersivity α_L [L] was 0.4 cm, as derived from the Ogatta-Banks (1961) analytical solution and breakthrough fitting curves obtained during the Darcy column tests. Following Abarca et al. (2004), transverse dispersivity α_T [L] was assumed to be one tenth of α_L. Discretization of the model domain was initially estimated using the grid Peclet number (*Pe* [-]) criterion (Voss and Souza, 1987):

$$Pe = \frac{q_f \Delta L}{D_m + \alpha_L q_f} \approx \frac{\Delta L}{\alpha_L} \leq 4 \tag{2.1}$$

Where q_f [L/T] is the local groundwater velocity and ΔL [L] is the grid spacing. The total height of the porous medium used in the numerical model was 52 cm. A uniform grid size of Δx = 0.50 cm and Δz = 0.50 cm resulted in a grid of 24,336 cells and a *Pe* of 1.25. This discretization scheme was then further validated by comparing the simulation results of a finer grid size with Δx = 0.25 cm and Δz = 0.50 cm, and the difference in the interface position was less than 0.05 cm. A time step of 30 s was employed, and the transport step size was set to 3 s. Three stress periods were defined in the numerical model of laboratory experiments, as: (1) a 4-hour period to reach steady-state conditions with h_s at 48.2 cm and h_f at 2.2 cm (refer to Figure 2.1), (2) h_f was dropped by 1.0 cm instantaneously, and passive SWI was simulated for 210 min, and (3) h_f was dropped instantaneously by 6.0 cm to produce active SWI for 18 min.

SWI simulations of several simplified field settings, using parameters from published case studies, were undertaken to gain insight into WTS under more realistic conditions relative to laboratory-scale experiments. Following Jakovovic et al. (2011) and Morgan et al. (2013c), no calibration of the laboratory and field-scale models was undertaken in this study. The SWI case studies and their related parameters are summarized in Table 1. Only brief descriptions are provided for the SWI field cases. The reader is directed to publications by Werner and Gallagher (2006), Kouzana et al., (2009), Ayni et al., (2011), Cook et al., (2013), Morgan et al., (2013a), and Morgan et al., (2013b) for a complete account of the respective field settings. Case 1 parameters apply to the Pioneer Valley unconfined aquifer, Australia (Werner and Gallagher, 2006; Morgan et al., 2013a), Case 2 parameters represent the Quaternary unconfined aquifer in Willunga Basin, Australia [Morgan et al., 2013b], Case 3 parameters are based on the Korba

aquifer, Tunisia (Kouzana et al., 2009; Ayni et al., 2011), and Case 4 represents the Cape Range Group aquifer, Australia (Cook et al., 2013). In Table 1, the initial and post-SWI values of h_f were taken from well observations located at a distance (x_f [L]) from the coast in each of the study areas. The initial h_f values for Cases 1, 2, 3 and 4 were measured in years 1988, 1988, 1993 and 1955, respectively, and h_f values following watertable decline were measured in years 2005, 2014, 2006 and 1994, respectively. W_{net} [L/T] and δ [-] in Table 1 are distributed net recharge and dimensionless density ratio $\delta = \left(\rho_s - \rho_f\right)/\rho_f$, respectively.

Table 2.1. Parameter values for SWI case studies.

Parameter	Case study			
	1	2	3	4
FHD rate (m/y)	0.32	0.02	0.48	0.12
FHD period (y)	17	26	13	39
K (m/d)	166	10	7	45
h_s (m)	37	20	50	120
Initial h_f (m)	4.64	1.12	1.30	3.40
Post-SWI h_f (m)	-0.80	0.60	-5.00	-1.43
x_f (m)	4750	1250	2000	2700
n (-)	0.10	0.30	0.27	0.30
S_y (-)	0.05	0.20	0.20	0.25
α_L (m)	10	1	10	10
α_T (m)	1	0.1	1	1
D_m (m^2/d)	0	0	0	0
δ (-)	0.025	0.025	0.025	0.025
W_{net} (mm/y)	110	20	33	15

2.4. Results and discussion

2.4.1. Comparison between laboratory experiments and numerical modelling

In this study, the sand-tank experiments focus on validating SEAWAT's use in simulating WTS. We tested SEAWAT's ability to predict WTS because the code

considers saturated conditions only, whereas the sand-tank and field settings include both saturated and unsaturated conditions, and our study focuses on the saturated-unsaturated interface. Furthermore, SEAWAT has not been used to investigate WTS previously. The results of the laboratory experiments are presented in Figure 2.3. The initial steady-state interface is shown in Figure 2.3a, which indicates a reasonable match between the physical experiment and numerical model. There was also a reasonable match between the physical experiment and numerical model following passive and active SWI conditions as shown in Figure 2.3b (210 min of passive SWI) and Figure 2.3c (after 13 min of active SWI), respectively. Sand tank and numerical modelling values of x_{toe}, x_{tip} and θ for the conditions shown in Figure 2.3 are listed in Table 2.

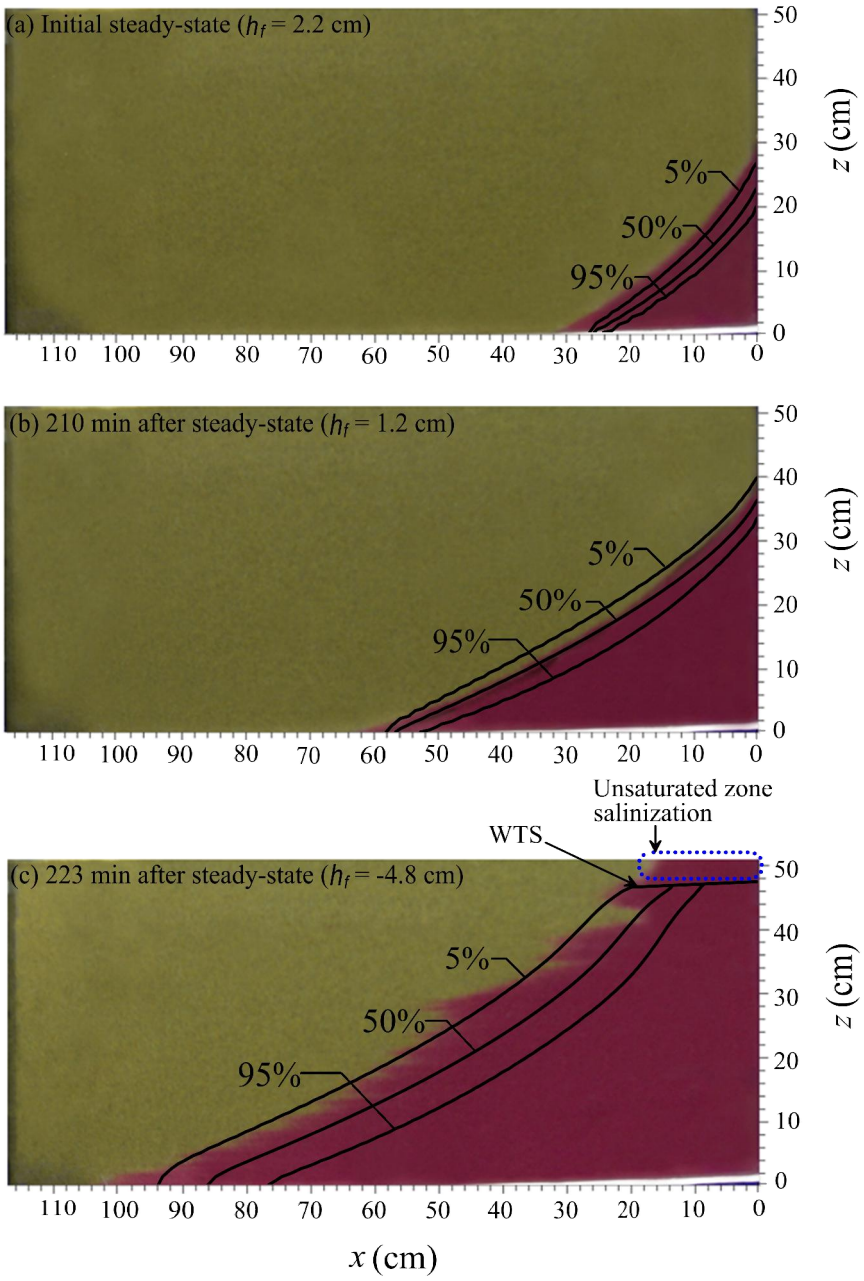

Figure 2.3. Comparison of observed saltwater wedge profiles between physical experiments and numerical modelling for: (a) initial steady-state conditions, (b) following 210 min of passive SWI, and (c) after 13 min of active SWI (black lines represent the numerical modelling results).

Table 2.2. The values of x_{toe}, x_{tip} and θ obtained from physical experiments and numerical modelling for the conditions shown in Figure 2.3.

Parameter	Physical experiment			Numerical model		
	Time (min)			Time (min)		
	0 (steady-state)	210	223	0 (steady-state)	210	223
x_{toe} (cm)	31.9	62.0	103.1	26.2	58.4	93.8
x_{tip} (cm)	0.0	0.0	23.0	0.0	0.0	19.5
θ (°)	42.3	32.2	30.7	45.3	34.4	32.6

The sharp interface observed in the laboratory experiment appeared wider in the numerical model under passive SWI conditions, but overall a reasonable match was observed for both steady-state and passive SWI conditions. The interface was highly dispersed and uneven under active SWI in the laboratory experiment (refer to Figure 2.3c). In the numerical model, the interface was wider during active SWI than in the passive case, in agreement with the laboratory results. However, the irregular shape of the laboratory interface, likely caused by small-scale heterogeneities, was smooth in the numerical model. That is, the high flow velocities associated with active SWI accentuate variability in the shape of the freshwater-saltwater interface due to heterogeneity effects. This process is simulated in an averaged manner by the velocity-dependent dispersion of SEAWAT, which reproduces reasonably well the widening of the interface under active SWI conditions.

As shown in Figure 2.3, a more aggressive landward movement of the interface occurred under active SWI compared to passive SWI, as expected. Active SWI was accompanied by WTS within both the physical experiment and numerical model (Figure 2.3c). The salinization of the watertable led to salinization of the overlying unsaturated zone near the coastal boundary of the laboratory experiment (Figure 2.3c). The saturation-only approach of SEAWAT cannot simulate this effect. This provides an initial indication, albeit only at the laboratory scale, that unsaturated zone salinization arising from active SWI is a plausible occurrence. Werner and Lockington (2004) undertook a simple 1D numerical investigation of salt rise from salinity-impacted watertables and found that surface salinization was a plausible outcome of enhanced

watertable salinities due to SWI. However, further investigation of this process is needed to investigate the likely extent of unsaturated zone salinization under field-scale conditions.

Figures 2.4a, 2.4b, and 2.4c show the transient values of x_{toe}, x_{tip}, and θ, respectively, as obtained from the physical experiments and numerical modelling. x_{toe} increased gradually under passive SWI and then rapidly under active SWI (Figure 2.4a). x_{tip} was 0.0 cm during passive SWI and increased abruptly following the commencement of active SWI. θ values decreased with time in both the physical experiments and numerical modelling during passive SWI because the toe of the wedge advanced inland and the tip did not advance landward. The commencement of active SWI via the instantaneous FHD of 6.0 cm (after 210 min) eliminated freshwater discharge q_0 to the sea boundary and the accompanying outflow face (i.e., O_f was 8.2 cm in the numerical model and 9.2 cm in the physical experiment) after 1 min. Once the tip of the saltwater wedge reached the watertable, θ increased abruptly in the physical experiment and the numerical model, from 32.2° to 36.8° and 34.4° to 38.1°, respectively after 1 min of active SWI. This indicates faster inland movement of the interface tip relative to the toe during the initial stages of active SWI in both the physical experiment and the numerical model. θ subsequently decreased during the rest of simulation. At the conclusion of the experiment (after 228 min), θ had reduced to 29.5° in the physical experiment and 31.3° in the numerical model, indicating faster toe movement relative to the tip during the later stages of active SWI.

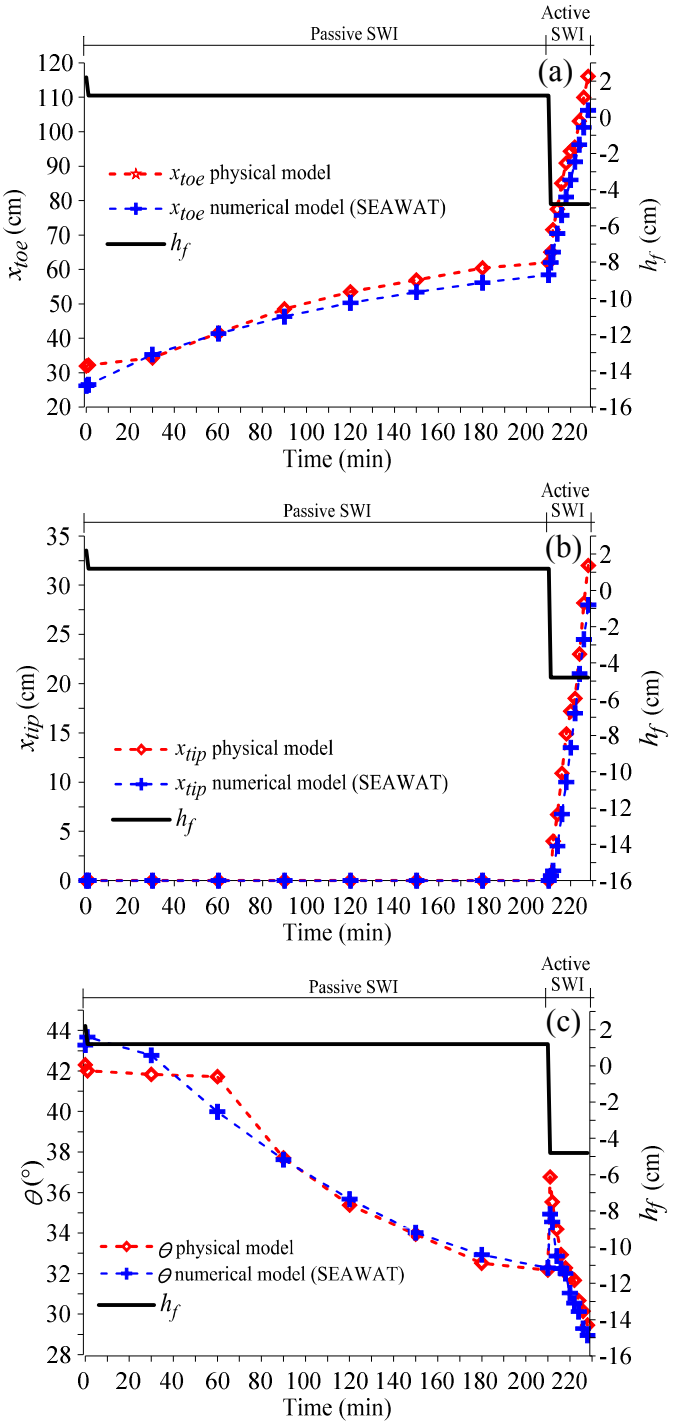

Figure 2.4. The temporal behaviour of the freshwater-seawater interface under passive and active SWI at the laboratory scale, in terms of: (a) wedge toe location, (b) wedge tip location, and (c) the interface alignment.

Particle tracking modelling using PMPATH (Chiang and Kinzelbach, 1994]) was undertaken to explore the origins of WTS. Laboratory-scale results are shown in Figure 2.5 after 210 min of passive SWI (Figure 2.5a) and after 0.5 min of active SWI (Figure

2.5b). It can be seen that the saltwater circulation that was present under passive SWI (Figure 2.5a) ceased under active SWI (Figure 2.5b). WTS is clearly derived from the lateral movement of saltwater from the sea boundary.

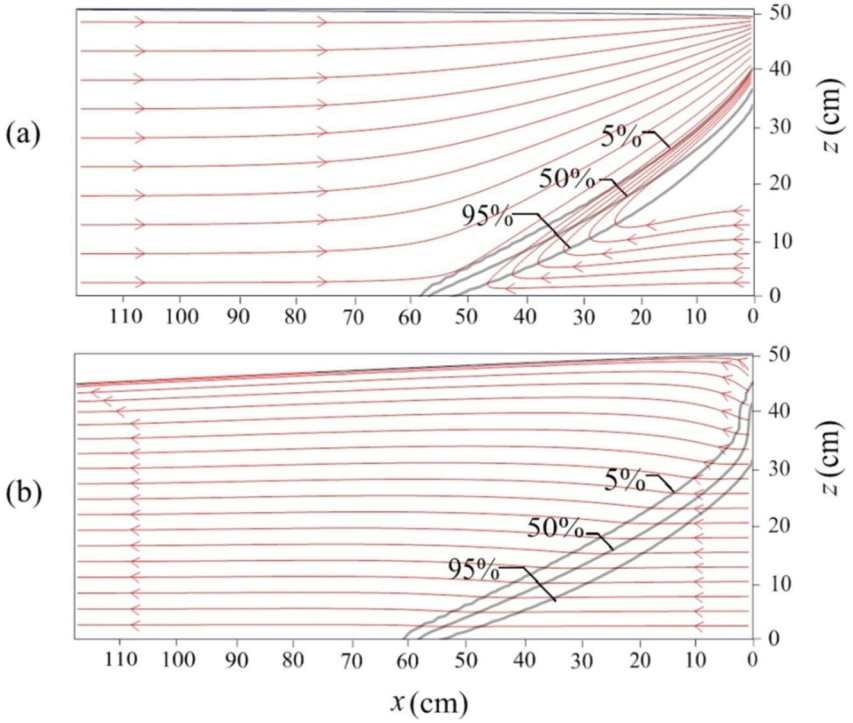

Figure 2.5. The results of particle tracking for: (a) passive SWI after 210 min and (b) active SWI after 0.5 min.

2.4.2. Numerical simulation of SWI case studies

The case studies of modified coastal aquifers include both active and passive SWI situations. The post-SWI h_f values in Table 1 indicate that inland-sloping hydraulic gradients and active SWI have occurred in Cases 1, 3 and 4, whereas Case 2 has experienced a seaward-sloping hydraulic gradient and passive SWI conditions. Figure 2.6 shows the simulated position of the 5%, 50% and 95% seawater salinities for the four case studies, following gradual FHDs at rates and magnitudes listed in Table 1. Significant WTS occurred in Cases 1, 3 and 4. x_{tip} values for Cases 1 and 3 were 597 m and 415 m, respectively. In Case 4, x_{toe} reached the inland boundary (at 2700 m) after 24 y of FHD, which was prior to the completion of the 39 y simulation period. Therefore, an earlier simulation time (i.e., 22 y) is presented in Figure 2.6 for Case 4 to avoid the inland boundary effect on the freshwater-saltwater interface. x_{tip} in Case 4 was

542 m after 22 y. There was minor WTS in Case 2, in which the watertable salinity exceeded 5% of seawater up to 18.4 m from the seaward boundary.

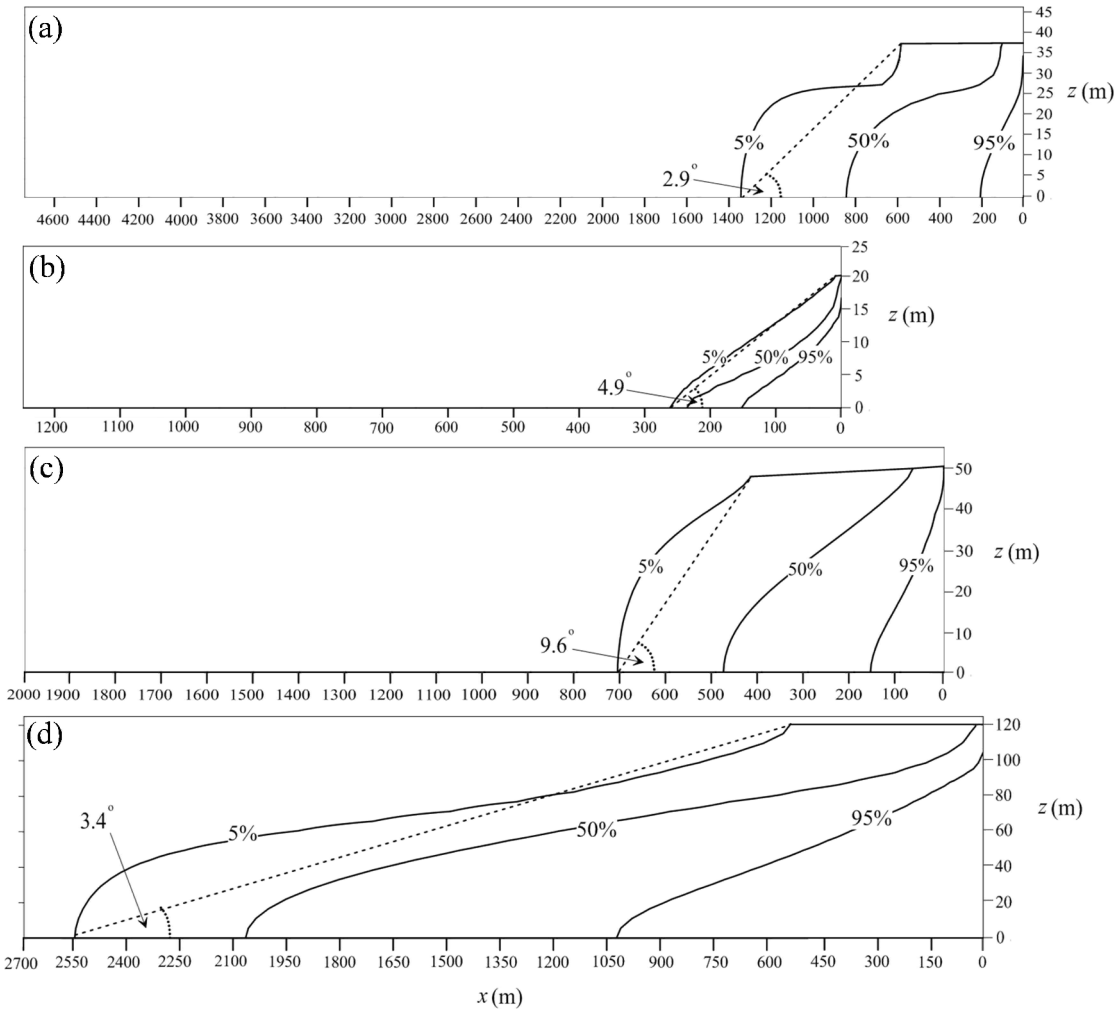

Figure 2.6. The results of SEAWAT numerical simulations after gradual inland FHD scenario for: a) Case1, Pioneer Valley aquifer, b) Case 2, Willunga Basin aquifer, c) Case 3, Korba aquifer, and d) Case 4, Exmouth aquifer (after 22 y).

At the end of the simulation periods, O_f was zero in all cases (i.e., the 5% seawater salinity had reached the watertable), including the passive SWI case where dispersive processes led to brackish groundwater discharge to the sea. This result suggests that WTS could theoretically occur in field-scale coastal aquifers under both passive and active SWI situations. At the cessation of simulations, θ values for Cases 1, 2, 3 and 4 (i.e., after 22 y) were 2.9°, 4.9°, 9.6° and 3.4°, respectively. In general, the values of θ obtained in the field-scale models are much less than the laboratory-scale model (see Figure 2.4c). This is attributable to the larger aspect ratio (i.e., the ratio of aquifer

length to thickness) within the field-scale models (ranging from 22 to 128) relative to the laboratory-scale model (2.4).

Salinities at the watertable (i.e., between the tip and coast) are predominantly less than 50% of seawater in all cases, indicating that WTS is primarily associated with brackish water from the mixing zone. Hence, longitudinal and transverse dispersivity, which control the width of the mixing zone (Abarca et al., 2007) are critical aspects of WTS extent.

Temporal patterns in SWI are given in Figure 2.7, which shows continuous decreases in θ (i.e., the toe moved faster than the tip) with time in Cases 1, 2, and 4. In Case 3, θ decreased for the first 9 y and then increased for the remaining simulation period. This indicates that the movement of the interface tip became faster than the movement of the interface toe after 9 y. This lag in the response of the interface tip may be attributed to the relatively low K used in Case 3 (i.e., K is 7 m/d). That is, longer response times occur in aquifer systems characterised by lower K values (Watson et al., 2010). A lag in the reduction of freshwater flux q_0 at the sea boundary was observed for Case 3, with q_0 reducing slowly from 0.46 m^2/d to 0.06 m^2/d during the first 9 y. This phenomenon was not observed in Case 2 (i.e., K is 10 m/d), which involved passive SWI, where changes in q_0 are more subdued (i.e., q_0 was 0.20 m^2/d at the end of the simulation period).

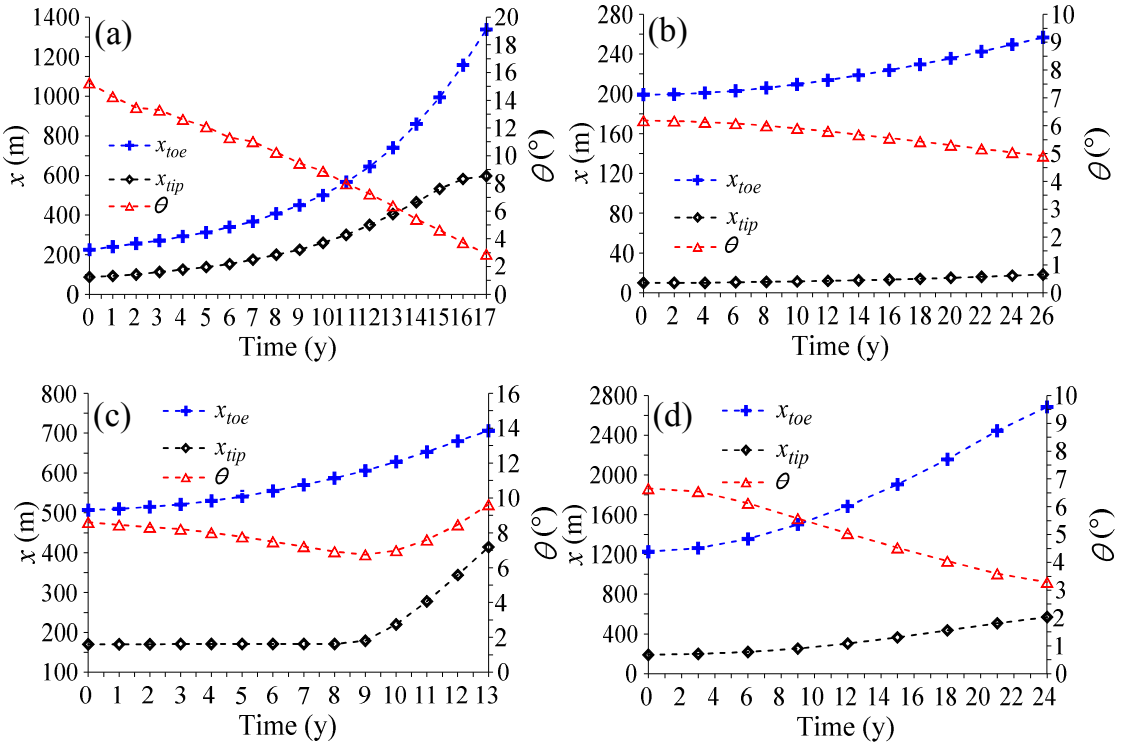

Figure 2.7. The freshwater-saltwater interface profile indicators for: (a) Case 1, Pioneer Valley aquifer, (b) Case 2, Willunga Basin aquifer, (c) Case 3, Korba aquifer, and (d) Case 4, Exmouth aquifer.

In order to explore the role of various parameters in controlling WTS, a sensitivity analysis was conducted using Case 4 as a base case. Different rates of FHD (0.18 m/y, 0.24 m/y, instantaneous), K (22.5 m/d, 67.5 m/d, 90.0 m/d, 112.5 m/d), α_L (1 m, 20 m, 30 m, 40 m), and h_s (115 m, 126 m) were used. The results presented in Figure 2.8 indicate that the magnitude of WTS is largest under conditions of high rates of FHD (Figure 2.8a), high K (Figure 2.8b), high α_L (Figure 2.8c) and large h_s (Figure 2.8d). It is shown in Figure 2.8d that a higher value of aquifer thickness h_s may lead to an increase in SWI and WTS in coastal aquifers, even though the boundary head difference between the inland and coastal boundary remained the same. This is likely due to the change in the model's aspect ratio (the ratio of aquifer length to thickness), whereby decreasing this ratio (due to the increase of h_s) enhances SWI and therefore WTS. This is in agreement with the result of Werner and Simmons (2009) and Lu and Werner (2013) who showed that the extent of SWI is larger in a thicker coastal aquifer, in response to the same boundary head differences. Interestingly, x_{tip} increased and x_{toe} decreased with higher values of α_L (Figure 2.8c). That is, higher dispersivity led to a

smaller magnitude of SWI extent within the lower domain of the coastal aquifer than in the upper domain. This agrees with the results of Kerrou and Renard (2010), who showed that an increase in dispersion (i.e., due to a larger dispersivity parameter or heterogeneity) may cause a decrease in density contrast within the mixing zone and a larger zone of mixing. They concluded that this condition may lead to a rotation of the saltwater wedge, where its base will move seaward relative to the upper part.

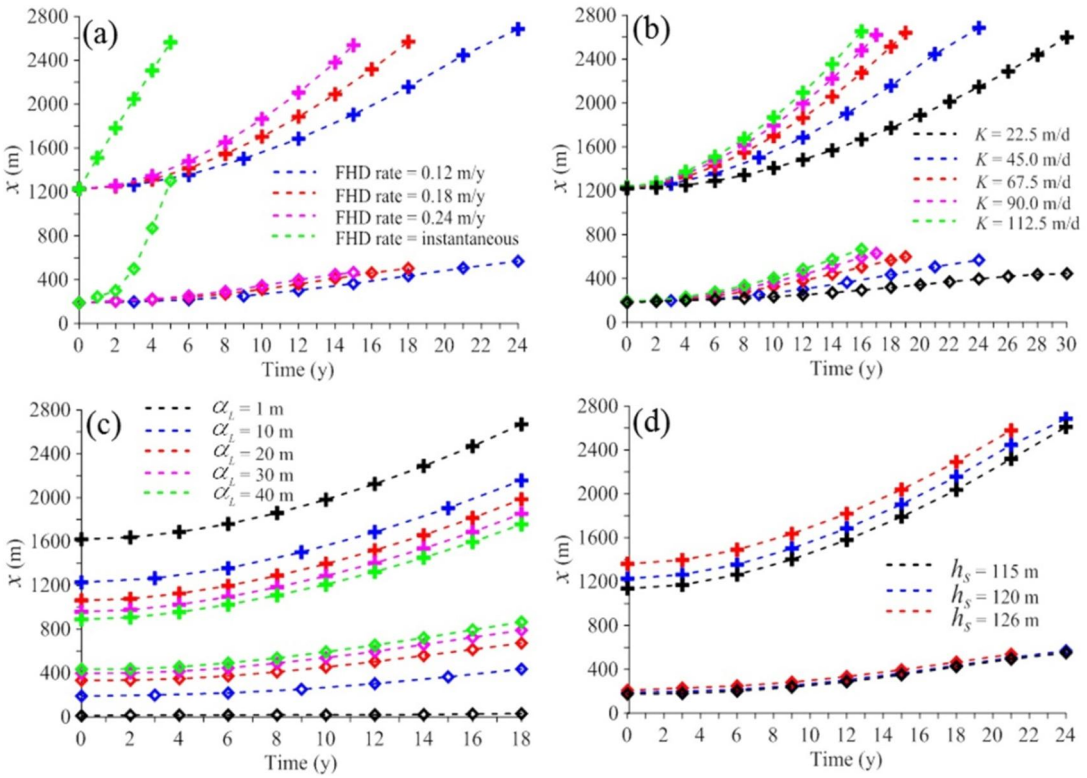

Figure 2.8. Sensitivity analysis for different values of: (a) FHD rate, (b) hydraulic conductivity, (c) dispersivity, and (d) aquifer thickness, using Case 4 Exmouth aquifer as a base case. x_{toe} trends are indicated by crosses (+) and x_{tip} trends by diamonds (◊).

2.5. Conclusions

SWI in unconfined coastal aquifers can result in WTS, which may induce soil salinization through capillary rise. There is presently limited guidance on the extent to which WTS may occur as a secondary impact of SWI. In this study, physical experiments and numerical modelling were used to explore WTS associated with SWI in various non-tidal, unconfined coastal aquifer settings.

Laboratory experiments and corresponding numerical simulations show that significant WTS may occur under active SWI due to the associated cessation of fresh groundwater flow to the coast. Under passive SWI conditions, minor WTS might occur under certain conditions (i.e., high α_L, high K, and low q_0) and as a result of dispersive processes, where the watertable may exceed 5% of seawater salinity in the vicinity of the sea boundary.

Numerical modelling of published field cases shows that WTS may occur at rates of up to 60 m/y, although supportive field evidence is presently lacking. Minor WTS was simulated in the Willunga basin aquifer that is presently undergoing passive SWI, while major WTS was modelled in the other three published field cases (i.e., Pioneer Valley, Korba, and Exmouth aquifer) that have experienced active SWI. WTS during active SWI is larger for cases with higher K, rapid FHD, higher dispersivity parameters and a thicker aquifer. These results suggest that the likelihood of WTS in real-world settings is high under active SWI conditions, and hence further field substantiation and an evaluation of the implications for unsaturated zone salinization is needed, particularly within aquifers where groundwater levels have fallen below sea level.

3. VERTICAL LEAKAGE IN SHARP-INTERFACE SEAWATER INTRUSION MODELS OF LAYERED COASTAL AQUIFERS

A modified version of this work was used by the first author (S. Sadjad Mehdizadeh) as a part of his PhD thesis that submitted in K. N. Toosi University of Technology, Tehran, Iran.

3.1. Introduction

Population growth and the scarcity of coastal freshwater resources have increased the stresses on many coastal aquifers, leading to aquifer storage decline and seawater intrusion (SWI) (Bear et al., 1999; Feseker, 2007; Werner et al., 2013). Most coastal aquifers comprise overlying sequences of geological strata, resulting in SWI characteristics that may differ significantly to those of homogeneous cases (e.g. Collins, 1971; Paniconi et al., 2001). Layered coastal aquifers have received significantly less attention than the more simplified single-layer case, despite that stratified aquifers are widespread (Lu et al., 2013).

The investigation of coastal aquifers routinely involves the application of SWI models, which can be divided into two categories, namely sharp-interface and dispersive-interface approaches. Sharp-interface approaches are computationally more efficient, and allow for the application of analytical solutions, predominantly assuming steady-state conditions and considering both single-layer aquifers (e.g. Mantoglou, 2003; Werner et al., 2012) and layered systems (e.g. Mualem and Bear, 1974; Dagan and Zeitoun, 1998). This approach is more practical for problems requiring reduced computational effort, such as large-scale problems applied to automated calibration procedures, or where the transition zone is thin relative to the depth of aquifer (Bear, 1979). Dispersive-modelling approaches are more numerically challenging, but allow for freshwater-saltwater mixing and the estimation of the dynamics of a wider range of salinities (e.g. Werner and Gallagher, 2006).

In the application of sharp-interface methods to layered aquifers, there is no mixing between freshwater and saltwater, and therefore it is necessary to make simplifying assumptions about vertical fluxes between overlying aquifers, in particular in areas where saltwater overlies freshwater. For example, Essaid (1990) applied a finite-difference sharp-interface approach to simulate SWI in the Soquel-Aptos Basin, USA. She assumed horizontal flow in the aquifer and vertical flow in the aquitard. Where freshwater and saltwater are juxtaposed across the aquitard, the head value of one fluid type is converted to an equivalent head of the other fluid type (depending on the direction of leakage), and leakage fluxes are presumed to enter the receiving water body (e.g. freshwater flows into saltwater) without modifying its salinity. Huyakorn et al. (1996) developed a sharp-interface numerical model of SWI in multi-layer aquifers based on Essaid's (1990) methodology, except with modified assumptions regarding vertical leakage. They implemented three different conditions for areas of overlying freshwater and saltwater: (1) downward freshwater leakage is prohibited where freshwater is underlain by saltwater; (2) saltwater cannot leak upward where it is overlain by freshwater; (3) the upward leakage of freshwater that is overlain by an aquifer containing both freshwater and saltwater (separated by a freshwater-saltwater interface) bypasses the saltwater in the upper aquifer to flow into the overlying freshwater. In the sharp-interface SWI package for MODFLOW (Bakker et al., 2013), vertical leakage occurs only between water bodies of the same type, despite that saltwater may separate the freshwater bodies. Hence, freshwater may bypass saltwater in leaking upwards, in a similar manner to the third condition of Huyakorn et al. (1996). The upward vertical leakage of freshwater into an aquifer containing only saltwater is converted to saltwater (without modifying the saltwater salinity). The SWI package has been assessed for stratified aquifer conditions by comparing to SEAWAT results (Dausman et al., 2010; Bakker et al., 2013; Fitts et al., 2014), but the implications of the different assumptions to vertical flow have not been assessed previously. In particular, the effect of vertical leakage on the distribution of the freshwater-saltwater interface in multi-layer aquifers, when the sharp-interface approach is applied, has not been examined.

In this study, we consider SWI in layered aquifers where upward freshwater leakage occurs. Steady-state and transient predictions using both sharp-interface and dispersive

models are evaluated, and compared to the results of sand-tank experiments. Sand-tank experiments have been used previously to study SWI mechanisms, although mostly for homogeneous settings (e.g. Zhang et al., 2002; Goswami and Clement, 2007; Werner et al., 2009; Luyun Jr et al., 2009; Shi et al., 2011). Experiments of stratified aquifers are rare. Lu et al. (2013) used sand tanks and dispersive modelling to investigate the effects of aquifer stratification on the thickness of steady-state mixing zones. Various aquifer-aquitard hydraulic conductivities, layer thicknesses, head gradients and dispersivities were simulated in three-layered aquifer arrangements. The dependency of the mixing zone on these parameters was assessed. Lu et al. (2013) showed that the interface position is seaward in comparison to the homogeneous case when a low hydraulic conductivity (K; L/T) layer is embedded between two high-K layers. Sensitivity analyses of large-scale layered aquifers indicated significant effects of aquifer stratification on flow paths and the flow rate near the coastal boundary. The mixing zone profile was dependent on the K contrast rather than the magnitude of K. Sand-tank experiments and steady-state analytical solutions have also been applied by Liu et al. (2013) for stratified aquifers where a high-K layer occurs between two lower K layers. They found a reduced SWI extent with the introduction of the high-K interlayer. Their attempts to apply the sharp-interface analytical solution of Pistiner and Shapiro (1993) for layered aquifers produced discrepancies that Liu et al. (2013) attributed to vertical leakage effects that are ignored in the solution. Their results highlight the importance of both geological stratification and vertical flow effects in controlling the wedge configuration.

3.2. Methodology

The vertical leakage assumptions of sharp-interface SWI models of layered aquifers were assessed in this study using three approaches. Firstly, laboratory sand-tank experiments were used to develop a physical basis for assessing interface characteristics in a coastal system comprised of two coarse-sand aquifers separated by a fine-sand layer. Laboratory experiments allowed for a representation of SWI in a layered system that was independent of the assumptions inherent in mathematical models. Secondly, dispersive, density-dependent flow and transport modelling was used to assess the laboratory results, in particular to provide quantification of vertical fluxes within the

sand-tank experiments since measuring the vertical leakage across the lower-permeability middle layer was not possible in our experiments. Thirdly, sharp-interface models in which vertical leakage was modified to test different leakage approaches were developed. Dispersive and sharp-interface models were compared for hypothetical stratified aquifers at the field scale to assess vertical leakage assumptions under more realistic conditions. Surface recharge is neglected for simplicity in this study. Surface recharge produces a modifying effect on SWI, as shown by Mahesha (2001), and therefore, the results of the analysis that follows may over-estimate the SWI that is likely to occur in areas that experience significant recharge.

3.2.1. Laboratory experiments

Experiments were conducted in a sand tank with internal dimensions 1170 mm length, 600 mm height and 52 mm width. The front and back of the tank were constructed with transparent plate glass of 10 mm thickness, supported by rectangular steel framing. Twelve inflow/outflow taps were installed at 50 mm intervals along the sides. A schematic diagram of the experimental set up is shown in Figure 3.1.

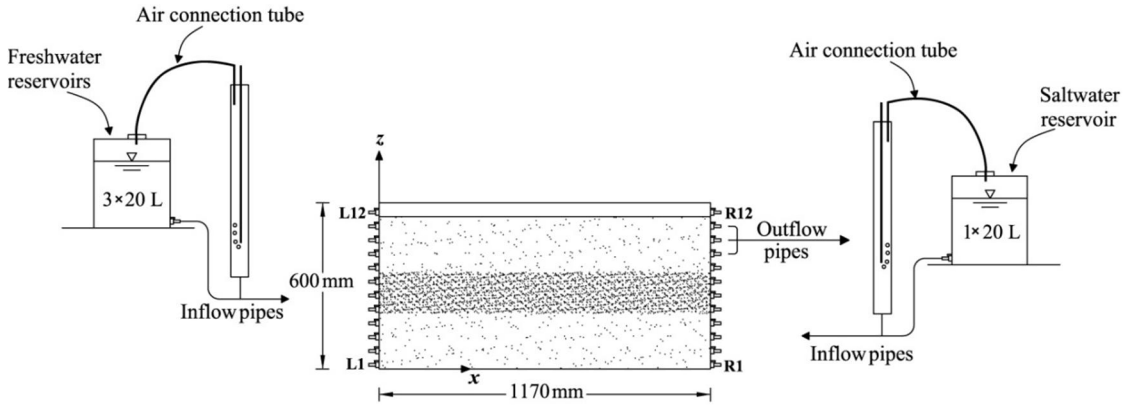

Figure 3.1. Schematic diagram of the experimental set up.

Boundaries were controlled using constant head reservoirs (i.e. freshwater and saltwater interconnected Mariotte bottles). Freshwater entered the tank via L2 to L11 taps, while saltwater inflow occurred via R2 to R7 taps (Figure 3.1). Mixed water discharged from the system via R9 to R11 taps. Three manometers were attached to taps L1, R1 and R8 to measure the heads at the boundaries. All head-control devices were placed at known

elevations, with both water and air interconnected in the same manner as adopted by Klute and Dirksen (1986).

The stratified aquifer consisted of three horizontal layers. Coarse sand (i.e. '16-30' grade sand, Sloan Sands P/L, Dry Creek, South Australia) was used for the top and bottom layers, with layer thicknesses of 25 cm and 20 cm, respectively. The middle layer was 10 or 15 cm thick (see Table 3.1) and comprised fine sand (i.e. 'N-30' grade sand, Sloan Sands P/L). A wet-packing method similar to that described by Ataie-Ashtiani (1998) was used to minimize entrapped air and non-uniform compaction.

Saltwater solution was produced by dissolving 35 g of calcium chloride dehydrate ($CaCl_2.2H_2O$) in 1 L of tap water. The salinity and density of tap water were tested. The electrical conductivity was 480 (±20) μs/cm at 16 (±1)^oC, and the total dissolved ion concentration was 280 mg/L. Rhodamine WT (fluorescent FWT Red dye, ENVCO, Australia) with concentration of 500 mg/L was used for visual monitoring of the saltwater wedge. The rhodamine tracer has been used successfully in previous studies (e.g. Schincariol and Schwartz, 1990; Simmons et al., 2002; Werner et al., 2009; Shi et al., 2011). Slight adsorption of rhodamine was found in our experiments, although we anticipate that the impacts on the results were negligible given that Jakovovic et al. (2012) found that adsorption influenced only the slowest of their up-coning experiments, and had essentially no bearing on steady-state distributions of saltwater.

For each experiment, the tank was initially filled with freshwater with all saltwater taps closed. Freshwater and saltwater reservoirs were adjusted to obtain predefined hydraulic gradients, and the experiment commenced through the introduction of saltwater into the sand tank. The salinity and discharge of outflow from the tank were measured at the end of each steady-state experiment.

Images of the experiments were recorded by an eight mega-pixel digital camera. During the transient development of steady-state conditions, pictures were taken at 15 min intervals. The experiments were assumed to have reached steady-state conditions when the toe position of the saltwater wedge remained constant in two consecutive pictures. After steady state was achieved, the freshwater head at the left boundary was lowered to

a new h^{f0} (according to Table 3.1) and the ensuing transient SWI was photographed every 5 min. Limitations in the experimental apparatus did not allow for an instantaneous change, i.e., after lowering the Mariotte bottle, approximately 30 sec passed before the air entry tube resumed bubbling.

The sand's K was estimated using two methods: (1) grain-size analysis and application of the Kozeny–Carman formula (Freeze and Cherry, 1979); and (2) constant head (Darcy column) testing. Sieve analyses produced grain-size distributions (for the coarse sand) yielding d_{10}, d_{50}, and d_{60} of 0.57, 0.64 and 0.78 mm, respectively. The uniformity coefficient (d_{60}/d_{10}) was 1.37. Fine sand values of d_{10}, d_{50} and d_{60} were 0.24, 0.41 and 0.47 mm, respectively, and the uniformity coefficient was 1.96. The porosity (n) was obtained from the common water saturation method (Fetter, 2001). The coarse sand n was 0.41 and the fine sand n was 0.39. The sieve grain sizes and the saturation method porosities were adopted in the Kozeny-Carman formula to produce K values of 308 m/d for the coarse sand and 43 m/d for the fine sand.

The Darcy column comprised a Plexiglas cylinder of 37 cm height and 5 cm internal diameter. Constant-head tests were carried out at least three times, and using different methods of Darcy column packing, producing average values of K for coarse and fine sand of 269 m/d and 40 m/d, respectively. After a series of model runs, the average K derived from Darcy column testing was adopted because it produced more satisfactory predictions of the laboratory observations. The saturation and drainage method described by Johnson (1967) was implemented to determine the specific yield (S_y). The resulting S_y value for the coarse sand upper layer was 0.33.

Salinity breakthrough curves from Darcy column tests were used to develop time series of the dimensionless concentration C/C_0, where C_0 refers to the input concentration. These were fitted to the one-dimensional analytical solution of Ogata and Banks (1961) to determine longitudinal dispersivity (α_L). The resulting value for α_L of 4 mm produced a satisfactory match to both coarse and fine sand column experiments. The transverse dispersivity (α_T) was assumed to be $1/20^{th}$ of longitudinal dispersivity, following Jakovovic et al. (2011). Table 3.1 summarizes the experimental parameters.

Table 3.1. Parameters of laboratory experiments, where SS-1 and SS-2 refer to two steady-state experiments and TS refers to transient state, which started after SS-1.

Parameters	SS-1	SS-2	TS
Freshwater head, h^{f0}(m)[a]	0.556	0.526	0.550
Saltwater head, h^{s0} (m)[a]	0.538	0.510	0.538
Top/middle/bottom layer thickness (m)	0.25/0.15/0.20	0.25/0.10/0.20	0.25/0.15/0.20
Total time (min)	430	370	270
All experiments			
Freshwater density, ρ_f (kg/m^3)	1000.16		
Saltwater density, ρ_s (kg/m^3)	1024.20		
Saltwater concentration, C_0 (kg/m^3)	33.65		
Top/middle/bottom layer K (m/d)	269/40/269		
Top/middle/bottom layer n (-)	0.41/0.39/0.41		
Top layer S_y (-)	0.33		
α_L, α_T (m)	0.004, 2×10^{-4}		

[a]The elevation of the sand tank base is considered as the datum.

3.2.2. Sharp-interface model

In sharp-interface approaches, freshwater and saltwater are assumed immiscible and a line of pressure equivalence exists between the two water bodies. Freshwater and saltwater flows are determined from continuity of flux and pressure, integrated vertically to develop differential equations describing the hydraulic head and interface distributions. The method is based on the following assumptions: (1) the Dupuit approximation and Darcy's law are valid; (2) aquifer and fluid properties remain constant in time; and (3) in layered aquifers, the aquitard has no storage, and flow and transport occur vertically across it. The equations for freshwater and saltwater motion within aquifer unit m, which is overlain and underlain by aquitard units m+1 and m, respectively (Figure 3.2), are as follows (Huyakorn et al., 1996):

$$\nabla.(K_m^f b_m^f \nabla h_m^f) + \beta_T^f \lambda_{m+1}^{'f}(h_{m+1}^f - h_m^f) + \beta_B^f \lambda_m^{'f}(h_{m-1}^f - h_m^f) = b_m^f S_{sm}^f \frac{\partial h_m^f}{\partial t} + n\eta \frac{\partial h_m^f}{\partial t} - n\frac{\partial Z}{\partial t} - Q_m^f \quad (3.1)$$

$$\nabla.(K_m^s b_m^s \nabla h_m^s) + \beta_T^s \lambda_{m+1}^{'s}(h_{m+1}^s - h_m^s) + \beta_T^s \lambda_{m+1}^{'s}(h_{m-1}^s - h_m^s) = b_m^s S_{sm}^s \frac{\partial h_m^s}{\partial t} + n\frac{\partial Z}{\partial t} - Q_m^s \quad (3.2)$$

Here, superscripts *f* and *s* refer to freshwater and saltwater, respectively. K represents the layer-averaged hydraulic conductivity [LT^{-1}], assumed to be the same in both freshwater and saltwater zones for simplicity; b is the thickness of freshwater/saltwater [L]; h is the head of freshwater/saltwater [L]; Q is the sink/source flux per unit volume of aquifer [LT^{-1}]; η is equal to 1 for unconfined and 0 for confined conditions; S_s is the specific storage [L^{-1}] (bS_s has to be replaced by S_y+bS_s for unconfined conditions); $\lambda'=K'/b'$ is the aquitard conductance [T^{-1}]; K' is the aquitard hydraulic conductivity [LT^{-1}]; b' is the aquitard thickness [L]; Z is the interface elevation above the datum [L]; β_T and β_B are dimensionless factors that are 1 or 0 depending on, respectively, the presence or absence of leakage through the top and bottom of the aquifer.

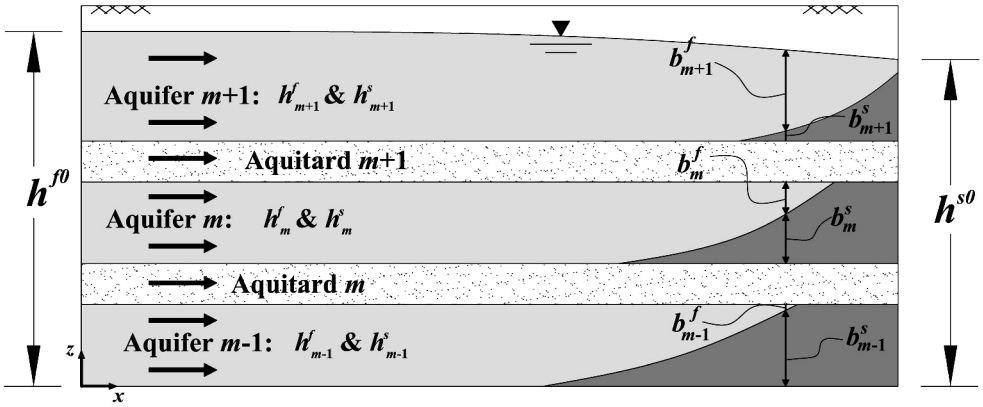

Figure 3.2. Conceptual model of a multi-layer aquifer system.

The interface elevation is given by Equation (3.3), and the freshwater and saltwater thicknesses can be determined from Equations (3.4) and (3.5), respectively.

$$Z = (1+\delta)h^s - \delta h^f \tag{3.3}$$

$$b^f = Z_T - Z \tag{3.4}$$

$$b^s = Z - Z_B \tag{3.5}$$

Here, $\delta = \rho_f / (\rho_s - \rho_f)$, where ρ_f and ρ_s are freshwater and saltwater densities [ML^{-3}], respectively, Z_B and Z_T are the elevations of the base and top of aquifer [L], respectively. h^f replaces Z_T in unconfined conditions. The position of the interface at the sea boundary is determined in the model by the approximation of Bear and Dagan (1964) that is dependent on the freshwater discharge, in a similar manner as described by Huyakorn et al. (1996).

Equations (3.1) and (3.2) are non-linear partial differential equations that are solved simultaneously for freshwater and saltwater heads. Z must be replaced in terms of h^f and h^s in Equations (3.1) and (3.2) according to Equation (3.3). Once Equations (3.1) and (3.2) are solved, the interface elevation can be obtained from Equation (3.3). The solution scheme involves a cell-centered finite-volume formulation (Bouzouf et al., 2001). The equations are linearized by adopting freshwater and saltwater thicknesses from the previous iteration. An implicit scheme is implemented for the discretization of time in transient modelling. A central-difference scheme is used to resolve the spatial gradient of heads. The tri-diagonal matrix algorithm (TDMA) is applied to solve the matrix of factors (Conte and De Boor, 1972) with an under-relaxation factor of 0.50. Head differences between two consecutive iterations are used to assess convergence.

Leakage across aquitards is calculated using three alternative methods. The first approach (Case 1) follows that of Huyakorn et al. (1996) in which water of one type only leaks into water of the same type. Where there is upward freshwater leakage into an overlying aquifer containing both freshwater and saltwater, the freshwater bypasses the saltwater in the upper aquifer and is treated as inflow to the overlying freshwater. Any downward leakage of saltwater similarly bypasses underlying freshwater such that it is added to saltwater in the aquifer below. The second method (Case 2) involves no leakage in areas of overlying freshwater and saltwater. The third method (Case 3) is based on Essaid (1990), whereby upward-leaking freshwater is converted to saltwater where it is overlain by saltwater, at a rate that is governed by the difference in hydraulic heads across the aquitard (after converting to equivalent saltwater head). Downward saltwater leakage is prevented in this method where there is underlying freshwater. The values of the β parameter are provided in Table 3.2 for implementing leakage assumptions in the three different cases.

Table 3.2. Description of the vertical leakage schemes in three different leakage cases.

Parameter	Constraint in the modelling	Description of constraint
Case 1. $\beta_T^s = 1$, $\beta_T^f = 1$, $\beta_B^s = 1$, $\beta_B^f = 1$ with the exception of the following:		
$\beta_T^s = 0$	if $h_m^s > h_{m+1}^s$ and $b_m^f \neq 0$	Saltwater in aquifer *m* does not leak upward when it is overlain by freshwater
$\beta_T^f = 0$	if $h_{m+1}^f > h_m^f$ and $b_{m+1}^s \neq 0$	Freshwater does not leak downward into aquifer *m* when there is overlying saltwater
$\beta_B^s = 0$	if $h_{m-1}^s > h_m^s$ and $b_{m-1}^f \neq 0$	Saltwater does not leak upward into aquifer *m* when there is underlying freshwater
$\beta_B^f = 0$	if $h_m^f > h_{m-1}^f$ and $b_m^s \neq 0$	Freshwater in aquifer *m* does not leak downward when it is underlain by saltwater
Case 2. $\beta_T^s = 0$, $\beta_T^f = 0$, $\beta_B^s = 0$, $\beta_B^f = 0$ With the exception of the following:		
$\beta_T^s = 1$	if $b_m^s = b_m$ and $b_{m+1}^s \neq 0$	Saltwater leakage occurs when there is juxtaposed saltwater in aquifers *m* and *m*+1
$\beta_T^f = 1$	if $b_m^f \neq 0$ and $b_{m+1}^f = b_{m+1}$	Freshwater leakage occurs where there is juxtaposed freshwater in aquifers *m* and *m*+1
$\beta_B^s = 1$	if $b_m^s \neq 0$ and $b_{m-1}^s = b_{m-1}$	Saltwater leakage occurs where there is juxtaposed saltwater in aquifers *m* and *m*–1
$\beta_B^f = 1$	if $b_{m-1}^f \neq 0$ and $b_m^f = b_m$	Freshwater leakage occurs where there is juxtaposed freshwater in aquifers *m* and *m*–1
Case 3. Case 2 constraints are applied, except where:		
$\beta_T^f = 1$	if $h_m^f > h_{m+1}^f$, $b_m^f \neq 0$ and $b_{m+1}^s \neq 0$	Freshwater in aquifer *m* leaks upward and is added to saltwater in the overlying aquifer
$\beta_B^s = 1$	if $h_{m-1}^f > h_m^f$, $b_{m-1}^f \neq 0$ and $b_m^s \neq 0$	Freshwater in aquifer *m*–1 leaks upward and is added to saltwater in aquifer *m*

To verify the model, it was compared to existing steady-state analytical solutions for homogeneous aquifers (e.g. Glover, 1959; Verruijt, 1968). Transient outputs were assessed by comparing to the experimental data of Bear and Dagan (1964) for a homogenous aquifer. Model verification for a multi-layer aquifer was achieved by comparing with Mualem and Bear's (1974) steady-state analytical solution, which they

solved for a Hele-Shaw experiment. In both homogeneous and layered aquifer cases, the interfaces were in reasonable agreement with both analytical solutions and experimental observations. Errors in the position of the steady-state toe ranged from 3% (for a homogeneous simulation) to 31% (for the upper layer of a heterogeneous simulation and using the Case 3 assumption).

3.2.3. Dispersive model

The present study used SEAWAT (version 4) to evaluate laboratory experiments and the various approaches to leakage in the sharp-interface models. SEAWAT is widely used and explained in detail in the reference manual (Langevin et al., 2008), and hence is not described here for brevity. SEAWAT's vertical water fluxes (F; L/T) through the aquitard were obtained from the water budget output of the code. An evaluation of salt concentrations (C; M/L^3) in the aquifers provided indication of the leakage situation (i.e. freshwater/saltwater fluxes to freshwater/saltwater receiving bodies). For the purposes of comparing dispersive and sharp-interface leakage fluxes, dispersive model fluxes required a classification strategy to characterize the water types into "freshwater" and "saltwater". That is, where the salinity of the uppermost cell in the aquifer layer was less than 50% of seawater, it was presumed that at least part of the aquifer contained freshwater. Where the maximum salinity within a vertical profile in the aquifer layer exceeded 50% of seawater, it was presumed that the receiving body at least partly comprised saltwater. These conditions were used to characterize aquitard leakage, including, for example, the length of aquitard over which upward freshwater leakage into overlying saltwater occurred. SEAWAT fluxes across the middle of aquitard were chosen for comparison with sharp-interface leakage between aquifers. This approach to interpreting the dispersive modelling results was necessary for comparative purposes, and to account for freshwater occurring below saltwater within an aquifer unit in the dispersive model (which is not possible in the sharp-interface models) due to upward freshwater leakage from the aquifer below.

3.2.4. Modelling scenarios

In simulating the three laboratory experiments, the parameters given in Table 3.1 were used in both sharp-interface and dispersive simulations. Constant freshwater and saltwater head values of h^{f0} and h^{s0} were adopted at the inland and seaside boundaries, respectively. No-flow boundary conditions were assigned to the top and the bottom of the aquifer, except for the unconfined case, in which the aquifer top boundary condition was the water table elevation. In the sharp-interface approach, a uniform rectangular grid with cell size Δx = 2 cm was used. The head convergence criterion was 0.001 cm and the time interval was set to 1 min for transient simulations.

SEAWAT simulations of the laboratory experiments required additional parameters to those given in Table 3.1. Time stepping was set to 30 sec and 3 sec for solving the flow and transport solutions, respectively. The uniform grid size (Δx=0.005 m and Δz=0.004 m) produced a Peclet number of 1.25, which is less than the recommended value of 4 (Voss and Souza, 1987). Flow and transport were explicitly coupled and solved using the pre-conditioned conjugate-gradient and the generalized conjugate-gradient solvers for flow and transport solutions (Langevin et al., 2008), respectively. A Courant number of 0.75 was selected for the advection package and the molecular diffusion coefficient (D_m) was set to 8.64×10^{-5} m^2/d. Three stress periods were defined for transient simulations. Steady-state conditions were obtained during the first stress period by adopting constant heads at the seaside and inland boundaries, and running the model for a sufficiently long time (i.e. 720 min). In the second stress period, the head at the freshwater boundary was lowered in 30 sec. Finally, the model was run until it reached the new steady-state condition.

Simulations representing a layered, field-scale coastal aquifer were undertaken to compare the three freshwater leakage assumptions at more realistic scales, and to assess the performance of the leakage assumptions under more extreme conditions than were possible with the laboratory apparatus. The system geometry and the soil and fluid properties (Table 3.3) were adopted from the hypothetical layered aquifer considered by Post et al. (2013), except that we adopt a vertical boundary at the shoreline to impart consistency between the dispersive and sharp-interface models. The aquifer extends 1000 m inland. The 30 m vertical profile includes two aquifer layers, each 14 m thick and separated by a 2 m aquitard. Some preliminary simulations were run to observe the

influence of truncating the Post et al. (2013) model at the shoreline (the results are not shown for brevity), and only relatively subtle differences (up to 10 m) in the position of the interface toe were obtained. A constant freshwater inflow (Q_{in}) is imposed at the inland boundary (producing flux-controlled conditions; Werner et al (2012), Post et al. (2013)), and other boundary conditions follow the same concepts as the tank-scale models. Similar to the laboratory-scale models, the field-scale model domain is subdivided using a uniform grid size (see Table 3.3) to satisfy the desired Peclet number.

Table 3.3. Field-scale aquifer parameters.

Parameters	Values
ρ_f, ρ_s (kg/m^3)	1000,1025
C_0 (kg/m^3)	35
h^{s0} (m)	30
Upper/lower aquifer K (m/d)	10/10
α_L, α_T (m)	0.5, 0.05
Upper/middle/lower layer n (-)	0.35/0.2/0.35
SEAWAT cell size (m)	Δx=1, Δz=0.5
Sharp-interface model cell size (m)	Δx=5

Field-scale simulations involved eight different scenarios, which differ in the values of K' and Q_{in} (see Table 3.4). In all cases, the total Q_{in} through the inland boundary (i.e. the sum of upper layer inflow, Q_u, and lower layer inflow, Q_l) was 0.548 m^2/d. The value of K' varied between K (i.e. a homogeneous case) and $K/10^5$ (see Table 3.4).

Table 3.4. Parameter differences between the eight field-scale scenarios

Scenario	Q_u:Q_{in}	Q_l:Q_{in}	K:K'
1	1:1	1:1	1:1
2	0.5:1	0.5:1	1000:1
3	1/11:1	10/11:1	1000:1
4	10/11:1	1/11:1	1000:1
5	1/11:1	10/11:1	100:1
6	1/11:1	10/11:1	10:1
7	1/11:1	10/11:1	100000:1
8	1/101:1	100/101:1	100000:1

3.3. Results

3.3.1. Evaluation of laboratory experiments

The laboratory results of SS-1, SS-2 and TS experiments are presented in Figure 3.3. In SS-1, no saltwater is apparent in the middle layer of fine sand, whereas the middle layer and upper aquifer clearly contain saltwater in SS-2. Salinity contours (5%, 50% and 95%) from the SEAWAT model are compared against the laboratory images, and demonstrate largely reasonable matches for the two steady-state experiments, albeit SEAWAT over-predicts the saltwater extent of SS-1. In the TS experiment (Figure 3.3c and 5.3d), the model produces the general observed shape of the wedge, but over-predicts significantly the extent of saltwater in the lower layer. This may be attributable to several differences between the model and the experimental conditions. For example, in order to have the same boundary type as in the sharp-interface approach, the seaside specified-head boundaries are continuous in the model, whereas point inflows were imposed in the laboratory tests. Additionally, some degree of heterogeneity, e.g. due to non-uniform packing, was unavoidable in the sand-tank, whereas the model assumes homogeneous conditions. It is also apparent that a wider mixing zone is produced by SEAWAT compared to the laboratory experiments. Alternative SEAWAT solution schemes (i.e. finite-difference method, hybrid method of characteristics, and 3rd-order TVD scheme) and dispersion parameters (2 mm $\leq \alpha_L \leq$ 4 mm; $0 \leq D_m \leq 8.64\times10^{-5}$ m^2/d) based on studies adopting similar materials (e.g. Jakovovic et al., 2011; Lu et al., 2013;

Dose et al., 2014; Liu et al., 2014) were tested to evaluate the influence on the mixing zone thickness. While the TVD scheme gives slightly narrower mixing zones, the simulated mixing zone is still wider than the laboratory observations.

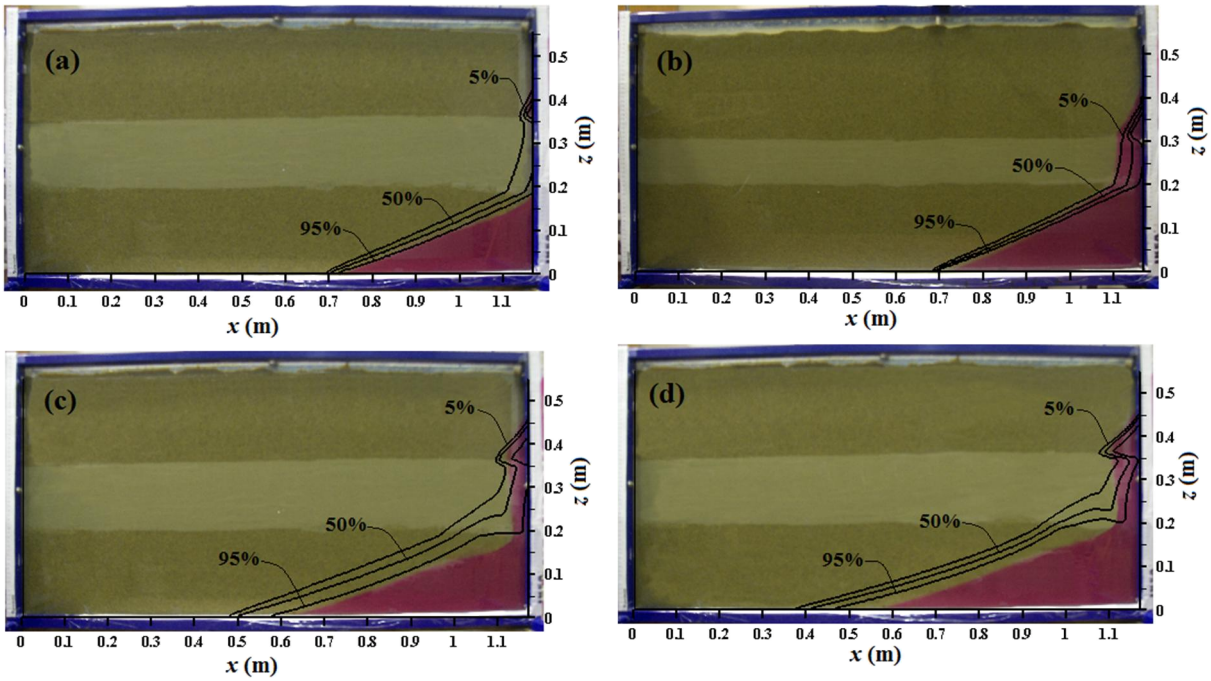

Figure 3.3. Saltwater distributions in laboratory experiments compared to SEAWAT salinity contours: (a) SS-1, (b) SS-2, (c) TS after 120 min, and (d) TS after 270 min.

The laboratory experiments involved only small zones in which overlying saltwater and freshwater occurred. The limited size of the sand tank and the need to avoid the interface toe reaching the freshwater boundary restricted the lower limit of freshwater discharge used in the experiments. Hence, it was especially challenging to produce more extensive regions of overlying freshwater-saltwater while maintaining reasonable experiment run-times and using existing infrastructure. A wider range of cases is evaluated using the numerical model and with different settings, and the sand-tank experiments serve merely to validate that the numerical model produces an adequate representation of the associated flow and transport processes.

3.3.2. Evaluation of tank-scale sharp-interface models

3.3.2.1. Steady-state modelling

The performances of multi-layer sharp-interface models are firstly evaluated for the two steady-state laboratory experiments. Figure 3.4 illustrates the comparison between simulated freshwater-saltwater interfaces for the three different leakage assumptions and those from the experiments. The modelled extent of SWI in the lower layer of SS-1 (Figure 3.4a) is similar for all three leakage cases, probably due to the small areas in the experiments where freshwater underlies saltwater. The interface extends slightly further inland in Case 3, most notably in the upper aquifer. In SS-2, Case 2 shows slightly less SWI in the upper part of the lower aquifer. These observations are consistent with the anticipated effect of the respective assumptions. That is, the lack of upward freshwater leakage in areas of overlying saltwater in Case 2 causes freshwater to discharge to the seaward boundary in the lower aquifer, and hence the model produces a freshwater outflow face below the middle layer. Saltwater in the upper aquifer receives additional inflow (in the form of freshwater from the lower layer) in Case 3. These assumptions modify both the freshwater discharge to the sea in the lower aquifer (more for Case 2 and less for Case 3), and the seawater volume in the upper aquifer (less in Case 2 and more in Case 3) close to the seaward boundary.

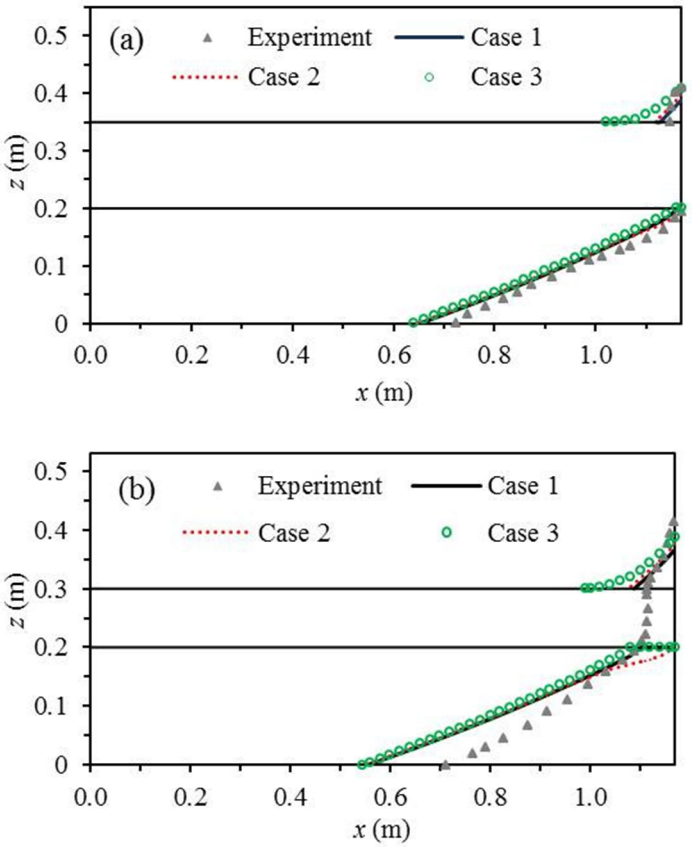

Figure 3.4. Comparisons of experimental results with sharp-interface cases for two steady-state experiments: (a) SS-1 and (b) SS-2.

Vertical leakage across the middle layer is estimated using SEAWAT. F and C values from SEAWAT are presented in Figure 3.5. Positive F values indicate upward leakage. The superscript notation here for F (e.g. F^{fs} for freshwater-to-saltwater leakage, etc.) refers to the salinity situation in overlying aquifers and not necessarily to any transformation of water types from freshwater to saltwater or vice versa. For example, F^{fs} in Case 1 refers to freshwater that bypasses overlying saltwater to become inflow to the overlying freshwater region. As Figure 3.5 shows, freshwater-to-freshwater fluxes (F^{ff}) from the sharp-interface model match well with values from the dispersive model in the freshwater area. The amount of upward freshwater leakage increases with distance from the freshwater boundary, until the saltwater wedge is encountered, and then leakage fluxes decrease closer to the saltwater boundary.

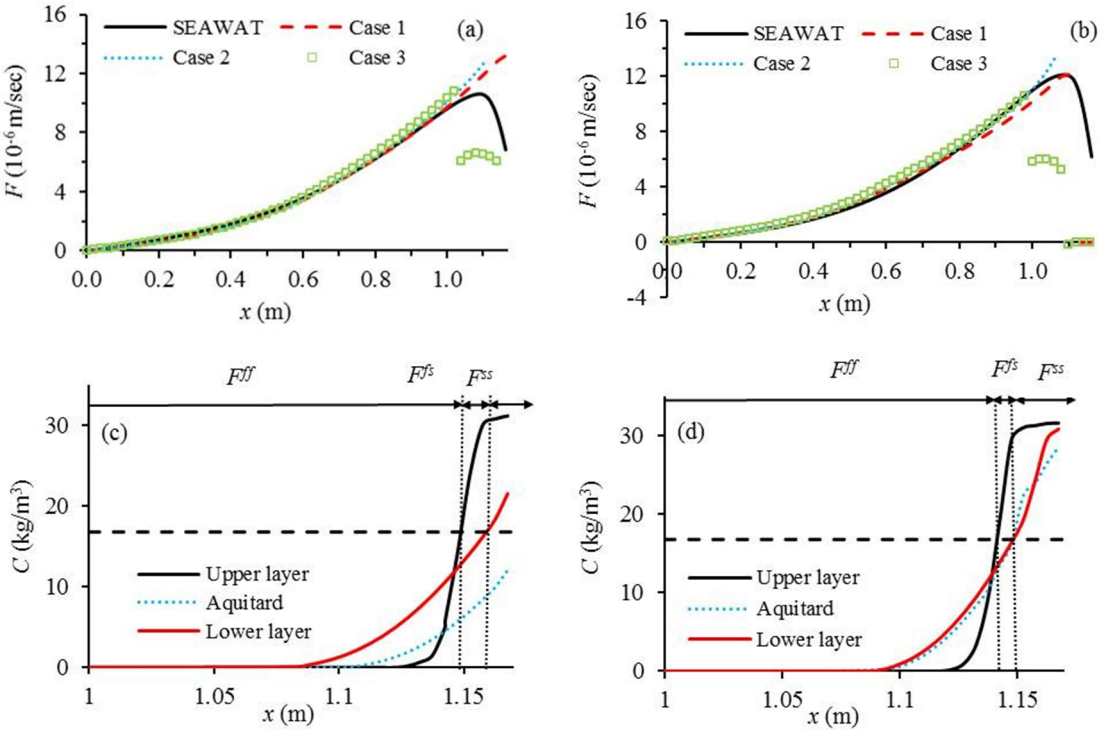

Figure 3.5. Leakage fluxes in sharp-interface and SEAWAT models: (a) SS-1, and (b) SS-2. Salinity distributions near the sea boundary from the SEAWAT model: (c) SS-1, and (d) SS-2. The dashed horizontal line separates freshwater (C<0.5C_0) and saltwater(C>0.5C_0).

In the sand-tank observations of the SS-1 experiment, there is no saltwater in the top of the lower aquifer (Figure 3.3a), and hence any upward leakage is freshwater. SEAWAT's prediction of SS-1 freshwater-to-saltwater flux (F^{fs}) is 4.0×10^{-9} m^3/sec, occurring over a distance of 1 cm. The sharp-interface model produces SS-1 values for F^{fs} of 2.7×10^{-8} m^3/sec over a distance of 4 cm from the sea boundary (Case 1), 0 m^3/sec over 6 cm (Case 2), and 4.0×10^{-8} m^3/sec over 12 cm (Case 3). Case 3's larger departure from SEAWAT fluxes and SWI extent (Figure 3.5) is consistent with the interface results of Figure 3.4. The values for F^{fs} and SWI extent in Case 1 show the best match to the SEAWAT prediction, albeit there is a significant error incurred by the sharp-interface assumptions. The saltwater-to-saltwater leakage (F^{ss}) is zero in Cases 1 and 2 (in agreement with SEAWAT), but is 1.5×10^{-10} m^3/sec over 2 cm in Case 3. This contributes to the larger saltwater plume in Case 3 in the upper layer (Figure 3.4a).

The upward saltwater leakage in SS-2 (i.e., F^{ss} of 1.2×10^{-8} m^3/sec) occurs over 2.0 cm near the sea boundary in SEAWAT (Figure 3.5b). The sharp-interface model fails to

reproduce SEAWAT's F^{ss} for all three leakage assumptions, producing 6.5×10^{-11}, 0.0 and 3.9×10^{-10} m^3/sec for Cases 1, 2, and 3, respectively. SEAWAT produced F^{fs} of 2.4×10^{-9} m^3/sec distributed over 0.5 cm for SS-2. No saltwater is found overlying freshwater in the sharp-interface models for Case 1, but Case 3 produces F^{fs} of 2.5×10^{-8} m^3/sec over 10.0 cm. The comparison of sharp-interface and SEAWAT fluxes for the SS-2 experiment follows generally similar trends to the SS-1 experiment.

3.3.2.2. Transient modelling

The sharp-interface and SEAWAT results, and experimental observations are given in Figure 3.6 for two selected times from the TS experiment. Similar to the steady-state results, transient sharp-interface models generally produce more SWI than observed in the sand tank. SWI is again slightly more extensive in Case 3 and least extensive in Case 2 in the lower aquifer, whereas in the upper aquifer, Case 3 is the most extensive and Case 1 is the least extensive, albeit the variations are subtle.

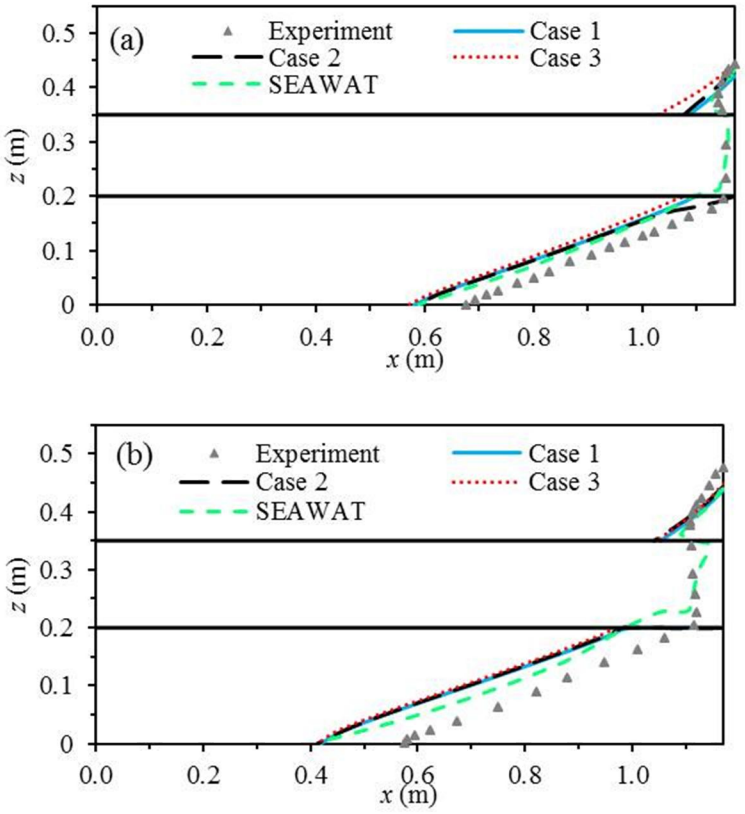

Figure 3.6. Comparison of experimental observations, sharp-interface results and the SEAWAT 50% salinity contour for the TS experiment, after: (a) 60 min, (b) 270 min.

Figure 3.7 shows simulated fluxes and salinities for the TS experiment. Again, F^{ff} values are similar in all sharp-interface cases and are consistent with SEAWAT, except near the interface. Case 1 out-performs the other cases in reproducing the transient SEAWAT F^{ss} values, e.g. after 270 min, F^{ss} values are 1.03×10^{-9}, 1.96×10^{-9}, 5.27×10^{-10} and 6.43×10^{-12} m^3/sec in SEAWAT, and Cases 1, 2 and 3, respectively. There is no upward leakage of freshwater to regions of the upper aquifer where saltwater exists in the SEAWAT transient simulation (i.e. $F^{fs} = 0$), at least for the 60 min and 270 min snapshots. In agreement with this, Cases 1 and 2 produce F^{fs} values of zero, whereas Case 3 predicts an F^{fs} of 9.8×10^{-9} m^3/sec after 60 min. SEAWAT produces saltwater-to-freshwater fluxes (F^{sf}) (e.g. 9.32×10^{-9} m^3/sec after 60 min). None of the leakage cases adopted in the sharp-interface models allow for the upward flow of saltwater into overlying freshwater systems, and hence $F^{sf} = 0$ for Cases 1 to 3. The occurrence of $F^{sf} \neq 0$ is more likely in transient rather than steady-state situations, and therefore transient models require additional modifications to the current suite of sharp-interface cases to allow for upward saltwater leakage to occur.

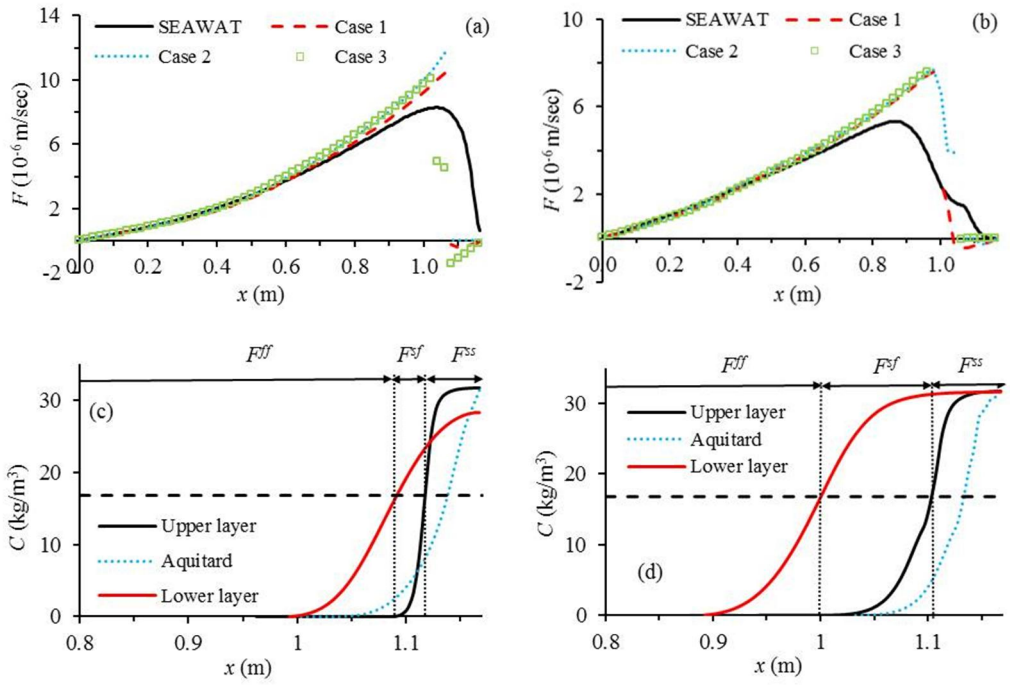

Figure 3.7. Leakage fluxes in sharp-interface and SEAWAT models for the TS experiment after: (a) 60 min, and (b) 270 min. Salinity distributions near the sea boundary from the SEAWAT model after: (c) 60 min, and (d) 270 min. The dashed horizontal line separates freshwater (C<0.5C_0) and saltwater(C>0.5C_0).

3.3.3. Evaluation of field-scale sharp-interface models

The sharp-interface results are compared to the 0.5 isochlor produced from SEAWAT in Figure 3.8, for eight field-scale scenarios. The sharp-interface models again over-predict SWI, as expected.

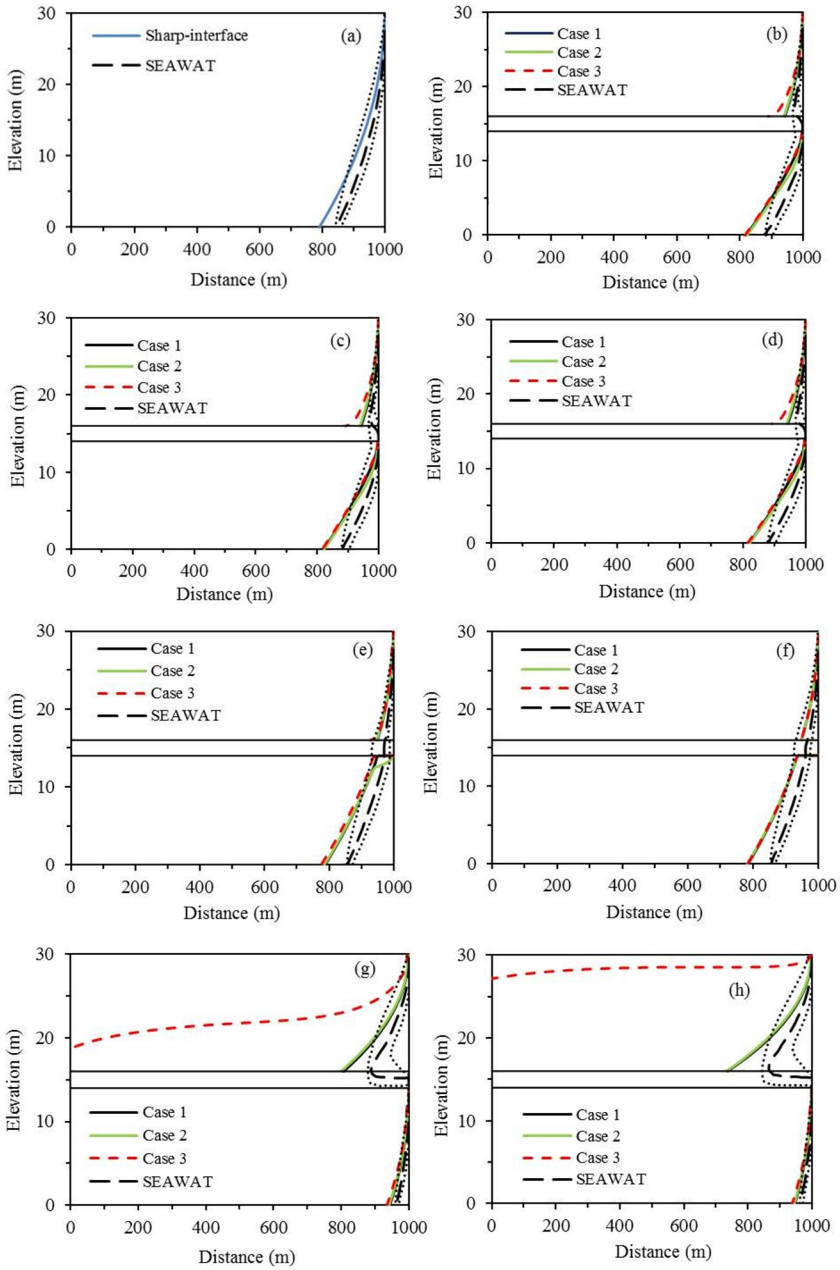

Figure 3.8. Comparison of different sharp-interface cases with SEAWAT results. (a) Scenario 1 (homogeneous aquifer); (b), (c), (d) Scenarios 2 to 4, respectively (same $K{:}K'$, different Q_{in}); (e), (f), (g) Scenarios 5 to 7, respectively (same Q_{in} as Scenario 3,

different $K:K'$); (h) Scenario 8 (same $K:K'$ as Scenario 7, different Q_{in}). The dotted lines indicate 5% and 95% salinity contours from SEAWAT.

The modest influence of modifying inflow ratios (see Table 3.4) are demonstrated by the results of Scenarios 2 to 4 (Figure 3.8b-3.8d), in which the same aquitard-aquifer K contrast is adopted. The reason that changes to the inland boundary flux distribution had only a small effect on the interface is that fluxes tend to cross the aquitard before reaching the wedge, and hence by the time the interface is reached, the fluxes in Scenarios 2 to 4 are somewhat similar. Reducing the $K:K'$ ratio (Scenarios 3, 5 and 6; Figure 3.8c, 3.8e and 3.8f), by increasing K', produced interface distributions that approach the homogeneous result (Figure 3.8a), as expected. The higher K' caused smaller regions of saltwater overlying freshwater, and the three sharp-interface cases subsequently converged.

The influence of reducing K' (Scenarios 3, 7 and 8; Figure 3.8c, 5.8g and 5.8h) served to enhance the region of saltwater overlying freshwater. The results show a substantial error associated with the application of Case 3 to situations involving low K' (Scenarios 7 and 8). In Case 3, enlargement of the upper interface is self-perpetuating, whereby upward leakage enhances the upper aquifer saltwater zone, thereby capturing more upward leakage, creating an unstable solution whereby the entire upward freshwater flow enters the overlying saltwater zone.

In all seven layered aquifer scenarios shown in Figure 3.8b-3.8h, and in the sand-tank scale results, Cases 1 and 2 produce similar interface distributions, with the exception of the lower aquifer interface near the shoreline. This can be explained by considering water budgets for the upper aquifer in regions with freshwater overlying saltwater, which receive upward leakage in Case 1, but no upward leakage in Case 2. That is, the rate of horizontal freshwater discharge in the upper aquifer, at the toe position, is considerably higher than any upward leaking freshwater in the region between the toe and sea, and this renders the differences in F^{fs} between Cases 1 and 2 as generally insignificant. For example, in Scenarios 2, 7 and 8, the upper layer freshwater flow rates at the toe position were 0.41, 0.102 and 0.072 m^3/d, respectively (Cases 1 and 2 flow rates differed by <4%). The corresponding Case 1 freshwater leakage rates were

0.005, 2.1×10^{-4} and 2.8×10^{-4} m^3/d, respectively. That is, upward F^{fs} in Case 1 is typically less than 1.2 % of ambient interface flows in all scenarios, and thus, the results of Case 1 are similar to those of Case 2, in which F^{fs} is zero.

The relative SWI extents produced by the three different sharp-interface cases are consistent with the sand-tank scale results. That is, all three sharp-interface cases produce similar interface positions in the lower layer, and differ mostly in the upper layer. Case 3 produces the most extensive SWI, and Case 1 creates marginally the least SWI, matching optimally with the SEAWAT results.

Flow streamlines from the dispersive modelling results provide important insight into the reason for the overall improved match between Case 1 sharp-interface results and SEAWAT results. The streamlines for Scenario 7 are given in Figure 3.9 to illustrate the characteristics of freshwater leakage pathways. The same general trends were observed in other simulations (these are omitted for brevity). The flow patterns show that in areas where freshwater is overlain by saltwater, upward freshwater leakage tends to flow around the overlying saltwater, thereby mostly bypassing it rather than mixing directly with it. This trend is commensurate with the Case 1 assumptions.

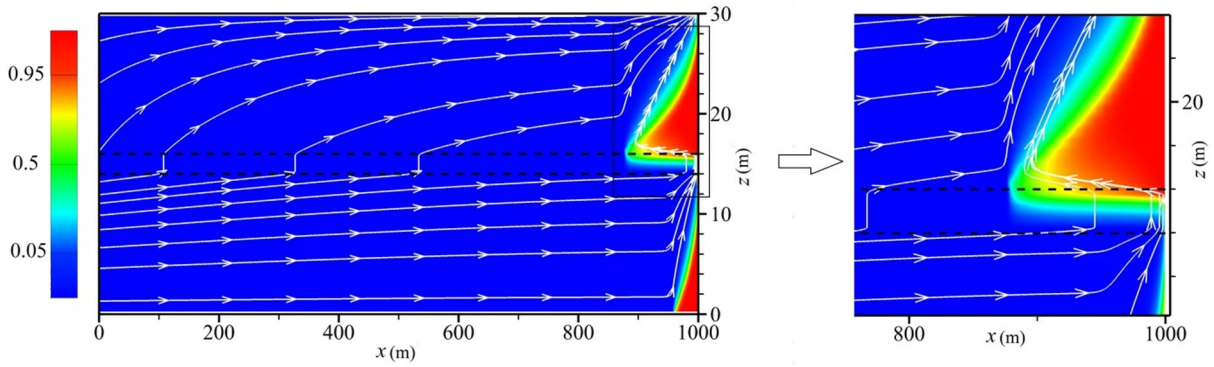

Figure 3.9. Flow streamlines for Scenario 7 (the regions where freshwater is overlain by saltwater are enlarged for better representation of flow direction). The colour scale represents relative salt concentrations, where 1.0 is seawater.

3.4. Conclusions

Sharp-interface seawater intrusion models of layered aquifers require simplifying assumptions regarding the upward flux of freshwater to overlying aquifers containing saltwater. We test three alternative sharp-interface modelling strategies for treating upward freshwater leakage through aquitards, based on the assumptions of previous studies: Case 1 involves freshwater bypassing any overlying saltwater, Case 2 assumes no upward freshwater leakage where there is overlying saltwater, and Case 3 transforms the upward freshwater leakage into saltwater. Firstly, two-dimensional sand-tank experiments of layered aquifer situations, evaluated using a dispersive numerical model (SEAWAT), are compared to the results of sharp-interface models with alternative leakage assumptions. Secondly, SEAWAT and the sharp-interface models are then compared for idealized field-scale simulations.

The results indicate that Case 1 produces optimal matches to both SEAWAT results and sand-tank observations, in terms of both the saltwater wedge location and the upward freshwater leakage rate and distribution, albeit all sharp-interface models over-predict the extent of saltwater, both in steady-state and transient conditions. The restriction of upward freshwater leakage in Case 2 creates freshwater outflow faces at the sea boundary of the lower aquifer that are not otherwise expected. Aside from this, Cases 1 and 2 were largely in agreement, mostly because upward freshwater leakage to overlying areas containing saltwater constitutes only a small component of the upper aquifer freshwater balance, and neglecting it (i.e. in Case 2) produces fairly minor departures from the Case 1 results. The conversion of lower aquifer freshwater to upper aquifer saltwater in Case 3 produces an over-estimation of the extent of upper aquifer saltwater. In the case of field-scale systems and with low conductance between overlying aquifers, Case 3 produces an unstable situation of complete salinization of the upper aquifer, in contradiction to the other methods. Freshwater-to-freshwater fluxes in areas where saltwater is absent were largely consistent across the three sharp-interface cases, relative to SEAWAT. None of the sharp-interface cases were able to reproduce SEAWAT's prediction of saltwater-to-saltwater fluxes in both laboratory- and field-scale simulations.

Streamlines predicted by the dispersive model highlight that the assumptions of Case 1 are best matched to the physical processes of upward freshwater leakage in the aquifers

considered here. That is, upward freshwater leakage from the lower aquifer trends to flow around and bypassing overlying saltwater, adding freshwater inflows to the upper aquifer freshwater zone, rather than mixing directly with the saltwater. Our findings lead to the recommendation that Case 1 is the optimal approach for the treatment of upward freshwater leakage in sharp-interface models of multiple aquifers. Further research is required to extend the current study to systems involving more extensive regions of saltwater in an upper aquifer overlying freshwater in a lower aquifer, to ascertain the conditions under which buoyancy forces create rising freshwater bubbles in the upper aquifer saltwater zone.

4. ON THE CHARACTERISTICS OF ACTIVE SEAWATER INTRUSION

4.1. Introduction

Seawater intrusion (SWI) is a phenomenon where seawater displaces fresh groundwater in coastal aquifers (Bear, 1979). The global significance of SWI is well-established (Wu et al., 1993; Bocanegra et al., 2010; Custodio, 2010; Werner et al., 2013b). Previous studies have recognized two types of SWI: passive and active (Mahesha, 1995; Morgan et al., 2012; Werner et al., 2012). In passive SWI, the hydraulic gradient slopes towards the sea. This results in density-induced forces acting in the opposite direction to fresh groundwater flow, creating the classical wedge-shaped seawater plumes that are traditionally associated with SWI (e.g., Pinder and Cooper, 1970). In active SWI, the hydraulic gradient slopes towards the land, and forces caused by density differences and fresh groundwater flow act in the same direction, causing more aggressive salinization.

The current understanding of SWI is based primarily on studies that assume a steady-state condition (Werner et al., 2013a). For example, a considerable body of SWI research adopts the Henry problem (Henry, 1964), and modifications thereof, to investigate the effects of density, heterogeneities and dispersion on steady-state SWI (e.g., Simpson and Clement, 2003; Held et al., 2005; Abarca et al., 2007; Sebben et al., 2015). Several studies use the shift in the interface between one steady-state condition and another in evaluating long-term extents of SWI (e.g., Werner and Simmons, 2009; Morgan et al., 2012), thereby neglecting altogether transient effects and precluding the evaluation of active SWI processes. Morgan et al. (2012) showed that if the freshwater-saltwater interface moves slowly enough, steady-state solutions reproduce approximately the transient interface. This permits use of quasi-equilibrium predictions of the transient interface, thereby avoiding the numerical burden of transient analyses.

Previous studies of the transience of SWI have mainly considered passive SWI (e.g., Chang et al., 2011; Webb and Howard, 2011; Morgan et al., 2015). For example, Watson et al. (2010) investigated transient SWI in response to both sea-level rise (SLR)

and sea-level drop in unconfined coastal aquifers, and defined a SWI response time-scale as the time needed for the freshwater-saltwater interface toe (i.e., the inland limit of the saltwater wedge along the aquifer basement) to reach 95% of the new steady-state condition. They observed temporal asymmetry in the SWI responses to rises and falls in sea level, and discovered the phenomenon known as 'SWI overshoot' (e.g., Morgan et al., 2013c). Following Watson et al. (2010), Lu and Werner (2013) employed the same definition of SWI time-scales in their investigation of response times associated with passive SWI, created by variations in the inland or coastal water level. They showed that for a particular coastal aquifer, the SWI response time-scale is determined by the final boundary head difference (i.e., the difference between inland and coastal boundary heads after an inland freshwater head decline (FHD)), regardless of the toe response distance associated with particular FHD events. In contrast, the toe response distance controls the time-scale of seawater retreat for cases with the same initial boundary head differences.

Compared to passive SWI, active SWI has received considerably less research attention, and general intuition about the controlling factors and time-scales of active SWI is under-developed, despite that active SWI is known to occur in many areas (i.e., Yakirevich et al., 1998; Fetter, 2001; Werner and Gallagher, 2006; Morgan and Werner, 2015). A prominent case study of active seawater intrusion is Vázquez-Suñé et al.'s (2006) investigation of the Llobregat Delta (Spain), where groundwater levels fell to more than 25 m below sea level in the 1970s, creating active SWI conditions that led to rapid and extensive salinization of the coastal aquifers. Studies of active SWI include that of Badaruddin et al. (2015), who used physical and numerical modelling to show that under active SWI conditions and in the absence of recharge, the potential for watertable salinization (WTS) was significant for non-tidal unconfined coastal aquifers. The transition from passive to active SWI, which is accompanied by cessation of fresh groundwater discharge to the sea, leads to WTS arising from the landward flow of seawater. WTS may occur at rates up to, or temporarily faster than, the speed of SWI along the aquifer base (Badaruddin et al., 2015). SWI causes more extensive WTS in tidal settings relative to non-tidal conditions (Werner and Lockington, 2006). Active SWI is largely an unstudied phenomenon from the perspective of its primary characteristics and key controlling forces. Thus, intuition on the behaviour of active

SWI is based largely on case studies, where the individual contributions of buoyancy, dispersive and advective forces to aquifer salinization are not investigated. The studies by Werner and Lockington (2006) and Badaruddin et al. (2015) did not explore the key features of active SWI and their relationships with the main system parameters, and rather, they focused on tidal effects and WTS, respectively.

This study investigates the characteristics of transient, active SWI occurring in cross section in various non-tidal, unconfined coastal aquifer settings, which are homogeneous, of simple geometry, and devoid of surface recharge. For the purpose of comparison, passive SWI conditions are also considered. Research by Badaruddin et al. (2015) and Abarca et al. (2004; 2007), who provide general guidance on steady-state SWI, are extended in this study by attempts to draw relationships between key features of active SWI (e.g., interface slope, mixing zone width and SWI time-scales) and the main controlling forces (e.g., density, dispersion and advection). We also extend the passive SWI characterisation of Lu and Werner (2013) using a modification to their approach to quantify active SWI time-scales.

4.2. Methodology

4.2.1. Conceptual model

Figure 4.1 shows a schematic representation of a simple unconfined coastal aquifer, and identifies the key parameters adopted in quantifying the main features of active SWI. The analysis applies to unconfined aquifers because these more often support freshwater extraction given their shallow occurrence relative to confined systems (Watson et al., 2010; Werner et al., 2013b).

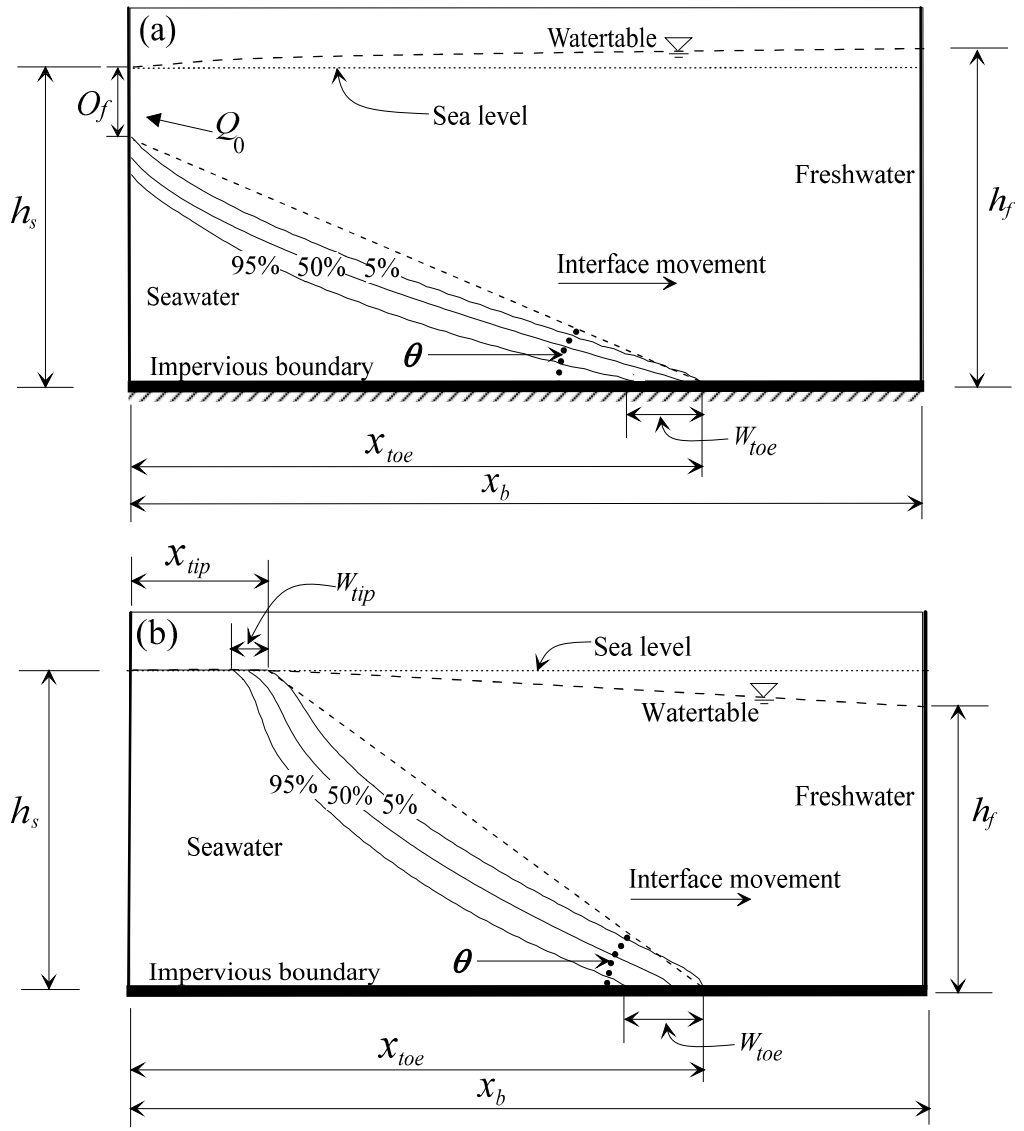

Figure 4.1. Conceptual model of an unconfined coastal aquifer subjected to: (a) passive SWI and (b) active SWI.

The left and the right sides of the conceptual model (Figure 4.1) are the coastal and inland boundaries, respectively. Q_0 [L^2/T] is freshwater discharge to the sea, and O_f [L] is the depth of freshwater discharging at the shoreline (i.e., 'outflow face'), which is shown in Figure 4.1 as the distance from the watertable to the 5% relative salinity on the ocean boundary. Obviously, O_f is dependent on the choice of relative salinity value used to define 'freshwater'. The regional head difference ($h_{f\text{-}s}$ [L]) is the advective force driving groundwater flow between the boundaries, and is represented by h_f - h_s, where h_s [L] is the depth of the horizontal aquifer base below sea level, and h_f [L] is the inland freshwater head (Figure 4.1). Surface recharge is neglected for simplicity. Recharge creates a mitigating effect on watertable salinization during active SWI, as shown by

Werner (2017), and therefore, the results of the analysis that follows may over-estimate the watertable salinization that is likely to occur in regions that experience persistent, significant recharge. Three different salinity values (i.e., 5%, 50% and 95% of seawater, termed 'relative salinity' in what follows) provide the basis for evaluating the behaviour of the interface, and both the interface toe (x_{toe} [L]) and the interface tip (x_{tip} [L]) are reported (Figure 4.1). The horizontal length between the 5% and 95% relative salinity contours is adopted as the width of the dispersion zone, which is calculated both at the interface toe (W_{toe} [L]) and at the watertable (i.e., the interface tip) (W_{tip} [L]). The interface slope (θ) is obtained from a straight line connecting the interface toe and tip.

The approach to modelling SWI is similar to numerical experiments by Lu and Werner (2013), whereby the initial interface position represents the steady-state condition, and then an instantaneous inland FHD of Δh_f [L] causes the interface to move landward. Under active SWI, there is no final steady-state condition, because the interface toe eventually intrudes to the inland boundary, unlike passive SWI, in which seawater eventually restabilises to a new location. SWI will reach the inland boundary unless h_f exceeds the equivalent freshwater head at the base of the coastal boundary (h_{base}), at least on the basis of sharp-interface theory (Werner et al., 2012). Here, $h_{base} = h_s \, \rho_s / \rho_f$, where ρ_s [M/L^3] is saltwater density and ρ_f [M/L^3] is freshwater density. Active SWI occurs if $h_f < h_{base}$.

The aquifer properties of the base case reflect those used by Lu and Werner (2013). That is, the coastal aquifer is homogeneous and isotropic, hydraulic conductivity (K) is 10 m/d, effective porosity (n) is 0.3, specific yield (S_y [-]) is 0.25, distance to the inland specified-head boundary (x_b) is 1000 m and h_s is 30 m. The values of ρ_s and ρ_f are 1025 kg/m^3 and 1000 kg/m^3, respectively. The longitudinal dispersivity (α_L) is 1 m and the transverse dispersivity (α_T) is one tenth of α_L (Lu and Werner, 2013; Abarca et al., 2007). Molecular diffusion (D_m) is 8.64 x 10^{-5} m^2/d.

The behaviour of the interface under various hydrogeological conditions and rates of passive and active SWI was explored primarily using sensitivity analysis. Table 4.1 outlines the various cases, which encompass several values of the final boundary head difference ($h'_{f\text{-}s}$) (i.e., after FHD), K, α_L, n, ρ_s and h_s, resulting in 64 SWI cases at the 1-

km scale. Negative values of $h'_{f\text{-}s}$ indicate a lower h_f relative to h_s (Table 4.1, Figure 4.1). A field-scale case, i.e., using parameters typical of the Pioneer Valley aquifer, Australia (Case 65) (Werner and Gallagher, 2006) is included. Cases 1 ($h'_{f\text{-}s}$ = 1 m) and 3 ($h'_{f\text{-}s}$ = -1 m) are the passive and active SWI base cases, respectively. In Table 4.1, Cases 1, 5, 9, … 41 represent passive SWI, and the other cases involve active SWI. We use a similar method to that adopted by Lu and Werner (2013) to seek empirical relationships between SWI response time-scales and the inland FHD.

Table 4.1. Parameter values for SWI cases.

Case	Initial h_f	Post-FHD h_f	FHD Δh_f	h_s	$h'_{f\text{-}s}$	x_b	K	n	α_L	Internal ρ_s	External ρ_s
	m	m	m	m	m	m	m/d	-	m	kg/m^3	kg/m^3
1 to 4	32	31 to 28	1 to 4	30	1 to -2	1000	10	0.30	1	1025	1025
5 to 8	32	31 to 28	1 to 4	30	1 to -2	1000	5	0.30	1	1025	1025
9 to 12	32	31 to 28	1 to 4	30	1 to -2	1000	20	0.30	1	1025	1025
13 to 16	32	31 to 28	1 to 4	30	1 to -2	1000	10	0.30	0.1	1025	1025
17 to 20	32	31 to 28	1 to 4	30	1 to -2	1000	10	0.30	10	1025	1025
21 to 24	32	31 to 28	1 to 4	30	1 to -2	1000	10	0.30	1	1020	1020
25 to 28	32	31 to 28	1 to 4	30	1 to -2	1000	10	0.30	1	1030	1030
29 to 32	28	27 to 24	1 to 4	26	1 to -2	1000	10	0.30	1	1025	1025
33 to 36	36	35 to 32	1 to 4	34	1 to -2	1000	10	0.30	1	1025	1025
37 to 40	32	31 to 28	1 to 4	30	1 to -2	1000	10	0.25	1	1025	1025
41 to 44	32	31 to 28	1 to 4	30	1 to -2	1000	10	0.35	1	1025	1025
45	31.5	29.5	2	30	-0.5	1000	10	0.30	1	1025	1025
46	32.5	30.5	2	30	0.5	1000	10	0.30	1	1025	1025
47 to 50	33 to 31.5	30.5 to 29	2.5	30	0.5 to -1	1000	10	0.30	1	1025	1025
51	31.5	28.5	3	30	-1.5	1000	10	0.30	1	1025	1025
52 to 54	33.5 to 32.5	30.5 to 29.5	3	30	0.5 to -0.5	1000	10	0.30	1	1025	1025
55	31.5	28	3.5	30	-2	1000	10	0.30	1	1025	1025
56 to 59	34 to 32.5	30.5 to 29	3.5	30	0.5 to -1	1000	10	0.30	1	1025	1025
60 to 64	34.5 to 32.5	30.5 to 28.5	4	30	0.5 to -1.5	1000	10	0.30	1	1025	1025
65	41.6	36.2	5.4	37	-0.8	4750	166	0.10	10	1025	1025

4.2.2. Numerical model

The variable-density groundwater flow and transport code SEAWAT version 4 (Langevin et al., 2008) was used to conduct numerical experiments of SWI in two-dimensional cross-sections. SEAWAT is widely applied, and has been tested against several benchmark problems (e.g., Langevin et al., 2003; Brovelli et al., 2007; Goswami and Clement, 2007). The governing equations and the numerical implementation of SEAWAT are given in the user manual (e.g., Langevin et al., 2008), and are therefore not shown here for brevity.

The base case model domain is 35 m high and 1000 m long. The mesh Peclet number (Pe_m [-]) suggested by Voss and Souza (1987) was used in specifying the discretization of the model domain:

$$Pe_m = \frac{\Delta L}{\alpha_L} < 4 \tag{4.1}$$

where ΔL [L] is the grid spacing. Initially, a uniform grid size of Δx = 1.0 m and Δz = 0.5 m was used, resulting in a grid of 70,000 cells and a Pe_m of 1. A grid-dependence test was conducted using both passive and active SWI base cases, and using alternative levels of discretization, namely (Δx, Δz) equal to (0.5 m, 0.5 m), (0.5 m, 0.25 m) and (2 m, 1 m). The simulation results showed differences of less than 1% in the transient interface locations between the initial grid spacing and finer grids, and more than 5% compared to the coarser grid model. Therefore, the initial grid spacing (1.0 m, 0.5 m) was adopted in this study. For Case 65 (the field case), the domain height was 47 m, and a uniform grid size of Δx = 10 m and Δz = 0.5 m (i.e., Pe_m = 1) was applied.

The left and right boundaries of the model (Figure 4.1) represent seawater and freshwater hydrostatic conditions, respectively, defined by specified-head boundary conditions. The solute boundary condition at the coastal boundary is one where inflowing water has the concentration of seawater, whereas outflowing water is assigned the ambient concentration of groundwater at the boundary. The base of the domain is a no-flow condition. The initial steady-state condition (pre-FHD) was obtained by running transient simulations for 150 y, by which time no change was observed in the salinity distribution. Instantaneous inland FHD simulations were conducted using SEAWAT's CHD package (Langevin et al., 2003), which was

assigned only to the part of the inland boundary that remained fully saturated after the FHD.

4.2.3. Dimensionless ratios in passive and active SWI

The primary controlling factors that affect transient interface behaviour in SWI problems include buoyancy forces (i.e., water density variations), advective forces (i.e., resulting from boundary head differences) and dispersion (Goswami and Clement, 2007; Werner et al., 2013a). Abarca et al. (2004; 2007) used Henry's (1964) dimensionless parameters, which we refer to as mixed-convection ratio (*MCR*) and Peclet number (*Pe*), to characterise mixed-convective (i.e., hydraulically driven versus density-driven convection) and advective-dispersive processes, respectively, in the steady-state Henry problem. *MCR* is defined as:

$$MCR = \frac{q_f}{K\delta} \tag{4.2}$$

where δ [-] is dimensionless buoyancy, calculated as $\delta = \left(\rho_s - \rho_f\right)/\rho_f$, and q_f [L/T] is the freshwater Darcy velocity ($q_f = Q_f/h_f$). Q_f [L^2/T] is freshwater flow at the inland boundary. Advective forces are more dominant relative to density (i.e., buoyancy) forces with higher values of *MCR*. Abarca et al. (2007) found that penetration of the steady-state saltwater wedge toe decreases with increasing *MCR*, which infers strengthening advective forces (acting towards the sea) relative to the buoyancy force (in the inland direction).

Both mixed-convective and advective-dispersive processes differ between passive and active transient SWI situations. For example, density forces oppose advective forces in passive SWI, whereas in active SWI, density and advective forces act in the same direction. In the context of modelling a coastal cross-section, this is invoked by freshwater outflow at the inland boundary under active SWI conditions and inflow for passive SWI conditions. It follows that the ratio of advective to buoyancy forces (i.e., *MCR*) is unlikely to be a feasible quantity for characterising the active SWI toe penetration extent, i.e., in the same manner that it is used in steady-state analyses (e.g., Abarca et al., 2007). However, other features of active SWI may respond to the balance

of advective and buoyancy forces, and therefore, *MCR* may yet provide some useful application to the characterisation of active SWI.

The steady-state definition of *Pe* is (Abarca et al., 2004):

$$Pe = \frac{D_m n + \alpha_g q_f}{Q_f} \tag{4.3}$$

where α_g [L] is the geometric mean of dispersivity, i.e., $\sqrt{\alpha_T \alpha_L}$. Dispersion is more dominant relative to advection with higher values of *Pe*. This is invoked by wider mixing zones, but also the seawater penetration (at least at the toe) is shorter, for higher *Pe* values where the saltwater wedge is at steady state (Abarca et al., 2004). Under active SWI, both buoyancy and advective forces drive seawater advance, and therefore *Pe* needs to be modified to account for the co-directional nature of buoyancy and advection. Thus, for active SWI, we apply a form of *Pe* that has an added density term in the denominator, as:

$$A_{SWI} = \frac{D_m n + \alpha_g q_f}{Q_f + K \delta h_f} \tag{3.4}$$

Given similarities between steady-state and passive SWI (e.g., Morgan et al., 2012), *MCR* and *Pe*, given by equations (4.2) and (4.3) are expected to provide insights into passive SWI, if passive SWI is considered simple transitions from one steady-state condition to another. However, whether or not the same dimensionless parameters assist in characterising active SWI is unknown. For completeness, we compare Abarca et al.'s (2004; 2007) dimensionless parameters (and equation (4.4)) to both passive and active SWI to evaluate whether these offer some indication of transient SWI behaviour. This is the first attempt to link *MCR* and *Pe* to the characteristics of transient SWI.

We adopt $|q_f|$ and $|Q_f|$ for q_f and Q_f in discussing *Pe*, A_{SWI} and *MCR* in the remainder of the article to avoid negative values of these. Obviously, where steady-conditions occur (i.e., after the cessation of passive SWI), Q_f equals Q_0. Preliminary model testing showed that in active SWI scenarios, q_f is largely stable once the abrupt hydraulic effects of the FHD have dissipated, and prior to the invasion of seawater at the inland boundary. Under these conditions, the rates of both seawater and freshwater flow (Q_s

and Q_f, respectively) towards the inland boundary are equal. We considered this period of temporary flow constancy in applying non-dimensional parameters to active SWI. That is, q_f was obtained 15 y after the inland FHD in applying the above equations to active SWI. A check after 15 y showed that the mixing zone had not reached the inland boundary in all of the SWI cases, and Q_s and Q_f were effectively the same.

4.2.4. SWI response time-scales

Previously, Watson et al. (2010) and Lu and Werner (2013) measured SWI response time-scales by considering the final steady state as the terminal condition of passive SWI events. An alternative approach is required for active SWI cases given the lack of a steady-state condition, as discussed earlier. SWI response time-scales (T_i [T]) are defined in this article as the time for the 5%, 50% and 95% relative salinity contours at the aquifer base to reach a somewhat arbitrary inland location (termed here as x_{tb} [L]), measured from the sea boundary. x_{tb} was set to 95% of the distance between the original and post-FHD steady-state interface locations from the passive SWI base case (Case 1), with the 5% relative salinity contour representing the interface location. This is somewhat comparable to the Watson et al. (2010) and Lu and Werner (2013) approaches. Figure 3.2 shows the use of x_{tb} to determine T_i for the 5% relative salinity contour in the passive and active SWI base cases. For the passive SWI base case, x_{tb} is 386 m from the sea boundary and the corresponding T_i is 50.4 y. The same value of x_{tb} subsequently defines the values of T_i in all other SWI cases by obtaining the time required for the 5%, 50% and 95% relative salinity contours to move along the aquifer base to the position x_{tb}. For example, the value of T_i for the 5% relative salinity contour in the active SWI base case is 6.6 y (see Figure 4.2).

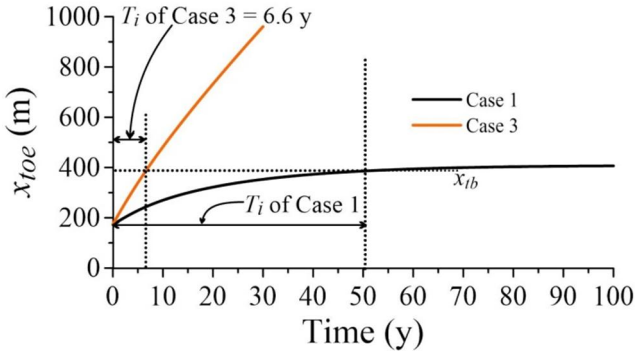

Figure 4.2. Estimation of T_i for the 5% relative salinity contour in the passive SWI (Case 1) and active SWI (Case 3) base cases.

4.3. Results and discussion

4.3.1. SWI sensitivity to parameter changes

4.3.1.1. Base cases of passive and active SWI

Figure 4.3 shows the transient interface movement of the passive and active SWI base cases. Following an instantaneous inland FHD, the interface advanced inland faster in the active SWI case relative to the passive SWI case, as expected. The mixing zone was wider under active SWI, and active SWI led to major salinization of the watertable, which was minor in the passive SWI case. Badaruddin et al. (2015) also reported these characteristics of active SWI. There was no outflow face (O_f) in both the active and passive SWI base cases, because the 5% relative salinity reached the watertable at the shoreline in the initial steady-state condition due to dispersive processes causing brackish groundwater discharge to the sea.

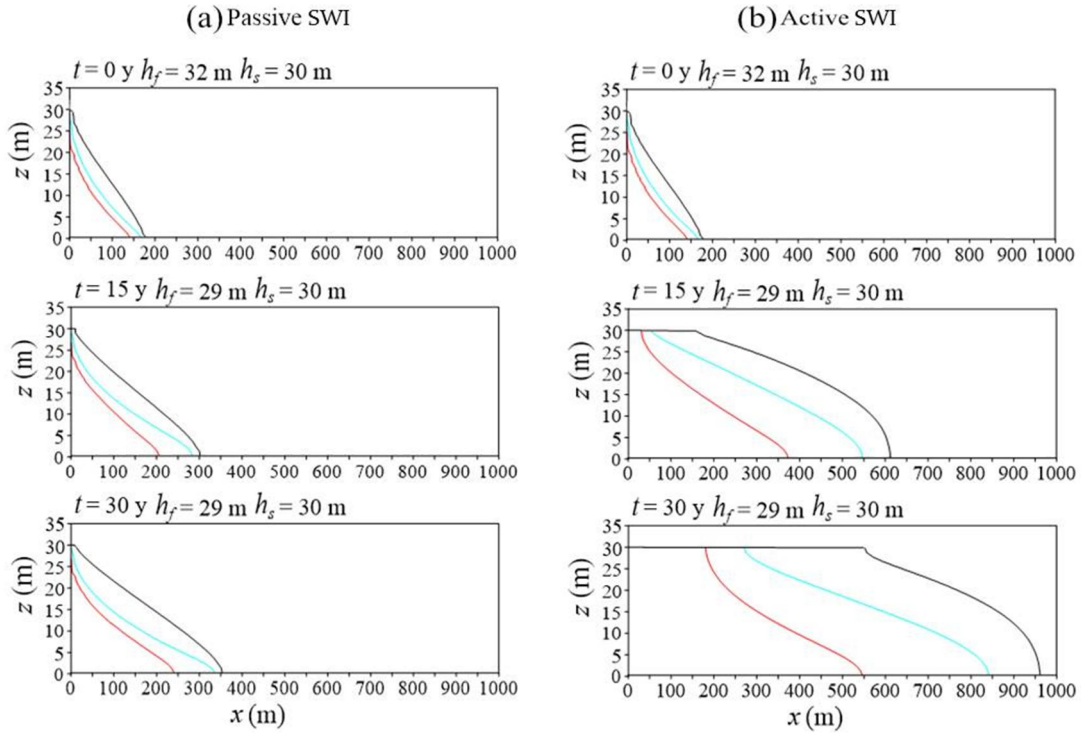

Figure 4.3. Distribution of the 5% (black line), 50% (blue line) and 95% (red line) relative salinity contours at 0 y, 15 y and 30 y for: (a) passive SWI base case (Case 1), and (b) active SWI base case (Case 3).

Figure 4.4 shows the temporal behaviour of key SWI measurables for the passive and active SWI base cases. Only the first 30 y are shown because simple continuations of trends were observed beyond that time (e.g., up to 100 y in the passive SWI base case).

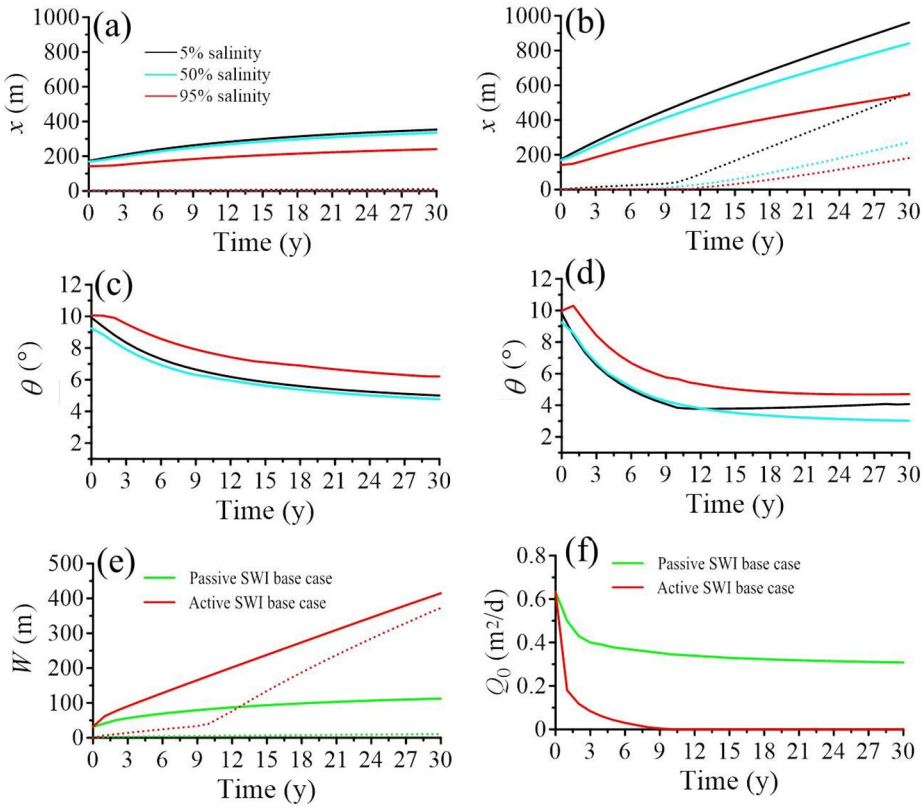

Figure 4.4. Transient changes in SWI measurables. (a) Case 1 toe and tip position, (b) Case 3 toe and tip position, (c) Case 1 interface slope, (d) Case 3 interface slope, (e) Cases 1 and 3 mixing zone widths, and (f) Cases 1 and 3 freshwater discharge to the sea. In (a), (b) and (e), solid and dotted lines are the interface toe and tip, respectively. The black, blue and red lines in (a) to (d) are the 5%, 50% and 95% relative salinities.

In the passive SWI base case, the toe (i.e., defined using three alternative salinities: 5%, 50% and 95%) moved inland gradually (Figure 4.4a), ceasing to advance after about 95 y. The tip effectively remained at the shoreline, although the 5% relative salinity contour stabilized at 18.0 m from the sea boundary (i.e., at the watertable). In contrast, the toe (e.g., in terms of the 5% relative salinity contour) almost reached the inland boundary (i.e., x = 961 m) after 30 y in the active SWI base case (Figure 4.4b). The tip (in terms of the 5% relative salinity contour) increased only slightly during the first 10 y of the active SWI case. Subsequently, the tip accelerated and maintained a higher inland velocity. Badaruddin et al. (2015) reported that this phenomenon is caused by the lag in the reduction of Q_0 to zero (and the accompanying reduction of O_f to zero), following the instantaneous FHD at the inland boundary. This is apparent in Figure 4.4f, which shows that in the active SWI base case, Q_0 dropped from the initial value of 0.63 m^2/d

to 0 m^2/d after about 10 y, which coincides with the tip's acceleration (Figure 4.4b). In the passive SWI base case, Q_0 decreased and stabilised at 0.29 m^2/d.

In Figure 4.4c, θ in the passive SWI base case decreased throughout the first 30 y of the simulation for all three relative salinity contours. This reflects the lack of inland movement in the interface tip. In the active SWI base case, more complex trends in θ are apparent (Figure 4.4d). For the 5% relative salinity contour, θ decreased for the first 10 y and then increased thereafter. This shows that the interface tip velocity exceeded the interface toe velocity for times greater than 10 y, at least in terms of the 5% relative salinity contour. For the 50% relative salinity contour, θ decreased for the entire 30 y simulation period, while θ for the 95% relative salinity contour increased only in the early period of the simulation (i.e., 1 y after FHD). This occurred because of the rapid upward movement of the 95% relative salinity contour that accompanied the closure of the outflow face at the sea boundary.

Transient changes in the interface width (Figure 4.4e) show gradual widening, approaching asymptotic values of W_{toe} and W_{tip}, in the passive SWI base case. Lu et al. (2009) attributed interface widening under passive SWI to increases in flow velocities accompanying sea-level rise or an inland FHD. Interface widths at the tip and toe increased more rapidly in the active SWI base case, relative to the passive SWI base case, with W_{toe} following an almost linear trend after the cessation of Q_0, in a similar fashion to W_{tip}.

4.3.1.2. Effects of boundary head difference on active SWI

Figure 4.5 shows transient interface behaviour during the first 30 y of three active SWI simulations, in which different advective forcings were created by imposing alternative values of $h'_{f\text{-}s}$. That is, $h'_{f\text{-}s}$ is 0 m (Δh_f = 2 m), -1 m (Δh_f = 3 m; base case) and -2 m (Δh_f = 4 m) in Cases 2, 3 and 4, respectively. For $h'_{f\text{-}s}$ of -2 m, only the results for the first 20 y are shown because the 5% relative salinity contour reached the inland boundary around that time. Figure 4.5a shows that the tip and toe moved inland monotonically for all three $h'_{f\text{-}s}$ cases, approaching linearity at later times, although no significant movement of the interface tip was observed for the smallest head drop (Case 2). The

decreasing trend in θ for the 50% relative salinity contour for all $h'_{f\text{-}s}$ variants (Figure 4.5b) indicates that the interface toe moved faster than the interface tip throughout the simulations. θ appears to tend towards asymptotic values with time that are higher (i.e., θ is steeper) for larger values of boundary head difference. That is, the landward advance of the interface tip eventually keeps pace with intrusion of the toe, and this occurs sooner with larger FHDs.

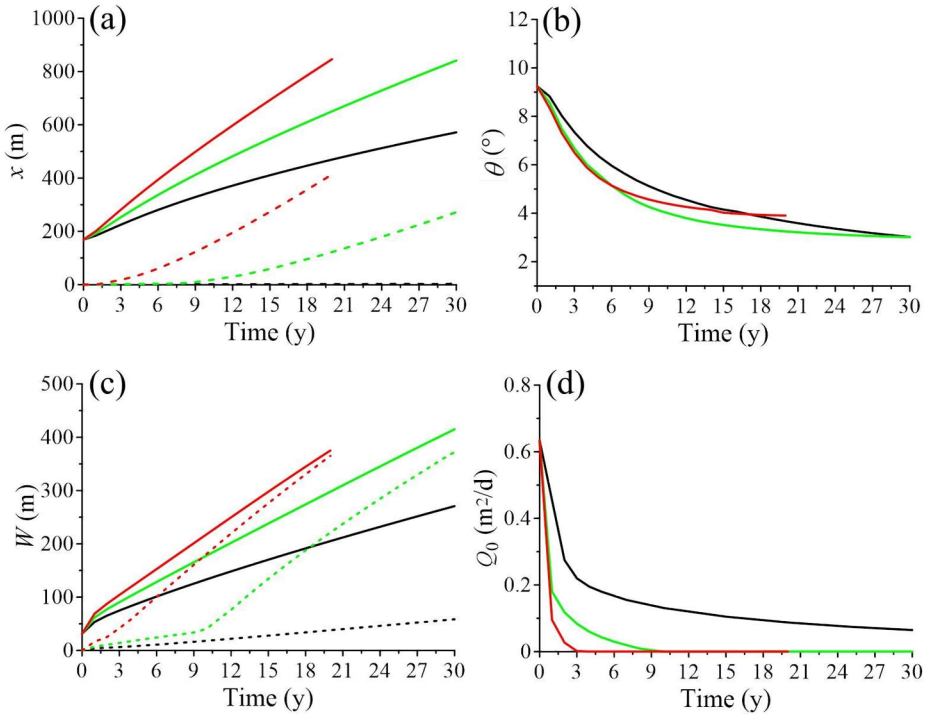

Figure 4.5. Effects of different final boundary head differences ($h'_{f\text{-}s}$ of 0 m (black; Case 2), -1 m (green; Case 3) and -2 m (red; Case 4)) on transient SWI: (a) tip and toe, (b) slope based on the 50% relative salinity contour, (c) interface width, and (d) seaward freshwater discharge. Solid and dashed lines in (a) and (c) are the interface toe and tip, respectively.

Figure 4.5c shows that larger FHDs lead to more enhanced widening of the mixing zone with time. This effect is more pronounced for W_{tip} compared to W_{toe}. That is, W_{tip} increases are subtle (at least initially) where $h'_{f\text{-}s}$ is 0 m and -1 m, whereas a steep W_{tip} trend is obtained for $h'_{f\text{-}s}$ equal to -2 m. Inflexion in the W_{tip} trends for $h'_{f\text{-}s}$ -1 and -2 m occurred at 10 and 3 y, respectively, coinciding with closure of the outflow face and the

cessation of Q_0 (Figure 4.5d). The largest FHD (Case 4) creates similar interface widening at the tip and toe.

4.3.1.3. Effects of K, n, α_L and h_s on active SWI

The effects of varying K (5, 10 and 20 m/d) and n (0.25, 0.30 and 0.35) on active SWI behaviour are presented in Figures 3.6a and 3.6b, respectively.

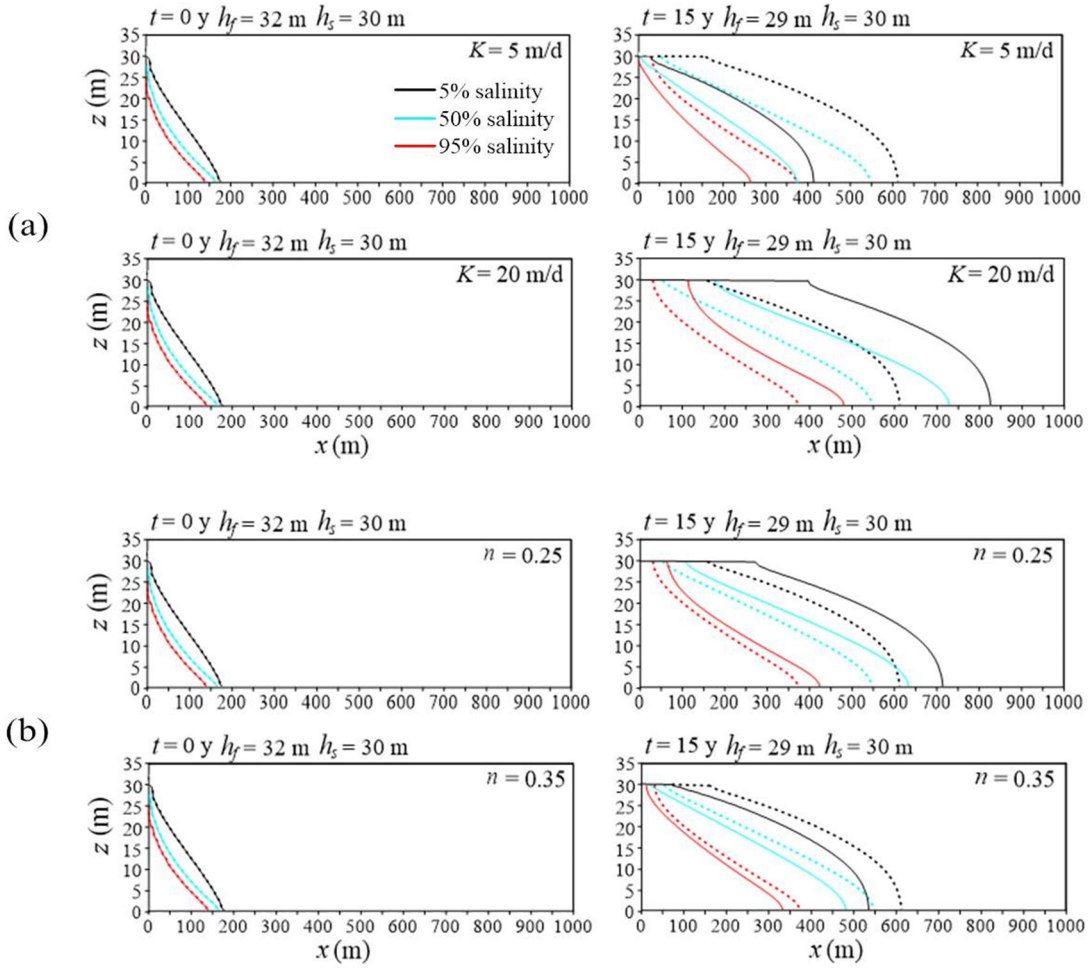

Figure 4.6. Distribution of the 5%, 50% and 95% relative salinity contours (solid lines) at 0 and 15 y using various values of: (a) hydraulic conductivity (Cases 7 and 11) and (b) porosity (Cases 39 and 43). Dashed lines represent salinity distributions of the active SWI base case.

Figure 4.6 shows that the initial steady-state salinity distribution was virtually unmodified by changes to K and/or n. This is justified based on Pe and MCR in Section

3.3.3. The interface toe and tip moved faster and the mixing zone was wider with higher K and lower n, both of which create higher flow velocities. These active SWI observations are consistent with the passive SWI results of Lu and Werner (2013). They found that the change in the interface toe position (from one steady-state condition to another) is independent of the value of K and n, but that larger values of K or lower values of n lead to shorter interface toe response time-scales (i.e., faster interface movements). Figure 4.6 also shows that both higher K and lower n produced more WTS, resulting in steeper interface angles.

Figure 4.7 illustrates the effect of modifying (i.e., relative to Case 3) α_L and aquifer thickness on active SWI. Higher α_L led to rates of interface movement that were lower at the toe but higher at the tip (thereby increasing θ), and resulted in mixing zone widths that were larger both at the toe and tip (Figure 4.7a). This is consistent with the steady-state SWI findings of Kerrou and Renard (2010), who found that stronger dispersion leads to decreased density contrasts due to the wider mixing zone. This condition causes rotation of the mixing zone alignment such that the interface toe moves seaward relative to the interface tip. Figure 4.7b shows that under transient conditions, the rates of both toe and tip movement were higher for thicker aquifers. This is in accordance with Badaruddin et al. (2015), who showed that under active SWI conditions, the toe and tip move faster inland in thicker aquifers, for a given $h'_{f\text{-}s}$. The interface slope was slightly shallower for thicker aquifers. This is attributable to the stronger buoyancy effect in deeper aquifers (e.g., the equivalent freshwater head increases with depth at the sea boundary) that drives landward rotation of the interface toe relative to the interface tip.

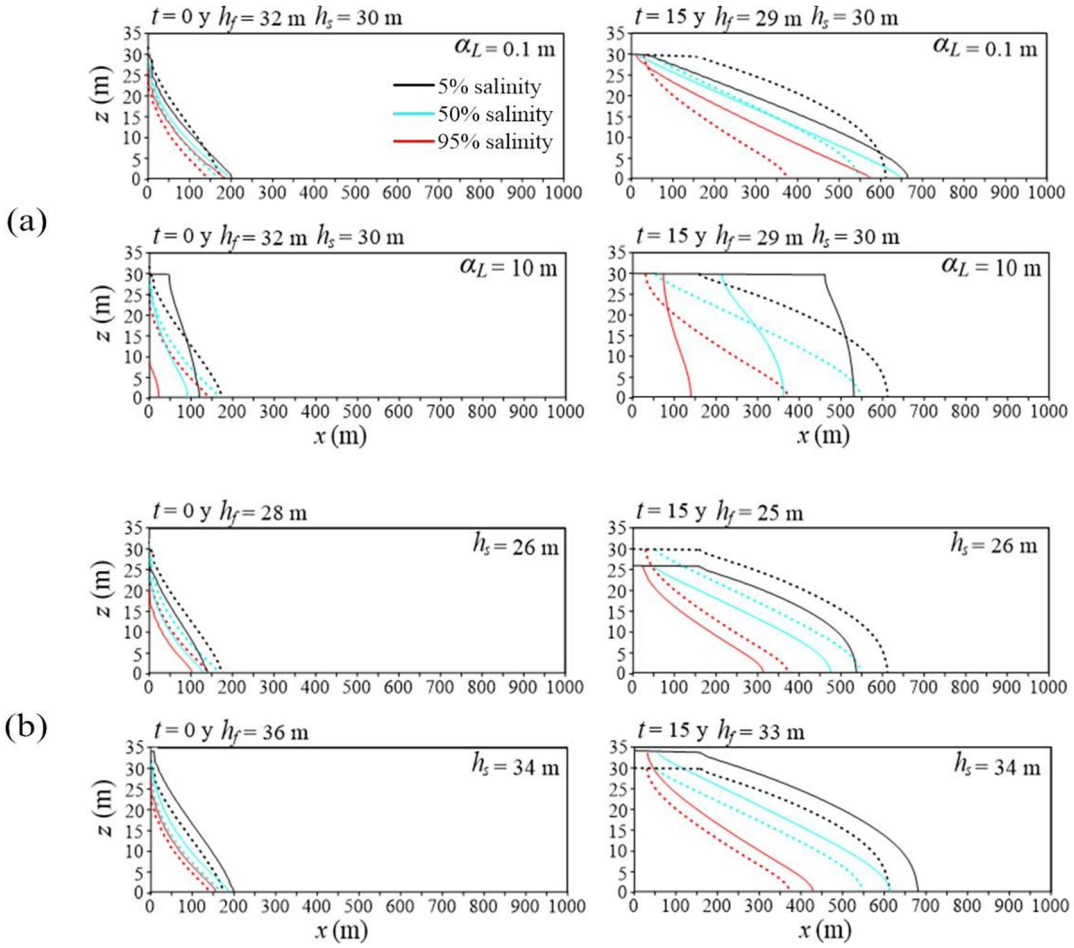

Figure 4.7. Distribution of the 5%, 50% and 95% relative salinity contours at 0 and 15 y using various values of: (a) longitudinal dispersivity (Cases 15 and 19) and (b) aquifer thickness (Cases 31 and 35). Dashed lines represent salinity distributions of the active SWI base case.

4.3.1.4. Effects of buoyancy on active SWI

The influences of modifying seawater density relative to the active SWI base case are shown in Figure 4.8. As expected, the interface toe and tip moved faster with higher ρ_s, and the stronger buoyancy force produced a shallower interface slope. Higher ρ_s also resulted in wider mixing zones. This adds to previous observations of density effects on SWI, although Schincariol (1998) noticed increased mixing with larger density contrasts in free convection problems.

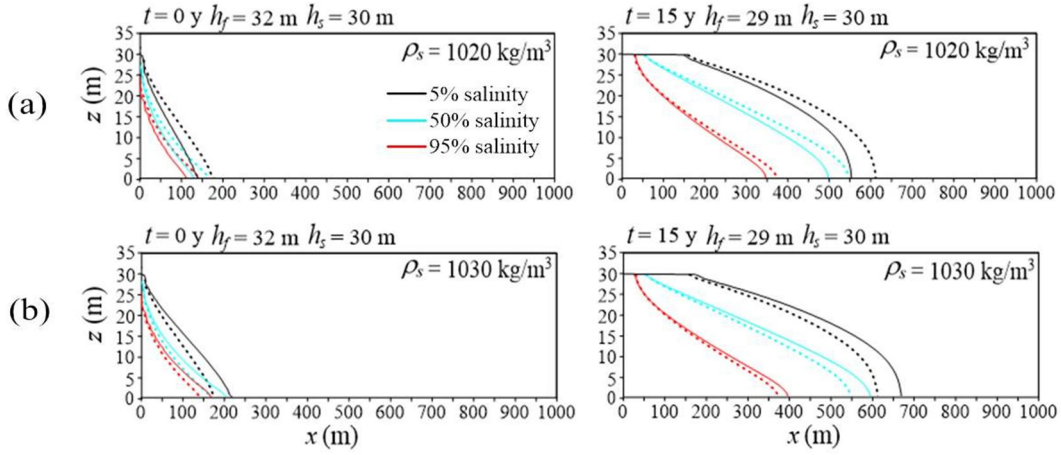

Figure 4.8. Distribution of the 5%, 50% and 95% relative salinity contours at 0 and 15 y using various values of seawater density: (a) 1020 kg/m^3 (Case 23), and (b) 1030 kg/m^3 (Case 27). Dashed lines represent salinity distributions of the active SWI base case.

Under the initial steady-state conditions illustrated in Figure 4.8, increasing ρ_s from 1020 kg/m^3 to 1030 kg/m^3 lowered q_f from 0.017 m/d to 0.015 m/d. The active SWI results showed contrasting ρ_s effects on q_f, which increased with higher ρ_s (i.e., after 15 y of active SWI, q_f was 0.013 m/d and 0.015 m/d in Cases 23 and 27, respectively). Higher ρ_s led to wider mixing zones in both steady-state and active SWI modes. That is, in Cases 23 and 27, W_{toe} was initially 21.4 and 44.5 m, respectively, and after 15 y of active SWI, these values increased to 205 and 271 m, respectively.

The evaluation of buoyancy effects was extended by comparing advective velocities $(v = q_f / n)$ to the velocities of the toe and tip at 15 years after the FHD for all non-field active SWI cases in Table 4.1. The same analysis is not possible for passive SWI cases, because there is no corresponding period of stable toe velocity. The 50% salinity contour was used to represent the toe and tip. The interface positions at 15.08 y and 15.16 y for both the toe and the tip were adopted in calculating their respective velocities. The temporal toe and tip trends were near-linear at this time (see Figure 4.5a) and hence we adopt these as representative toe and tip velocities for each case. We presume that differences between the interface velocities of active SWI and the advective transport rate (v [L/T]) are an indication of the effect of density on active

SWI. The results are presented in Figure 4.9. For clarity, only the interface velocity differences of active SWI cases with $h'_{f\text{-}s}$ of 0, -1 and -2 m are shown in Figure 4.9.

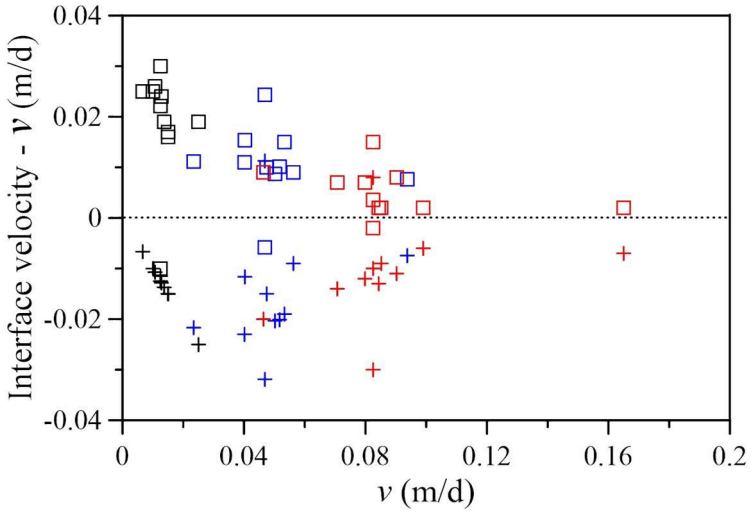

Figure 4.9. Scatter plot of the differences between the groundwater velocity (v) and the interface toe (□) and tip (+) in active SWI simulations. Black, blue and red symbols represent the cases with $h'_{f\text{-}s}$ of 0, -1 and -2 m, respectively.

Figure 4.9 shows that differences between active interface velocities and v become smaller as SWI becomes more active (i.e., as the interface velocity increases), highlighting the relatively stronger effect of advection. In general, the tip velocity is slower than v and the toe velocity is larger than v. The toe velocity is closer to v than the tip velocity, indicating that the tip velocity is more responsive to density effects. The relative effect of buoyancy on velocities is quantified using |1 – interface velocity/v|, which falls to less than 0.10 (< 10% buoyancy effect on velocities) for v > 0.08 m/d. For these cases, we argue that the rate of active SWI can be reasonably estimated using density-independent formulae.

4.3.2. Active SWI response time-scales

In this section, we compare time-scales of active SWI to those of passive SWI reported by Lu and Werner (2013), who observed a linear relationship between the response time-scale T_i and the exponential of the final boundary head differences $(e^{h'_{f-s}})$. Figure 4.10 shows T_i for 5%, 50% and 95% relative salinity contours versus $e^{h'_{f-s}}$. Several

different values of Δh_f were used (i.e., Δh_f ranging from 2 to 4 m; Cases 2 to 4 and 45 to 64) to create multiple series of T_i versus $e^{h'_{f-s}}$. The two variables were related using a simple linear relationship similar to the approach of Lu and Werner (2013), as:

$$T_i = a + be^{h'_{f-s}} \tag{4.5}$$

Here, a and b are coefficients obtained by linear regression. Their values differed depending on Δh_f. A strong correlation was observed in the linear regression between T_i and $e^{h'_{f-s}}$ values, as indicated by values of the determination coefficient R^2 [-], which ranged from 0.97 to 0.99 (the values of a, b, and R^2 resulted from a larger modelling dataset than the subset used to produce Figure 4.10 are provided in Appendix 4.A).

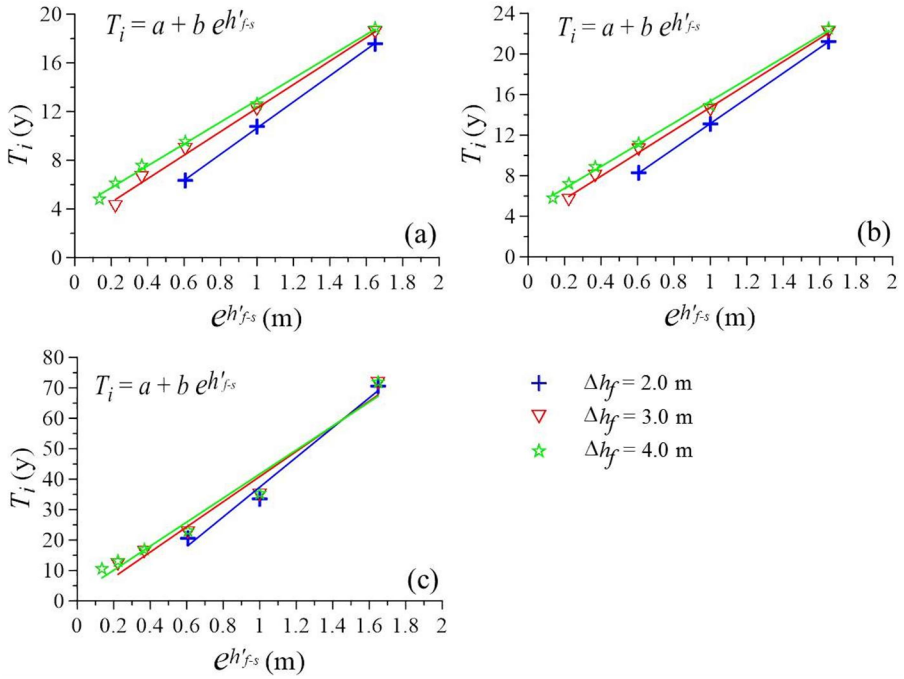

Figure 4.10. Linear regressions between $e^{h'_{f-s}}$ and T_i for: (a) the 5% relative salinity contour, (b) the 50% relative salinity contour and (c) the 95% relative salinity contour, in Cases 2 to 4 and 45 to 64.

The current analysis of time-scales differs to the approach of Lu and Werner (2013) in that the final interface location for defining T_i in the current study (i.e., x_{tb} = 386 m from the sea boundary) was the same in all cases, as discussed above. Figure 4.10 shows that for equal values of Δh_f, T_i values increased with less steep head gradients in the inland

direction (i.e., $h'_{f\text{-}s}$ becomes more positive). In other words, SWI slows down and the time-scale increases as the inland head gradient becomes shallower, as expected. This is in accordance with the passive SWI results of Lu and Werner (2013). Figure 4.10 also shows that for a given $h'_{f\text{-}s}$, T_i increases with larger Δh_f, more noticeably for the 5% and 50% relative salinities. Longer time-scales occur with larger Δh_f because the interface has further to travel, given that the initial interface is closer to the coast with increasing Δh_f. This indicates that besides the final boundary head difference, the initial boundary head difference also influences active SWI time-scales, unlike Lu and Werner's (2013) observation of passive SWI, in which only $h'_{f\text{-}s}$ modifies T_i. This outcome is at least partly attributable to the manner in which T_i has been obtained in the two studies, whereby Lu and Werner (2013) recalculated x_{tb} for each case, rather than the fixed value adopted in the current analysis, as described above. Nevertheless, the key outcome of this analysis is that active SWI time-scales are linearly related to $e^{h'_{f-s}}$, consistent with the passive SWI findings of Lu and Werner (2013), despite that our definition of T_i is unavoidably modified relative to that used by Lu and Werner (2013).

4.3.3. *MCR* and *Pe* as indicators of passive and active SWI characteristics

In this section, dimensionless parameters used by Abarca et al. (2004, 2007) are evaluated in terms of their ability to predict various characteristics of steady-state interface conditions and active SWI. Steady-state conditions were adopted as a surrogate for passive SWI in testing dimensionless parameters for reasons given in Section 3.2.3. Firstly, we reviewed the direction of sensitivities between SWI variables and model parameters, as given in Table 4.2. The complete results of SWI variables for the passive and active SWI cases listed in Table 4.1 are provided in Appendix 4.B and 4.C, respectively.

Table 4.2. Trends in SWI variables as a function of increases in the values of model parameters, arising from the sensitivity analysis.

SWI variable	Model parameters					
	K	α_L	ρ_s	h_s	n	$\lvert h'_{f\text{-}s} \rvert$
Passive SWI						
x_{toe} (50% contour)	None	Falling	Rising	Rising	None	Falling
W_{toe}	None	Rising	Rising	Rising	None	Falling
θ (50% contour)	None	Rising	Falling	Falling	None	Rising
Active SWI						
x_{toe} (50% contour)	Rising	Falling	Rising	Rising	Falling	Rising
x_{tip} (50% contour)	Rising	Rising	Rising*	Rising	Falling	Rising
W_{toe}	Rising	Rising	Rising	Rising	Falling	Rising
W_{tip}	Rising	Rising	Rising	Rising	Falling	Rising
θ (50% contour)	Falling*	Rising	Falling	Falling*	Rising*	Mixed

"None" means that the SWI variable is insensitive to the parameter
"Rising" means that the SWI variable increases with an increase in parameter value
"Falling" means that the SWI variable decreases with an increase in parameter value
"Mixed" means that there is no predominant trend.
"*" refers to variables where a predominant trend is noted, but exceptions apply.

Table 4.2 highlights complex relationships between SWI variables and model parameters. For example, under steady-state conditions, x_{toe} (50% contour), W_{toe} and θ (50% contour) each respond differently (in terms of rising, falling or insensitive) to changes in individual parameters. Under transient (i.e., active SWI) conditions, x_{tip} (50% contour), W_{toe} and W_{tip} respond in the same general fashion, but differently to θ (50% contour) and x_{toe} (50% contour). None of the SWI variables responds to parameter changes in the same manner (i.e. show the same trends) under both passive and active SWI conditions.

Some of the SWI responses are predictable using *Pe* and *MCR*. For example, the initial steady-state salinity distribution of the base case model was virtually unmodified by changes to K and/or n (see Section 3.3.1.3). These insensitivities are recorded in Table 4.2 as "None", and can be justified by considering *Pe* and *MCR* for steady-state conditions. That is, *Pe* is dominated by α_g/h_f given that D_m is small, and therefore *Pe* is largely independent of both K and n (see equation (4.3)). In equation (4.2), q_f/K is approximately proportional to $h'_{f\text{-}s}$ under steady-state conditions due to the specified-

head boundaries, and therefore *MCR* is also essentially independent of K and n. However, both K and n play an important role in active SWI, as illustrated in Figure 4.6 and identified in Table 4.2. This highlights important differences between the controlling factors of active and steady-state SWI.

Drawing on equations (4.2) to (4.4), some of the responses in SWI variables to parameter changes can be linked to dimensionless parameters. For example, steady-state x_{toe} (50% salinity contour) increases with lower α_L and $h'_{f\text{-}s}$, and with higher ρ_s and h_f. The effects of ρ_s and $h'_{f\text{-}s}$ are captured within the definition of *MCR* (equation (4.2)), whereas the effects of α_L and h_f are contained within *Pe* and A_{SWI} (equations (4.3) and (4.4)). Linear correlation between steady-state x_{toe} (50% salinity contour) and *MCR* results in a falling trend and $R^2 = 0.77$, indicating the dominant influences of ρ_s and $h'_{f\text{-}s}$ in controlling steady-state x_{toe}. Efforts to correlate steady-state x_{toe} with *Pe* were unsuccessful ($R^2 < 0.14$), and therefore α_L and h_f are minor factors relative to ρ_s and $h'_{f\text{-}s}$ in controlling x_{toe} for the steady-state cases considered here.

MCR showed similar correlation statistics when linearly related to the transient x_{toe} and x_{tip} positions, producing R^2 values of 0.61 and 0.71, respectively. While steady-state x_{toe} generally reduces with increasing *MCR*, transient x_{toe} and x_{tip} tend to be larger with higher *MCR*. It is important to note that relatively few unique values of δ have been tested in obtaining these relationships (see Table 4.1). Thus, the active SWI results reflect x_{toe} and x_{tip} that are further inland with stronger discharge (q_f; away from the coast), rather than mixed convection processes. Hence, we maintain that *MCR* is a poor indicator of active SWI trends, in terms of the effects of mixed-convective processes on x_{toe} and x_{tip}. However, *MCR* has a more logical association with the interface slope, given Kerrou and Renard's (2010) observations, as mentioned earlier, and indeed, *MCR* shows some correlation with steady-state θ (50% contour), with $R^2 = 0.65$. No significant correlation was apparent between *MCR* and active SWI θ (50% contour). Rather, both steady-state and active SWI θ (50% contour) show some correlation to A_{SWI}, with R^2 values of 0.61 and 0.80, respectively. A weaker correlation between *Pe* and steady-state and active SWI θ was obtained (R^2 equal to 0.30 and 0.49, respectively). These results highlight the complex mixed convective and convective-dispersive relationships that govern interface slope under transient SWI conditions.

Surprisingly, *Pe* was found to be a poor indicator of steady-state W_{toe}, with R^2 of 0.11. In fact, *MCR* outperformed *Pe* in terms of its linear correlation with steady-state W_{toe}, producing $R^2 = 0.67$. This is in contradiction to the findings of Abarca et al. (2004). In active SWI cases, *Pe* was similarly a poor predictor ($R^2 < 0.26$) of W_{toe} and W_{tip}. A_{SWI} also produced a weak match to active SWI W_{toe} and W_{tip} (R^2 of 0.42 and 0.44, respectively), albeit slightly improved relative to *Pe*.

No correlation was found between *Pe* and steady-state x_{toe} or active SWI x_{toe} and x_{tip} ($R^2 < 0.12$), despite Abarca et al. (2004) suggesting smaller toe penetration with higher *Pe*. A_{SWI} was similarly poorly performing as a measure of interface location in active SWI cases ($R^2 < 0.30$), although R^2 for A_{SWI} versus steady-state x_{toe} was 0.56 using a power function.

The results suggest that the dimensionless forms of *Pe* and *MCR* used in the current study cannot be used to generalise without exception the sensitivity and response of the freshwater-saltwater interface to changes in various aquifer parameters. Nonetheless, the dimensionless numbers remain useful indicators of buoyancy, advective and dispersive controls, which influence the interface behaviour in predictable ways under certain conditions, as described above. Despite the inability of the dimensionless numbers tested here to consistently predict interface changes arising within the one-at-a-time sensitivity analysis carried out in this study, both under steady-state and active SWI conditions, we have been unable to define new dimensionless variables with improved performance in characterising active SWI.

4.3.4. Field-scale example of SWI

As stated previously, Case 65 represents the field SWI case in the Pioneer Valley aquifer, Australia (Werner and Gallagher, 2006). The relevant parameters are listed in Table 4.1, and the transient interface behaviour for this case is presented in Figure 4.11, which shows aggressive inland movement of the interface toe and tip, following the inland FHD. At the initial steady-state, the values of *Pe* and *MCR* in this case are 0.07602 and 0.02978, respectively. At 15 y after FHD, the values of *Pe* and *MCR*

changed to 0.08736 and 0.03691, respectively. Relative to the non-field active SWI cases with α_L equal to 10 m (i.e., Cases 18, 19 and 20), the magnitudes of dimensionless numbers for Case 65 are closer to those of Case 19 (i.e., Pe = 0.1091; MCR = 0.05626). Cases 65 and 19 are characterised by $h'_{f\text{-}s}$ of -0.8 m and -1 m, respectively. Interestingly, it was observed that at 15 y after FHD, the magnitudes of W_{toe} and W_{tip} for Case 65 are approximately five times larger than those in Case 19 (see Appendix 4.C). This is likely due to the higher K (166 m/d) and lower n (0.1) values used in Case 65 which increase the flow velocity in this case (q_f = 0.15 m/d), relative to Case 19 (q_f = 0.014 m/d).

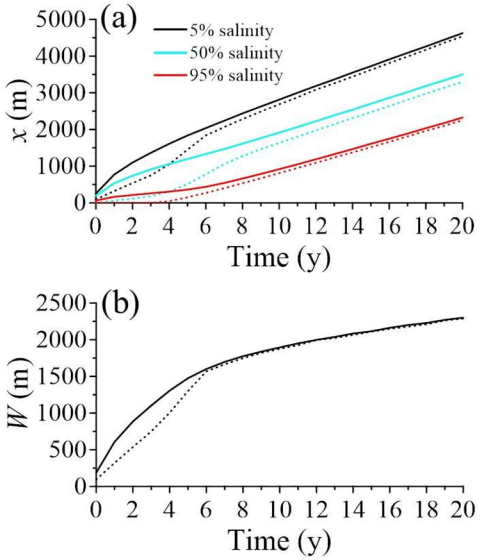

Figure 4.11. Transient changes of: (a) interface locations and (b) interface width, for Case 65. Solid and dotted lines represent the interface toe and tip, respectively.

To examine the effects of aquifer parameters on the interface position and width in the field-scale case, sensitivity analyses were conducted with increasing K (332 m/d), α_L (20 m), ρ_s (1030 kg/m^3), h_s (40 m) and n (0.2), using Case 65 as the base case (the results are not shown for brevity). It was observed that for a given $h'_{f\text{-}s}$, the x_{toe} increased with increasing K, ρ_s and h_s and decreased with increasing α_L and n. In addition, the x_{tip} and the mixing zone width (at the toe and tip) increased with increasing K, ρ_s, h_s and α_L and decreased with increasing n. These trends are consistent with those found for the cases adopting smaller domain sizes (Table 4.2).

To explore the relationship between SWI response time-scales and the inland FHD in the field-scale case, more SWI simulations were undertaken using five different values of $h'_{f\text{-}s}$ (from -0.4 to -2 m, in increments of -0.4 m), using Case 65 as the base case. Five values of Δh_f were adopted for each $h'_{f\text{-}s}$ value (i.e., 5.4, 5.8, 6.2, 6.6 and 7 m), resulting in 25 more SWI simulations. The arbitrary point of x_{tb} used for the field-scale cases was 1133 m (obtained from the 95% of the distance between the original and post-FHD steady-state interface locations of the 5% relative salinity in the passive SWI field case with $h'_{f\text{-}s}$ = 1 m) from the sea boundary. It was observed that the final and the initial boundary head differences influence the SWI time-scales in the field-scale cases (Figure 4.12). The SWI response time-scales are also linearly related to $e^{h'_{f-s}}$, as indicated by high values of R^2 that ranged from 0.98 to 0.99 (the values of a, b and R^2 resulted from a larger modelling dataset than that given in Figure 4.12 and are provided in Appendix 4.D). These results are in accordance with the results of the non-field cases.

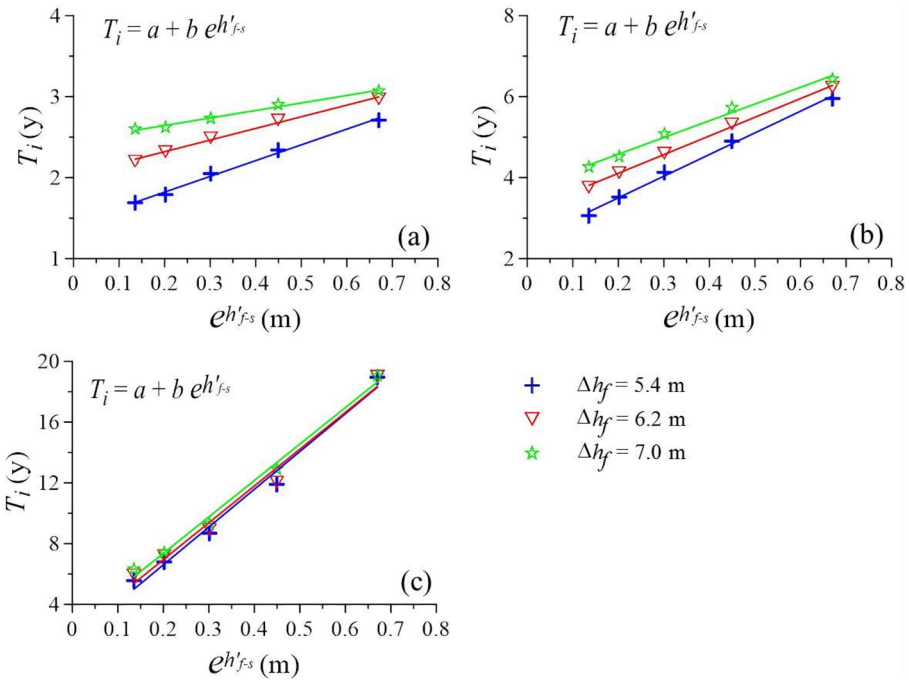

Figure 4.12. Linear regressions between $e^{h'_{f-s}}$ and T_i for: (a) the 5% relative salinity contour, (b) the 50% relative salinity contour, and (c) the 95% relative salinity contour, in the field scale cases.

4.4. Conclusions

The current study is the first attempt to characterize freshwater-saltwater interface characteristics during active SWI conditions. Aside from conforming to several of the active SWI observations of Badaruddin et al. (2015), our sensitive analysis reveals important features of active SWI. For example, while the interface slope gradually became shallower during passive SWI, trends in the interface angle during active SWI simulations were complex. That is, active SWI can sometimes lead to interface tip movements that are faster than the interface toe velocity. The interface tip eventually kept pace with the toe, particularly for increasingly active SWI, which also led to widening of the mixing zone with time, especially at the interface tip. Furthermore, the interface toe and tip moved faster and the mixing zone was wider with higher K and lower n, both of which created higher flow velocities. These observations of active SWI match those by Lu and Werner (2013) for passive SWI. However, only in active SWI does higher K and lower n produce more watertable salinization, resulting in steeper interface angles. In addition, higher α_L led to rates of interface movement that were lower at the toe but higher at the tip (thereby increasing interface alignment), and resulted in mixing zone widths that were larger both at the toe and tip. This result overlaps with observations of steady-state SWI characteristics by Kerrou and Renard (2010). The interface slope was slightly shallower for thicker aquifers due to stronger buoyancy effects in deeper aquifers.

As expected, the interface toe and tip moved faster with higher seawater density, and the stronger buoyancy force produced a shallower interface slope. Higher seawater density also resulted in wider mixing zones. This adds to previous observations of density effects on SWI. Differences between interface velocities under active SWI and the advective transport rates were used as an indication of the effect of density on active SWI. The effect of advection was found to increase as SWI became more active. The toe velocity was closer to the advective transport rate than the tip velocity, indicating that the tip velocity was more responsive to density effects. It was found that the rate of active SWI could be reasonably estimated using density-independent formulae when the advective transport rate was greater than 0.08 m/d.

Based on the numerical modelling results, we conclude that active SWI time-scales are linearly related to $e^{h'_{f-s}}$, consistent with the passive SWI findings of Lu and Werner (2013), despite that our definition of T_i was unavoidably modified relative to that used by Lu and Werner (2013). A field-scale SWI example showed that the effects of aquifer parameters on interface behaviour and the time-scales showed consistent trends to the 1 km-scale models.

The transient nature of our active SWI investigation adds to the primarily steady-state assessment in a concurrent analysis by Werner (2017). For example, the link between mixing zone width and the freshwater-seawater density difference highlight critical differences between active SWI and slower rates of SWI. As a general concept, coastal aquifer custodians should consider SWI to resemble density-independent plumes as the disequilibrium between the coastal head and inland heads increases. It follows that under increasingly active SWI conditions, salinization is more likely to eliminate the freshwater normally found in the shallow part of the aquifer. The current results, combined with Werner's (2017) modelling show that this effect is particularly dependent on density and dispersive parameters, and the degree of disequilibrium.

Our attempts to describe active SWI in terms of dimensionless parameters, which are widely used for steady-state SWI, were unsuccessful. Specifically, the results demonstrate that the dimensionless parameters of *Pe* and *MCR* were unable to consistently predict interface changes arising within the sensitivity analysis, both under steady-state and active SWI conditions. Complex relationships were found to occur between SWI variables and model parameters, whereby none of the SWI variables show the same type of response (i.e., rising, falling, etc.) to parameter changes under both passive and active SWI conditions. This highlights important differences between the controlling factors of active and steady-state SWI. Further work is needed to define new dimensionless variables with improved performance in characterising active SWI.

5. CONTRIBUTION OF SEAWATER INTRUSION TO AQUIFER DEPLETION: ULEY SOUTH BASIN (SOUTH AUSTRALIA)

5.1. Introduction

Seawater intrusion (SWI) is a phenomenon where seawater intrudes into coastal aquifers and leads to losses in the available fresh groundwater (Bear, 1979). This phenomenon has become a major problem in many coastal aquifers around the world (Werner et al., 2012; 2013). The occurrence of SWI is usually human-induced, mainly through groundwater exploitation (Ferguson and Gleeson, 2012), although natural factors such as sea-level rise and climate variations may also contribute to SWI (Werner and Simmons, 2009; Koussis et al., 2012).

Understanding the relationship between climate variations (e.g., leading to recharge variability), pumping stresses and the extent of SWI is critical for developing effective strategies for avoiding SWI and managing coastal aquifers more generally. For instance, knowledge of the relative importance of the key causal factors of SWI will inform attempts to optimize freshwater availability and constrain groundwater extraction (Cheng et al., 2000; Mantoglou, 2003; Werner et al., 2011). Previous studies of regional-scale SWI have mainly focused on groundwater salinity responses to the cumulative effects of aquifer stresses, and rarely isolate or compare their individual effects on SWI. For example, three-dimensional (3D) numerical models of SWI have been developed for Eastern Cap-Bon (Tunisia; Paniconi et al., 2001), Pioneer Valley (Australia; Werner and Gallagher, 2006), Salalah Plain (Oman; Shammas and Jack, 2007), and Uley South Basin (Australia; Werner and Dang, 2013). Each of these assessed variations in both climate and pumping during historical periods, although the individual effects of pumping and climate variations were not distinguished. Regional-scale SWI models have also been developed for the Alabama Gulf Coast (USA; Lin et al., 2009), Damsharko (Syria; Allow, 2011) and Goksu Deltaic Plain (Turkey; Cobaner et al., 2012). However, these models consider only the impact of historical groundwater pumping variations on SWI, and adopted time-invariant recharge. No regional SWI

studies available to date have attempted to differentiate the effects of climate and groundwater pumping variations on SWI. As a result, comparing the individual impact of climate and pumping variability on SWI using regional SWI modelling remains a challenge.

The USB coastal aquifer was chosen as the subject of the current study. The USB contributes around 70% of the total water supply for some 55,000 residents of the Eyre Peninsula, South Australia (Zulfic et al., 2007), providing around 5 GL/year in recent years (Knowling et al., 2015). The USB is in direct contact with the ocean, and natural and anthropogenic stresses make the aquifer susceptible to SWI (Ward et al., 2009; Werner et al., 2011). Understanding the relative contributions of natural and anthropogenic stresses to the extent of SWI in USB has become imperative on the back of a recent parliamentary inquiry (NRC, 2013) into water management in the Eyre Peninsula. This investigation concluded that the cause of water quantity and quality decline in the Uley Basins (of which Uley South is a part) cannot be clearly attributed to either natural (i.e., recharge variability) or anthropogenic (i.e., groundwater pumping) factors. Furthermore, it is presently unknown as to the degree to which SWI is a component of the freshwater depletion in the region.

Knowling et al. (2015) used all available hydrogeologic and groundwater pumping data for the period 1960-2012 to develop a calibration-constrained regional groundwater model of USB. They set out to quantify the individual contributions of climate and pumping on the decline in USB groundwater levels. To increase the reliability of their model predictions, Knowling et al. (2105) used PEST (Doherty, 2013) to estimate model parameters on the basis of steady-state and transient groundwater conditions using a parameter estimation processes that was parallelised using BeoPEST (Hunt et al., 2010). Pilot point parameterization (de Marsily et al., 1984) was used to reflect spatial variability in both hydraulic conductivity and storage parameters. Knowling et al. (2015) found that the effects of climate and pumping stresses on groundwater head decline were varied across the aquifer and changed with time. They also found that the pumping impacts on the groundwater head decline were greater than those of climate between 1978 and 2012 (i.e., groundwater pumping contribution was shown to be 1.4 times that of climate in terms of the maximum basin-scale water budget). Nevertheless,

since the study of Knowling et al. (2015) focused on groundwater heads conditions only in the USB, then the individual effect of climate and groundwater pumping on SWI was neglected in their study.

Given that SWI introduces more dense water into coastal aquifer, SWI may affect the fresh groundwater head response to aquifer stresses around the coast, thereby modifying the behaviour predicted in single-density groundwater models, such as those used by Knowling et al. (2015). The addition of seawater to models of USB is expected to induce seawater recirculation near the coast due to the introduction of buoyancy-driven forces (Smith, 2004; Chang and Clement, 2013). No previous regional and small-scale SWI studies available to date have explored the seawater effects on the fresh groundwater head behaviour near the coast. Morgan et al. (2012) have shown through steady-state sharp-interface analytic modelling that the change of seawater volume caused by SWI can significantly influence the groundwater level trends in coastal aquifers, however they did not explore in detail to what extent the buoyancy effects of seawater can change the fresh groundwater head responses to human and climate stresses, above the interface around the coast. This is important to be examined because groundwater heads are commonly used as an indicator in controlling groundwater extraction in coastal aquifers (Evans et al., 2004; Bekesi et al., 2009; Werner et al., 2011).

The present study aims to extend the study of Knowling et al. (2015) to examine the individual relative contributions of climate variability (recharge) and human stresses (pumping) on the extent of SWI in USB. In the current study, the complex pattern of SWI is involving the temporal and spatial variability conditions of aquifer stresses. This study also purposes to investigate the effects of seawater (buoyancy) on the fresh groundwater head behaviour, in responding to aquifer stresses in the vicinity of the coast in USB coastal aquifer.

5.2. Preliminary analysis of buoyancy effects on groundwater head behaviour

To initially check whether groundwater head behaviour can be affected by SWI, using SEAWAT version 4 (Langevin et al., 2008), four pre-numerical simulations (i.e., a

density-dependent model without pumping, a density-dependent model with pumping, a freshwater only model without pumping and a freshwater only model with pumping) using a small scale two-dimension (2D) of unconfined aquifer were conducted in the current study. Since the pre-numerical simulation was run in 2D, then, the 3D radial flow effects of pumping on groundwater heads were neglected in these simulations. The size of the 2D model is 1.17 m in length, 0.05 m in width and 0.45 m in height (Figure 5.1a), the same length and width used by Mehdizadeh et al. (2014) and Badaruddin et al. (2015). Following Badaruddin et al. (2015), a uniform grid size of Δx = 0.50 cm and Δz = 0.50 cm was used, resulting in a grid of 21,060 cells. The aquifer was considered homogeneous and isotropic, hydraulic conductivity (K [L/T]) is 269 m/d and effective porosity (n [-]) is 0.41 (Badaruddin et al., 2015). The longitudinal dispersivity (α_L [L]) is 0.004 m and the transverse dispersivity (α_T [L]) is one tenth of α_L (Lu and Werner, 2013; Abarca et al., 2007). The values of saltwater density (ρ_s [M/L^3]) and freshwater density (ρ_f [M/L^3]) are 1025 kg/m^3 and 1000 kg/m^3, respectively and molecular diffusion (D_m [L^2/T]) is 8.64 × 10^{-5} m^2/d. The specified inland head (h_f [L]) and sea level (h_s [L]) in the model were set to 0.38 m and 0.37 m, respectively. The magnitude of pumping was set to be 0.0005 m^3/hour, and the distances of the pumping location from the inland boundary (x_p [L]) and from the bottom of the model (y_p [L]) were 0.16 m and 0.19 m, respectively.

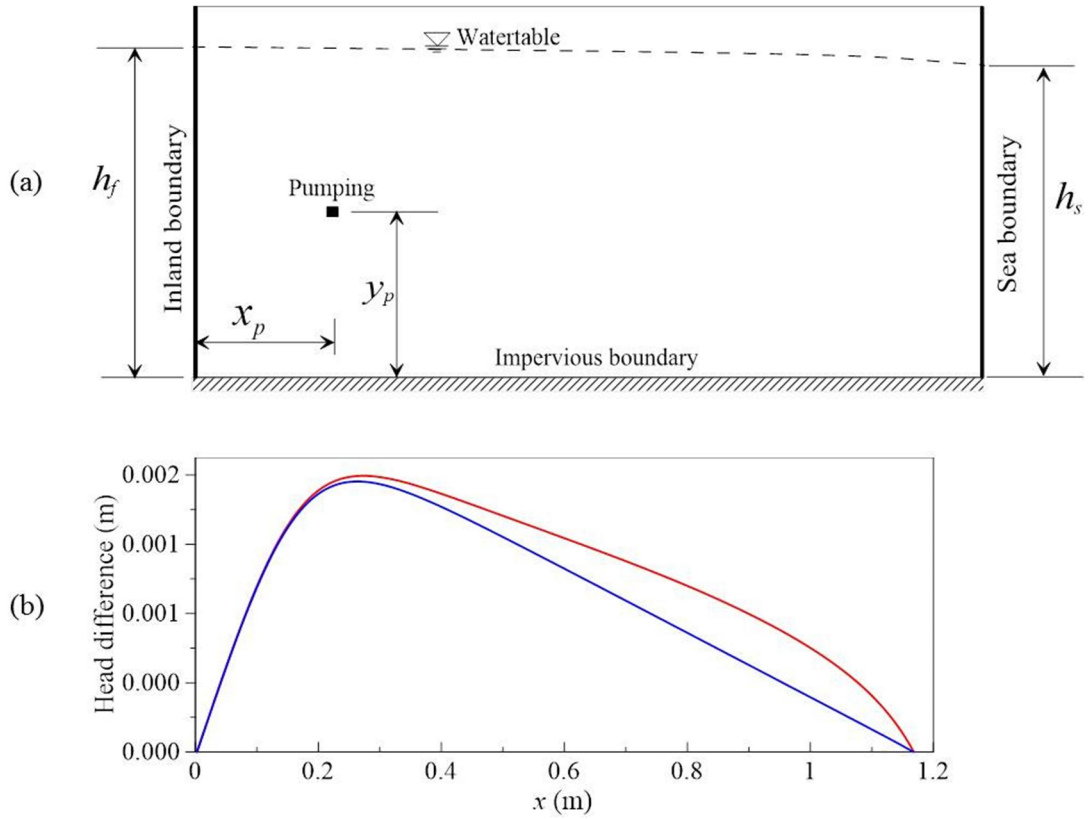

Figure 5.1. (a) Schematic picture of the small-scale 2D model (b) the head differences resulted from the pumping effects in the density-dependent (red line) and fresh water only (blue line) models along the 2D model at 0.36 m from the bottom (above saline water).

The comparison of fresh groundwater head differences resulted from the pumping effects along the 2D model (i.e., 0.36 m from the bottom) in the density-dependent and freshwater only models under steady-state conditions (i.e., after 34 hours of simulation time) is presented in Figure 5.1b. It was observed that in general, the relative effects of pumping stress on the fresh groundwater head differences near the sea boundary were slightly higher by 0.02 cm on average when seawater involved in the model compared to those in the freshwater model only. This phenomenon is investigated further in the current study to see how this occurs in the real world scale settings.

5.3. Description of study area

USB is situated in the southern part of the Eyre Peninsula, South Australia (Figure 5.2). Its Mediterranean-type climate is characterised by precipitation at winter (May to

October) and hot and dry at summer (November to April) (Harrington et al., 2006). The averages of annual pan evaporation and precipitation rates from 1975 to 2010 are 1547 and 560 mm/y, respectively (Bureau of Meteorology, 2010).

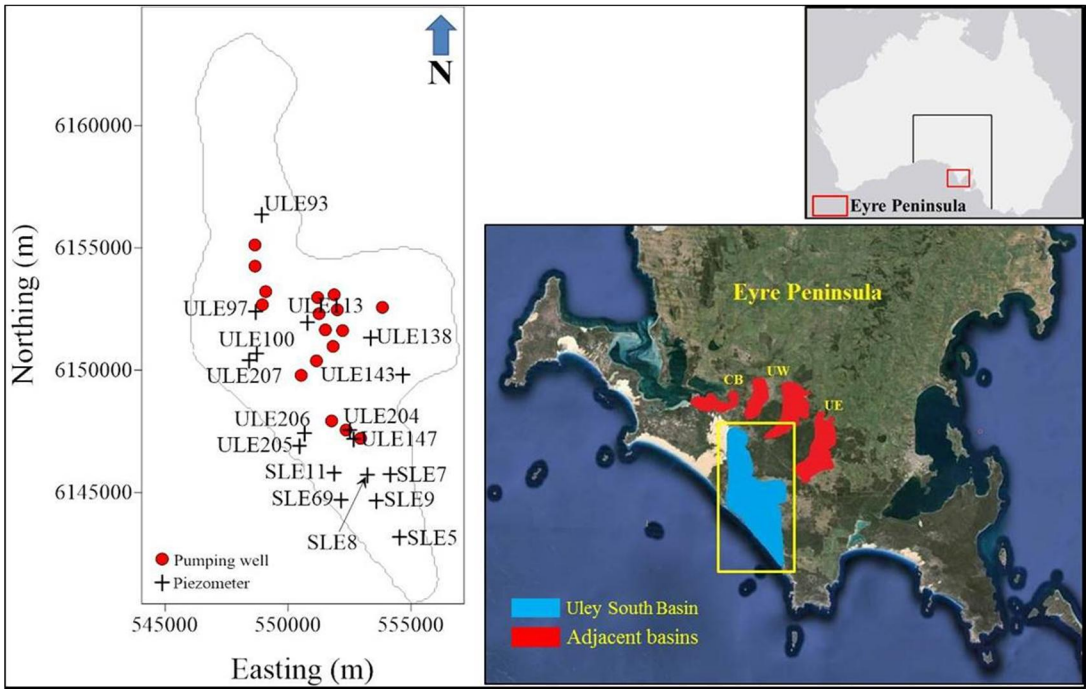

Figure 5.2. Locality map of study area and bore locations. UE, UW and CB are the adjacent groundwater basins Uley East, Uley Wanilla and Coffin Bay, respectively.

USB is topographically closed and surrounded by steep coastal cliffs of up to 140 m AHD (Australian Height Datum; approximately mean sea level) to the south and by low-reliefs between 50 and 170 m AHD to the west, north and east of the basin (Clarke et al., 2003; Werner, 2010). The land surface is formed mainly by thin calcareous, sandy soils, and clayey loams (Evans, 1997; Alcoe, 2009). The USB is covered mainly by three kinds of vegetation i.e., Malle Scrub and Drooping She-oak (Li, 2008), and Sparse Grassland (Ordens et al., 2012). There are numerous sinkholes in USB and these sinkholes perform as a mechanism for rapid groundwater recharge (Ordens et al., 2012). Using one-dimensional and field-based approach, Ordens et al. (2012) found that the temporal and spatial recharge averaged value in the area was around 84 mm/y. Estimation of the temporal and spatial recharge volume distribution in USB over the period 1960 – 2012 (Ordens et al., 2012; Knowling et al., 2015) is provided in Figure 5.3a.

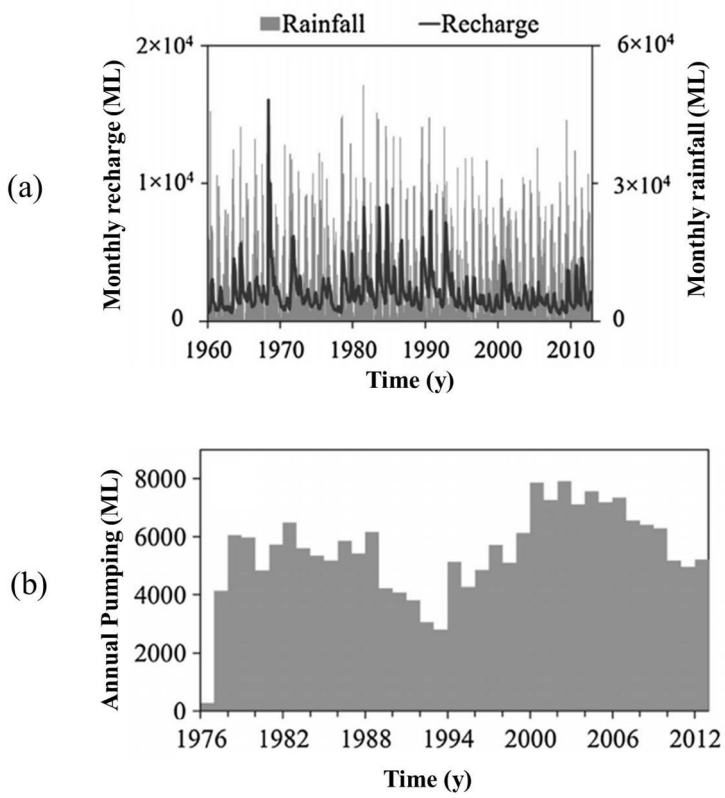

Figure 5.3. Time series of USB total: (a) annual pumping volume and (b) monthly recharge and rainfall volume distribution (Knowling et al., 2015).

The USB consists of two main aquifers: the Quaternary Limestone (QL) (Bridgewater Formation) and the Tertiary Sand (TS) (Wanilla Formation), and these aquifers are separated by a discontinuous Tertiary Clay aquitard (TC) (Harrington et al., 2006). The QL is formed mainly by aeolian sediments and limestone while the TS consists primarily of sands, clay and gravels (Harrington, 2006). The TC is formed mostly by clay and silty clay, and is highly variable in its thickness such that the QL and TS are hydraulically connected in several locations (Morton and Steel, 1968). Similar to Werner and Dang (2013) and Knowling et al. (2015), in the current study, USB coastal aquifer is treated as an equivalent porous media and its karst behaviour is ignored. This is because the majority of groundwater flow in USB occurs through granular porosity, with fewer well-developed karst conduits within the saturated zone (Sibenaler, 1976; Barnett, 1978; Davis et al., 2013; Werner, 2014). Groundwater extraction in the USB was started in 1976 with eight production wells (Barnett, 1978) and the extraction occurs only from the QL aquifer (Clarke et al., 2003, Werner et al., 2010). The pumping from QL is used primarily for urban water supply (Ordens et al., 2012). In year 2000,

the number of production wells increased to 17 and these wells were operated only by the South Australian Water (SA Water) (Werner et al., 2010). The data for the total annual pumping volume in USB from 1976 to 2012 can be seen in Figure 5.3b.

5.4. Methodology

5.4.1. Modelling strategy

Prior to the development of SWI model, a groundwater flow (GWF) model of USB with two layers (QL and TS layers) was developed by Knowling et al. (2015) using MODFLOW (Harbaugh et al., 2000). A Newtonian solver (PCGN; Naff and Banta, 2008), which is capable for solving problems involving drying and rewetting in the unconfined coastal aquifer conditions, was used in their study. The TC layer was represented implicitly in their model using a quasi 3D approach (i.e., vertical flow only and no TC storage effect) (Chiang and Kinzelbach, 1998). In the current study, the previous GWF model was subsequently converted to GWF with 10 layers using MODFLOW and the TC layer was made to be explicitly represented in the model. In converting the 2-layer GWF model to 10-layer GWF model, comparisons were made between the new and previous models in terms of flow and head components to ensure consistency.

In this study, a 10-layer 3D SWI model was created using SEAWAT version 4. SEAWAT is a widely used code and has been validated using several benchmark problems (e.g., Langevin et al., 2003; Brovelli et al., 2007; Goswami and Clement, 2007). The governing equations of SEAWAT from the user manual are not re-written here for brevity. Since the Newtonian solver is not yet compatible with SEAWAT version 4, then PCG2 solver (Harbaugh et al., 2000) was chosen in the SEAWAT simulations. To overcome the non-convergence problem faced in the SEAWAT model due to the dry cells issues and to produce the same results in terms of groundwater heads as obtained in the GWF model, the type of QL layer in the SWI model was made to be confined and then the groundwater heads resulted from the GWF model were imported as the initial head conditions in the SWI model. The top of Layer 1 in QL layer was also changed based on the Layer 1's heads obtained from the GWF model

and all dry cells were changed to be inactive. Recharge was applied to the highest active cells of QL layer in the SWI model. In this way, it is expected that the SEAWAT model could run and produced a close match of groundwater head results, relative to the GWF model.

A flow chart summarising the modelling strategy is presented in Figure 5.4. The model development can be subdivided into the following six phases: 1. Groundwater flow model of Knowling et al. (2015) with two layers, 2. Construction of a 10-layer MODFLOW model, 3. Addition of solute transport parameters in the density-dependent SEAWAT model, 4. Simulation of pre-development SWI conditions, 5. SWI simulation using no-pumping scenario with historical recharge (1960-2012) and 6. SWI simulation using historical pumping and recharge (1960-2012). For the pre-development (pre-development recharge and no pumping) density-dependent SWI simulation, the model was run for 800 years to create steady-state conditions and then used as the initial conditions for transient SWI simulations.

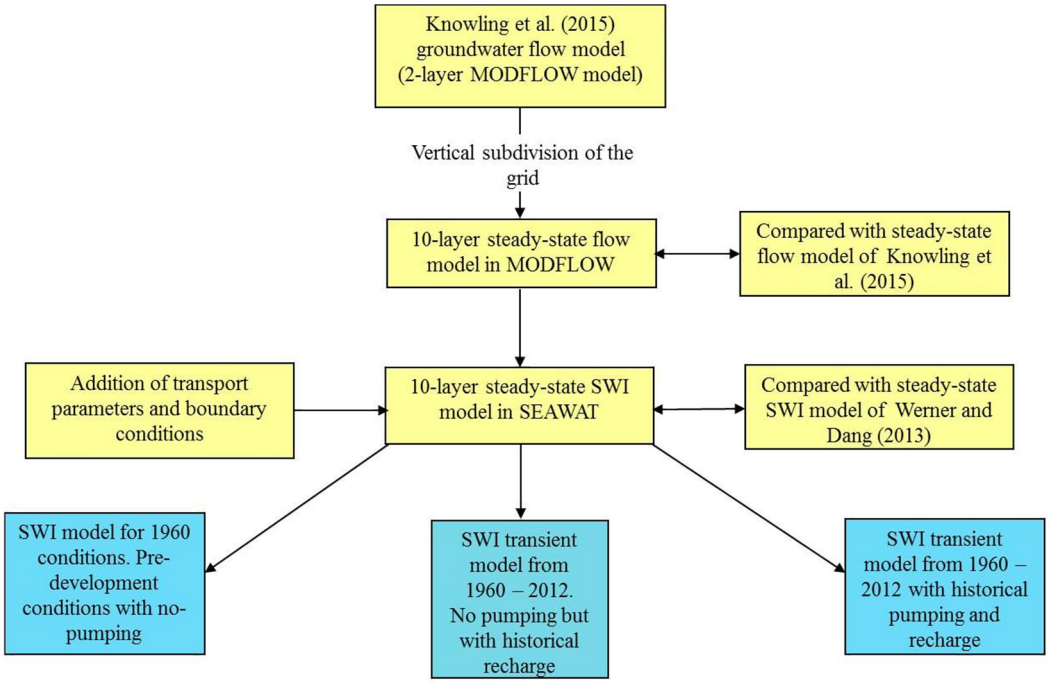

Figure 5.4. A procedure flowchart in developing the SWI model of USB.

Following Knowling et al. (2015), it was assumed that climatic and anthropogenic stresses are represented only by the recharge variability and groundwater pumping, respectively. In order to examine the individual impact of recharge variability and

pumping stresses on the extent of SWI in USB, similar to Knowling et al., (2015), we employed the modelling strategy that involves comparison of simulated natural (i.e., no pumping but with historical recharge) (Scenario 1) and disturbed SWI conditions (i.e., historical pumping with historical recharge) (Scenario 2). To measure the impact of aquifer stresses on SWI across the aquifer, the transient inland locations of the 0.05 relative salt concentration contour (measured perpendicular to the coastline) (x_t [L]) obtained in the SEAWAT model were evaluated in three locations around the coastal area, at the base of QL and TS layers (see Figure 5.5). The salinity distribution from the numerical model results of the pre-development SWI conditions was used as the initial condition of measurement (base line). The transient changes of the total mass of salt in the model (M_s [M]) with time from each SWI scenario were also evaluated. Using these methods, the relative effects of recharge variability and pumping on SWI in USB were examined. To explore the effects of seawater on the groundwater head behaviour around the coast, freshwater only numerical model of Scenario 1 (referred here as Scenario 3) and 2 (referred here as Scenario 4) were also run and then the transient head differences resulted from the recharge and pumping effects during 1976 to 2012 in some selected observation wells near the coast from the density-dependent and freshwater only regional models were compared. In this way, the effects of seawater on groundwater heads behaviour around the coast in response to aquifer stresses can be estimated.

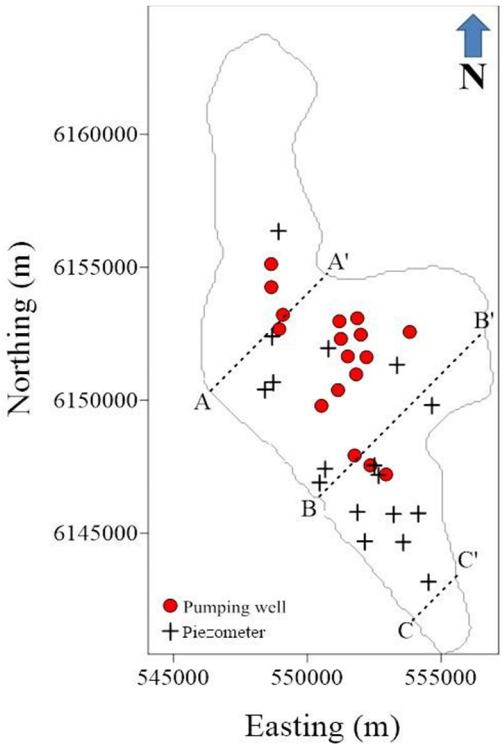

Figure 5.5. Three transect lines (AA′, BB′ and CC′) indicating the locations for SWI extent observation in the model.

5.4.2. Modelling set up

In the GWF model, the same data of the top, bottom, and thickness of each hydrogeological unit as used in Knowling et al. (2015) were used in the model, which were obtained from a combination of bore-log information and airborne electromagnetic surveys (AEM) interpretations (Fitzpatrick et al., 2009). In the current model, 10 layers represent three stratigraphical sequences in the area i.e., six layers for QL, one layer for TC, and three layers for TS. The grid of finite-difference was comprised of 245 rows and 132 columns and a uniform horizontal discretization of 100 m by 100 m was used.

In constructing the GWF model with 10 layers, the aquifer properties, such as hydraulic conductivity K [LT^{-1}] (Figure 5.6), specific yield S_y [-] (Figure 5.7a), specific storage S_s [L^{-1}] (Figure 5.7b), and conductance of the boundary T_c [L^2T^{-1}] (Figure 5.7c) were derived directly from Knowling et al. (2015). The process in transferring the model parameters from 2-layer to 10-layer GWF model was straightforward for most of the

parameters where the parameter arrays were exported and imported with the assistance of Groundwater Vistas 6 (Rumbaugh and Rumbaugh, 2007). Pumping wells that were originally in the single QL layer in Knowling et al. (2015) model now are allocated to Layer 6 (the base of QL layer). The connection between Uley South basin and neighbouring basins was considered occurred through the TS layer and therefore, the inland general head boundary (GHB) conditions that were originally located in the single TS layer, now are allocated at some locations in Layer 10 (the base of TS layer) along the northern part of USB to let water exchanges between the basins (see Figure 5.7c). The south-western coastal boundary that is adjacent to the sea was a fixed, density-corrected coastal head in the model.

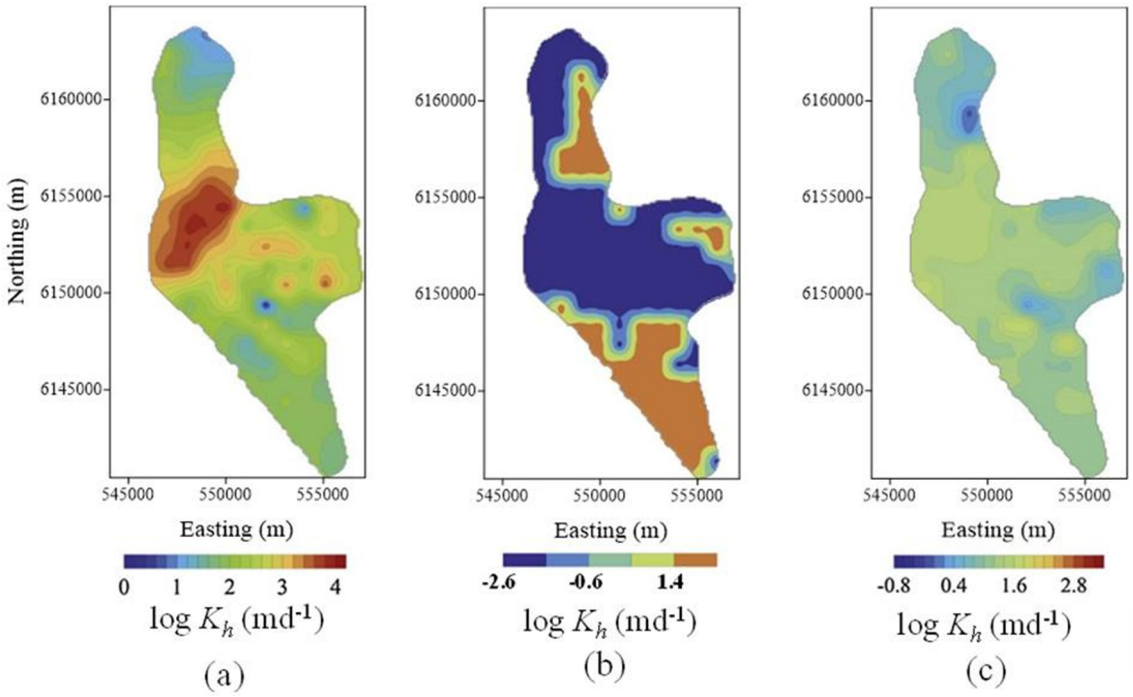

Figure 5.6. Horizontal hydraulic conductivity distributions: (a) K_h QL layer, (b) K_h TC layer and (c) K_h TS layer. Vertical hydraulic conductivity K_v was set to be one tenth of K_h in all layers.

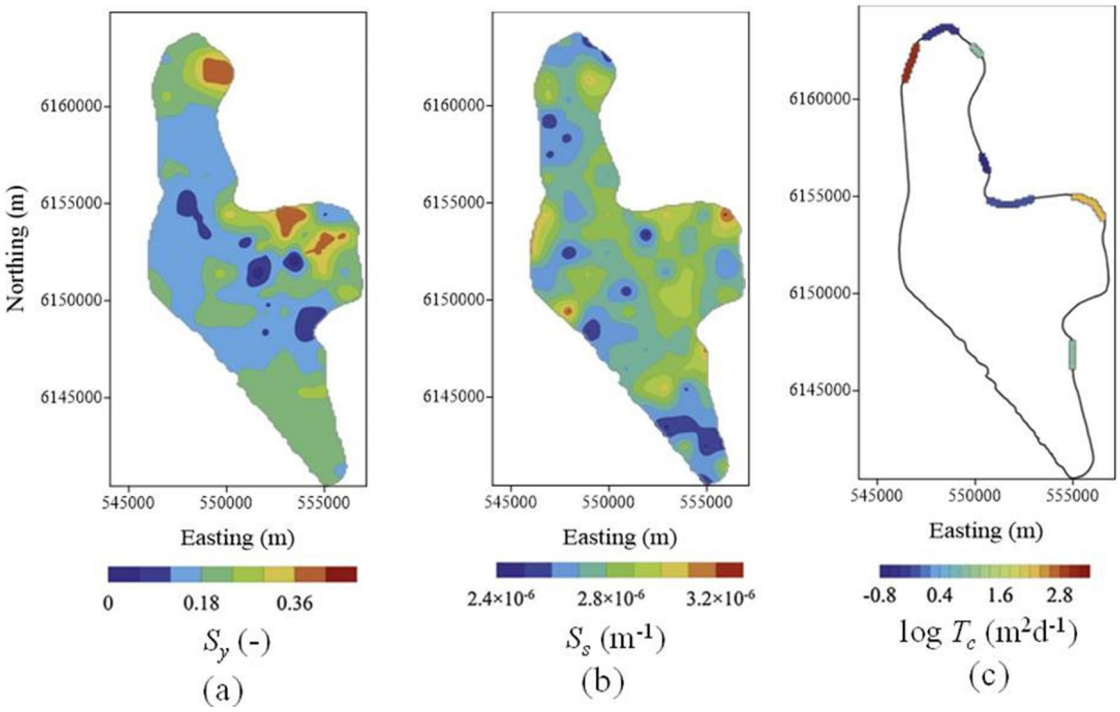

Figure 5.7. Distribution of: (a) specific yield in QL layer (b) specific storage in TS layer (c) boundary conductance T_c for each GHB cells in TS layer.

By considering the typical setting of the aquifer, some additional textbook values were used for solute transport parameters in the SEAWAT model and summarized in Table 5.1.

Table 5.1. Parameters of solute transport model.

Parameter description	Units	Value
Initial relative salt concentration (1 represents saltwater)	-	0.0
Coastal boundary salt concentration	-	1.0
Recharge and inflow salt concentrations	-	0.0
Longitudinal dispersivity (α_L)	m	100
Transverse dispersivity (α_T)	m	10
Vertical dispersivity (α_Z)	m	10^{-4}
Molecular diffusion (D_m)	m^2/day	8.64 x 10^{-5}
QL porosity (n)	-	0.35
TC porosity (n)	-	0.42
TS porosity (n)	-	0.30

5.5. Results

5.5.1. Comparison of head prediction between SWI and MODFLOW groundwater model

Testing of the hydrologic predictions of the 10-layer, density-dependent SEAWAT model for pre-development condition was undertaken by comparing heads from the model to the 2-layer MODFLOW model. The aim was to test the extent to which the calibrated state (in terms of heads) of the MODFLOW model was transferred to the SWI model. A scatter plot of the comparison is given in Figure 5.8. Clearly the match is excellent, although there is a small bias in the SEAWAT predictions, being a 0.08 m under-prediction in water levels on average, relative to the results of the 2-layer MODFLOW model. The root-mean-square error (RMSE) in head predictions between the two models was 0.084 m. The match between the SEAWAT SWI model and the 2-layer steady-state MODFLOW model is considered to be acceptable and therefore, the current seawater intrusion model is considered to be similarly "flow calibrated" as the previous freshwater-only MODFLOW model from Knowling et al. (2015).

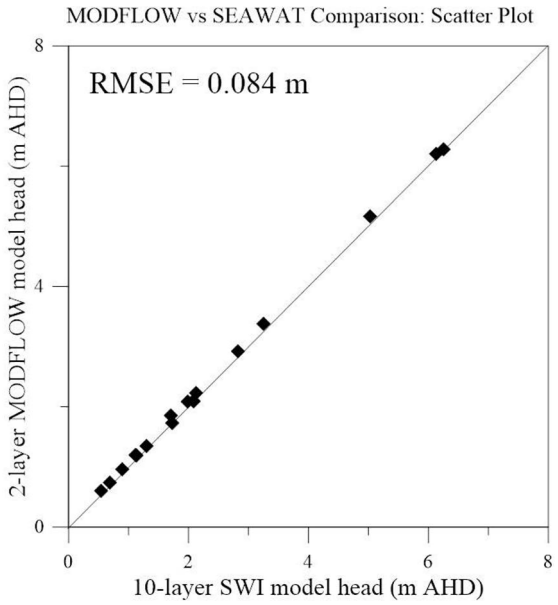

Figure 5.8. Scatter plot of the groundwater head comparison between the 2-layer MODFLOW GWF model and the 10-layer SEAWAT SWI model.

5.5.2. Results of density-dependent SWI simulation for pre-development conditions

The results of a long-term simulation period of pre-development conditions in the Uley South Basin are shown in Figure 5.9. This simulation was run for 800 y, after which time there was no evidence of change in the groundwater head and salinity conditions. This simulation adopts the aquifer stresses representing the condition prior to aquifer development periods (1960-2012). Salinity in the model is expressed in a relative salt concentration where a value of 1 represents seawater. For brevity, the simulated results presented comprise: (1) Salinities at the end of the simulation period in Layer 2 (Upper QL), 6 (QL bottom), 8 (Upper TS) and 10 (TS bottom). Based on the 0.5 of relative salt concentration contour, Werner and Dang (2013) obtained the maximum inland toe positions of 500 m in the QL and 2500 m in the TS with their SWI numerical model under pre-development conditions, while in the current study, the maximum wedge toe position obtained in the pre-development conditions was about approximately 600 m in the QL (Layer 6) and 1700 m in the TS (Layer 10). The pre-development salinity results are reasonably consistent with the results of Werner and Dang (2013), even though some deviations in the magnitude of SWI were still observed. The deviations on the results are likely caused by the differences in the spatial variability of hydraulic properties adopted in these two studies.

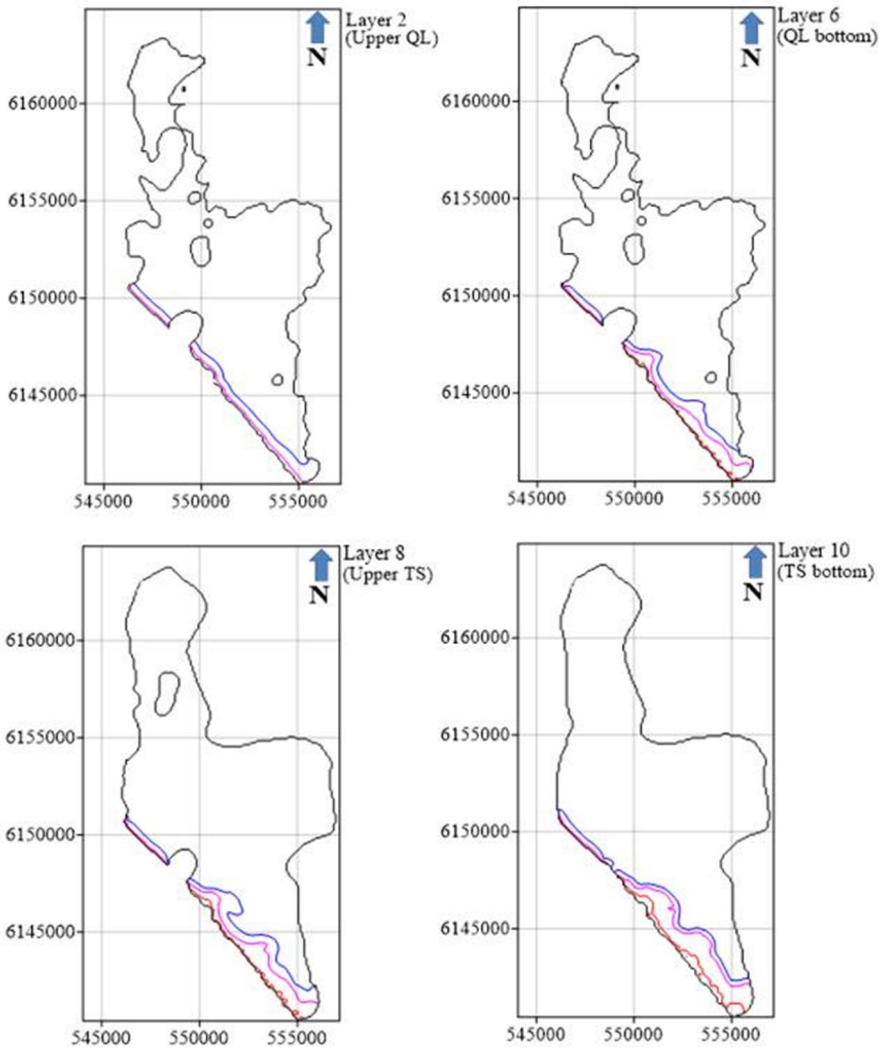

Figure 5.9. Salinity distributions from the density-dependent, steady-state prediction of the pre-development scenario for Layers 2, 6, 8 and 10. Blue, magenta and red lines represent the 0.05, 0.50 and 0.95 of relative salt concentration contours.

As can be seen in Figure 5.9, the zone of saline groundwater in adjacent to the southeast coastline was the same location as that reported by Fitzpatrick et al. (2009) from airborne electromagnetic (AEM) survey, even though the saline groundwater plume adjacent to the northwest coastal was not detected by Fitzpatrick et al. (2009) (see Figure 5.10). It is difficult to compare in detail between the given AEM survey data and the model results, however, the given AEM survey data is still worthwhile to confirm (at least under regional scale) the results from the numerical model.

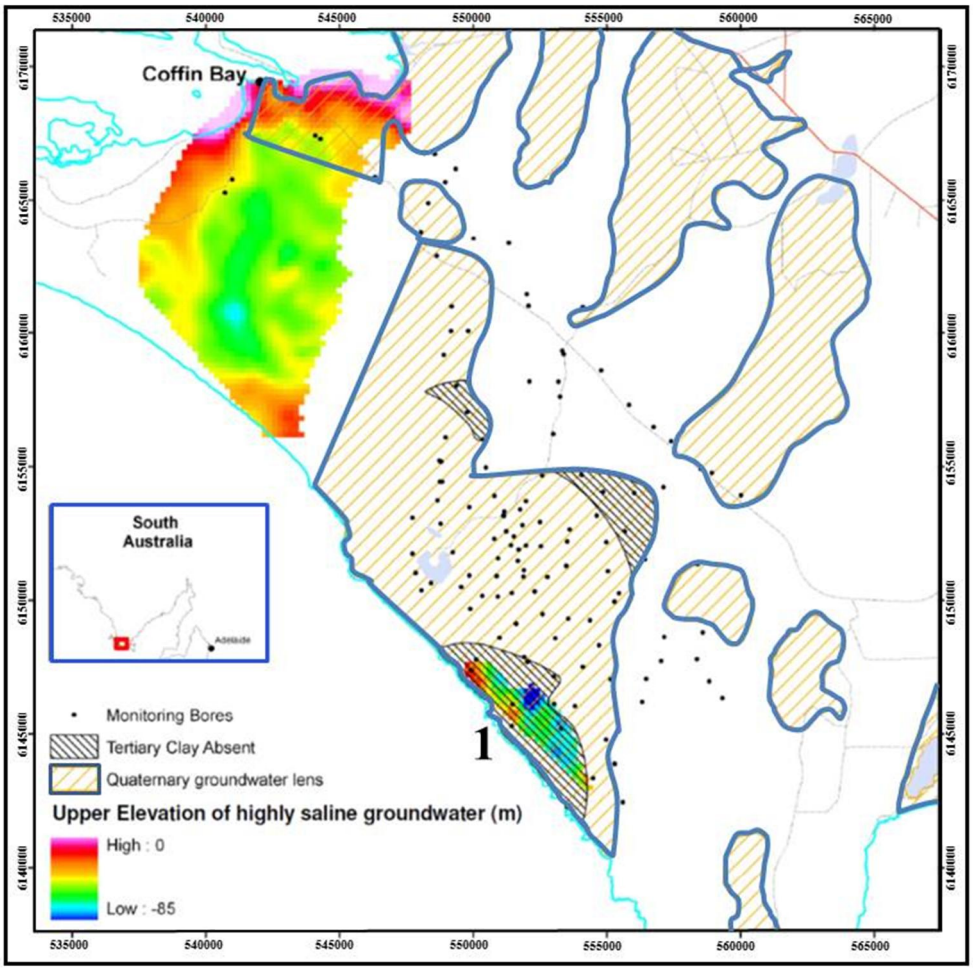

Figure 5.10. Upper surface area of saline intrusion obtained from AEM survey conducted by Fitzpatrick et al. (2009) (Werner and Dang, 2013). Location 1 indicates the area with highly saline groundwater.

5.5.3. SWI transient model using historical recharge with no pumping (Scenario 1)

This scenario was produced to explore the simulated changes in aquifer condition (i.e., groundwater head and salinity distribution) that occurs in the absence of pumping but with historical recharge conditions. This scenario purposes to show the effects of historical recharge alone and to isolate the effects of historical pumping on the aquifer conditions after the pre-development period. The recharge used to produce the initial conditions (equal to 14.8 GL/year) was higher than the average recharge occurring during 1960-2012 (i.e. 13.7 GL/year), and therefore a drop in groundwater head and a slight inland shift in the interface was expected in the model predictions. The salinity distribution after 52 years is presented in Figure 5.11. Figure 5.11 shows a slightly

larger salt wedge compared to the pre-development results given in Figure 5.9. Landward salinity movements were most evident in the QL sequence (particularly in the south-western part of the basin) rather than the TS sequence, although overall salinity changes were fairly small when visualised at the basin-scale. Put simply, the lower recharge produced a lower inland head, which in turn induced a change in the salt wedge extent. In Scenario 1, the maximum inland toe position obtained at the end of simulation period in 2012 using the 0.05 relative salinity contour in the QL layer was 1531 m and in the TS layer was 1922 m. These values were 1404 m and 1907 m, respectively, at the pre-development conditions.

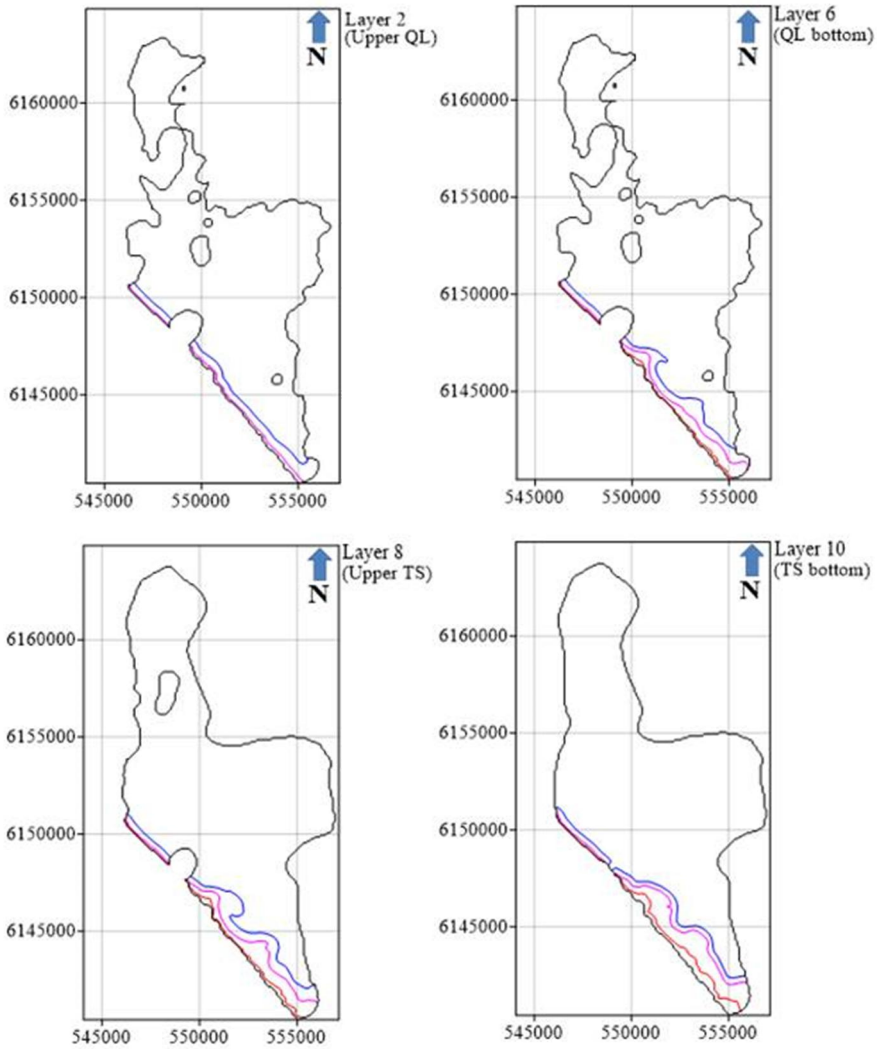

Figure 5.11. Salinity distributions at the end of simulation of Scenario 1 for Layers 2, 6, 8 and 10. Blue, magenta and red lines represent the 0.05, 0.50 and 0.95 of relative salt concentration contours.

5.5.4. SWI transient model using historical recharge and pumping (Scenario 2)

In reality there is a strong seasonal variability in recharge and a related variability in pumping that occurs in the USB, and it is reasonable to infer that this may exacerbate SWI due to the combination of pumping and recharge during the summer times. In order to assess the influence of historical climate and variability of pumping on SWI in USB, an attempt was made here by considering the variations in recharge and pumping over the period 1960 to 2012. The Scenario 2 results are presented in Figures 5.12. The salinity contours of Figure 5.12 identified landward wedge movements that are larger than those of the previous simulation involving no pumping (Scenario 1). Enlargement of the south-western wedge which relatively closer to the pumping wells was especially noticeable in the QL layer while a slight enlargement of the wedge in the north-western part of USB was evident from the basin-scale images. Only a slight expansion of the wedge was observed in the TS layer which is hardly seen from the regional scale images but the wedge expansion is larger than that in Scenario 1. In Scenario 2, the maximum inland toe positions obtained at the end of the simulation period in 2012 using the 0.05 relative salinity contour in the QL and TS layers were 1645 and 1944 m, respectively.

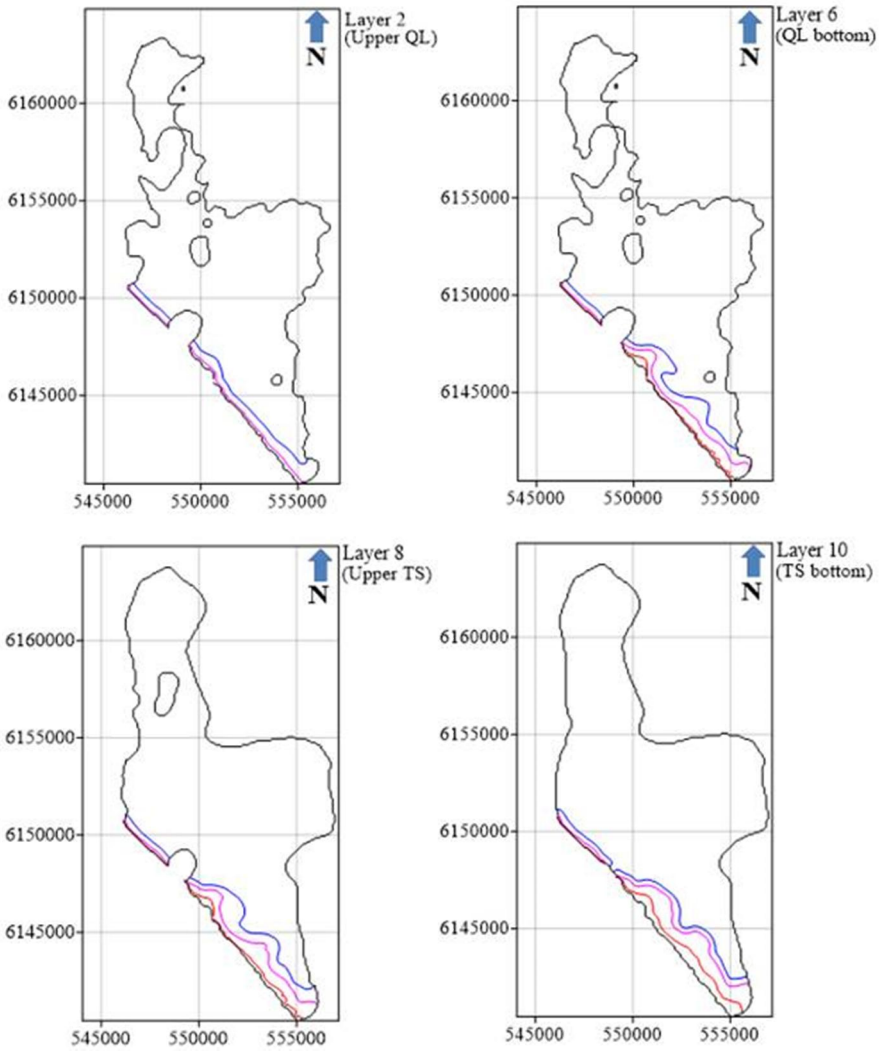

Figure 5.12. Salinity distributions at the end of simulation of Scenario 2 for Layers 2, 6, 8 and 10. Blue, magenta and red lines represent the 0.05, 0.50 and 0.95 of relative salt concentration contours.

Simulated pre-development salinity profiles in 2004 at bores SLE69 and ULE205 are illustrated in Figure 5.13. These are somewhat consistent with the sonde profiles that are illustrated in Figure 5.13 for the same time of observation (Clarke, 2005). It needs to be reinforced here that the current model was not meant to predict individual bore salinity profiles; however, it is clear that the model performed reasonably well against existing field observations, especially considering that the transport parameters are not calibrated and given the inherent limitations of SWI simulation.

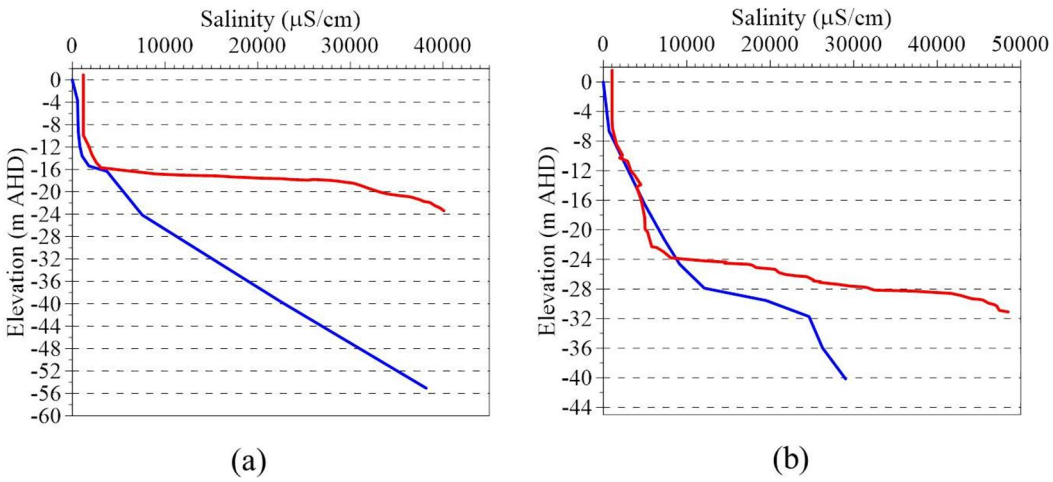

Figure 5.13. Salinity profiles in wells: (a) SLE69 and (b) ULE205. Blue and red lines represent simulated and observed (sonde) salinities, respectively. The observed salinity profiles in SLE 69 and ULE 205 were taken on November and June 2004, respectively.

5.5.5. Relative effects of recharge variability and pumping on SWI

Figure 5.14 shows the transient groundwater head dynamics resulting from Scenarios 1 and 2 in selected piezometers ULE205, ULE206, SLE5, SLE9, SLE11, SLE69, SLE8 and ULE207. Observed groundwater head data from the field site (Water Connect) are also presented in the graph for the purpose of comparison. A decreasing trend of groundwater heads was demonstrated in Scenario 1 (no pumping scenario with historical recharge) which indicates a decline of groundwater heads due to the effect of the lower average historical recharge magnitude relative to the pre-development recharge, as stated above. The drawdown was spatially variable and in the order of roughly 20 cm. A reasonable match of groundwater heads was noticed between observed groundwater head data from Water Connect and Scenario 2. As expected, the same dynamic of groundwater heads between Scenarios 1 and 2 from 1960 to 1976 was noticed, and Scenario 2 hydrographs showed a marked response to the 1976 and 2012 changes in pumping where lower groundwater heads were observed relative to that in Scenario 1.

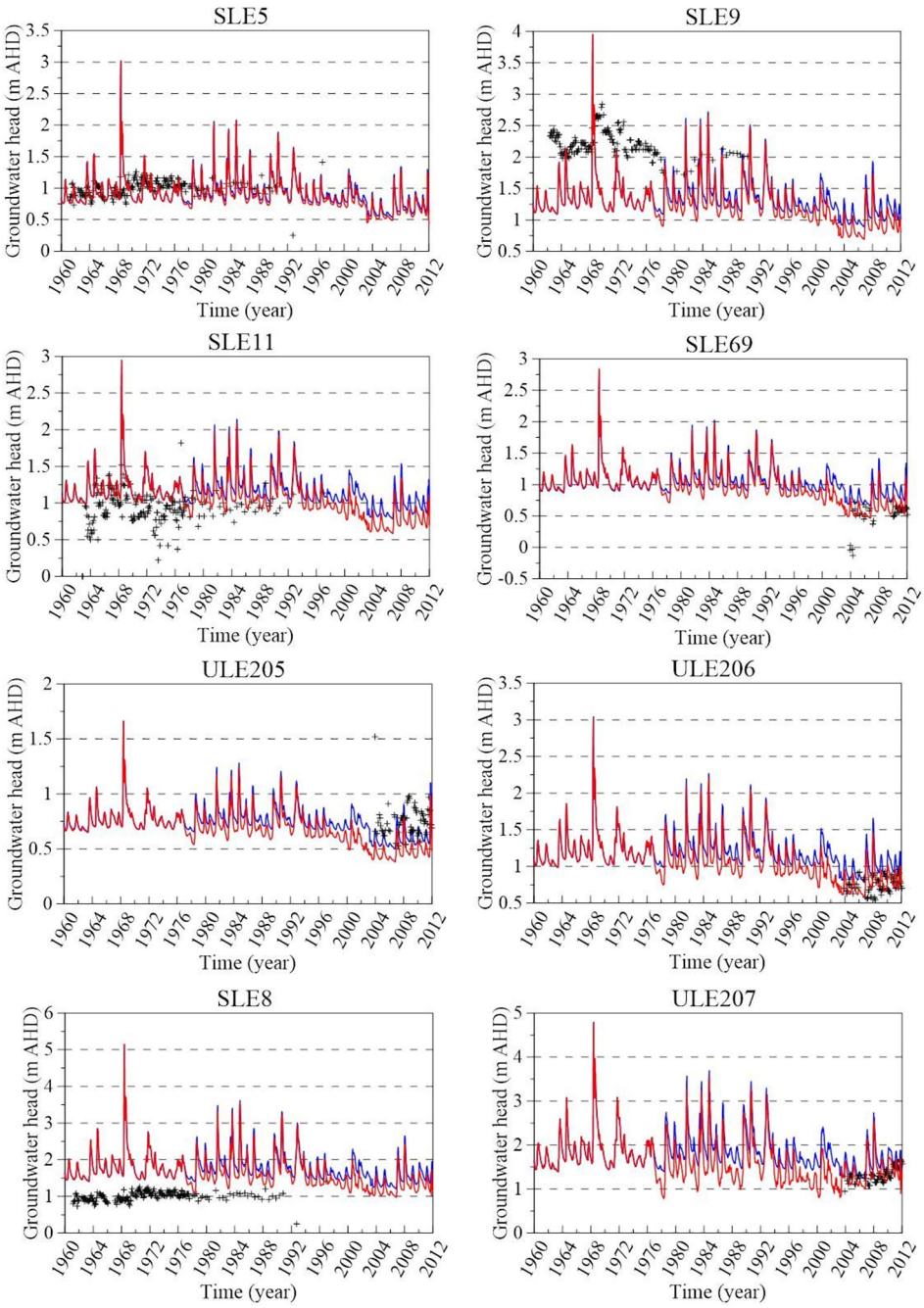

Figure 5.14. Observed and simulated groundwater head dynamics obtained from Scenarios 1 and 2 in some selected observation wells. Blue and red lines represent the groundwater heads from Scenarios 1 and 2, respectively. The observed groundwater heads are represented by the plus (+) symbol.

The trends in salinity in Scenarios 1 and 2 at the bottom of QL are assessed through plots of salinity trends at individual sites within the model, i.e. via the salinographs given in Figure 5.15. As can be seen, the response of simulated salinity in these observation wells was not as dynamic as the response of groundwater heads on the

changes of historical recharge and pumping. In Scenarios 1 and 2, increases in detectible salinity (i.e. only predicted salinities greater than 10^{-4} as a fraction of seawater are considered in this study) were observed in piezometers ULE205, ULE206, SLE5, SLE9, SLE11 and SLE69. Greater increases of salinity were observed in Scenario 2 from 1976 to 2012 in these piezometers as the result of pumping stresses, as expected. Note that none of these are in the vicinity of production bores. Despite similar groundwater heads in ULE207 as there were in more saline piezometers in the south-western part of USB; i.e. in the order of 0.6-0.7 m AHD, ULE207 showed no signs of salinization (the results are not shown for brevity). Clearly, the north-western and south-western parts of the USB model are behaving differently which is likely due to the contrast in aquifer properties of these areas.

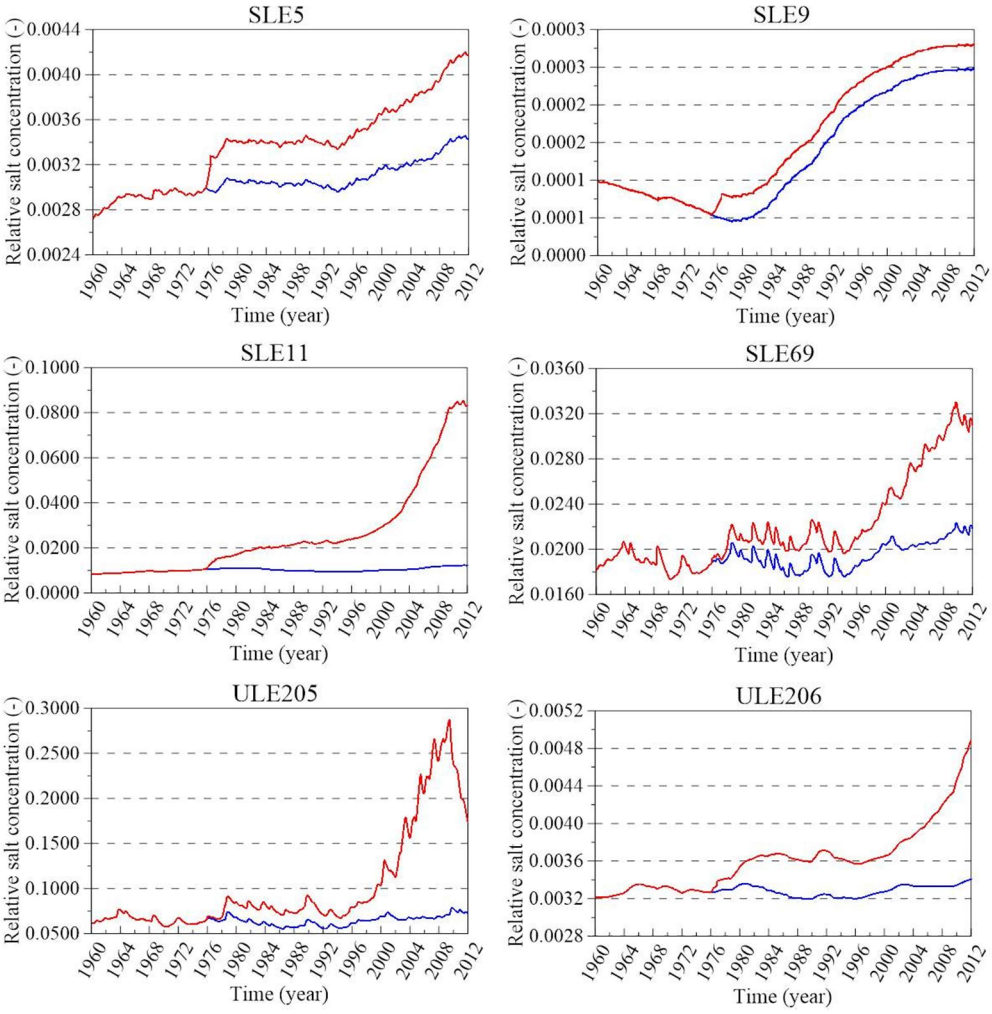

Figure 5.15. Comparison between the transient salinity changes from Scenarios 1 and 2 at the bottom of QL in some selected observation wells. Blue and red lines represent the results from Scenarios 1 and 2, respectively.

Figure 5.16 shows the changes of total salt of mass M_s in the aquifer obtained from Scenarios 1 and 2. The value of M_s from the pre-development condition (i.e., 9.50 x 10^7 kg) is also presented as a comparison. In Figure 5.16, long term M_s trends for Scenario 1 are characterised by: (1) considerable increase from 1960 to 1963 (mean rainfall during this period is 457 mm/y), (2) significant decrease from 1964 to 1969 (mean rainfall is 528 mm/y), (3) increase between 1970 and 1977 (mean rainfall is 548 mm/y), (4) gradual decrease from 1978 to 1986 (mean rainfall of 612 mm/y), (5) slight increase during 1987 to 1989 (mean rainfall is 534 mm/y), (6) most decrease between 1990 and 1992 (mean rainfall is 652 mm/y), (7) gradual increase from 1993 to 2009 (mean rainfall is 520 mm/y) and (8) somewhat decrease during 2010 to 2012 (mean rainfall is 483 mm/y). The maximum M_s in Scenario 1 is 9.81 x 10^7 kg that occurred in 2009 following the long-term low rainfall period between 1993 and 2009. In Scenario 2, the trends of M_s are characterised by: (1) the same trends as Scenario 1 during 1960 to 1975 (no pumping), (2) significant increase from 1976 to 1978 (the mean pumping rate during this period is 3483 ML/y), (2) slow decrease from 1979 to 1986 (mean pumping of 5675 ML/y), (3) significant increase from 1987 to 1989 (mean pumping of 5133 ML/y), (4) considerable decrease from 1990 to 1993 (mean pumping of 3250 ML/y), (5) gradual increase between 1994 and 2009 (mean pumping of 6447 ML/y) and (6) somewhat decrease during 2009 to 2012 (mean pumping of 5375 ML/y). The maximum values of M_s in Scenarios 2 is 1.04 x 10^8 kg that occurred in 2009 and slightly decreased in trend thereafter due to the decrease of pumping after 2009. Between 1976 and 2012, the M_s in Scenario 2 was higher on average than that in Scenario 1 by 3.25 x 10^6 kg. At the end of simulation period (2012), the value of M_s in Scenario 2 was 2.4 times higher than that in Scenario 1, relative to the pre-development M_s value. This indicates the higher contribution of pumping relative to climate variability on the magnitude of SWI in the USB coastal aquifer. These results are reasonably consistent with the finding from the previous freshwater-only study (Knowling et al., 2015) stated previously, that demonstrated the higher impact of pumping compared to the climate on the aquifer depletion in the USB coastal aquifer.

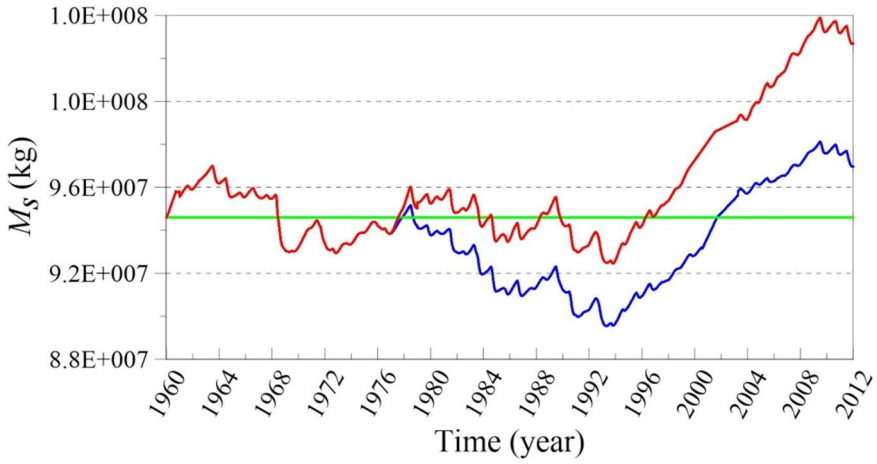

Figure 5.16. Comparison between the transient changes of M_s in the aquifer from Scenarios 1 and 2. Blue and red lines represent the M_s from Scenarios 1 and 2, respectively. Green line represents the value of M_s from the pre-development condition.

Figure 5.17a and 5.17b provide the transient locations of the 0.05 relative salt concentration contour (x_t) at the base of QL and TS layers, respectively, measured from the coastline after pre-development conditions, both in Scenarios 1 and 2. This aims to examine the effects of groundwater pumping on SWI relative to recharge variability, in terms of SWI extent perpendicular to the coastline at three locations (i.e., Line AA′ at the north-western part of the USB and Lines BB′ and CC′ at the south-western part of the USB) around the coastal area (see Figure 5.5). Generally, the trends of changes in the x_t observed are relatively similar to the trends in the changes of M_s in the model. Under steady-state pre-development conditions, the x_t at Lines AA′, BB′ and CC′ at the base of QL layer (Figure 5.17a) were 248, 1052 and 994 m, respectively and at the base of TS layer (Figure 5.17b) were 407, 1175 and 1224 m, respectively. Relative to Scenario 1, larger magnitude of x_t during 1976 to 2012 was observed in Scenario 2, as expected. Between 1976 and 2012, the x_t values in Scenario 2 at Lines AA′, BB′ and CC′ were higher on average than that in Scenario 1 by 3, 77 and 35 m, respectively in the QL and 4, 39 and 18 m in the TS. In Scenario 1, the maximum x_t at Lines AA′, BB′ and CC′ in the QL that occurred in 2009 were 251, 1098 and 1047 m, respectively, and were 412, 1220 and 1245 m, respectively in the TS. In Scenario 2, the maximum x_t values at Lines AA′, BB′ and CC′ in the QL in 2009 were 253, 1304 and 1076 m, respectively, and were 414, 1317 and 1273 m, respectively in the TS. At the end of the simulation period in 2012, the values of x_t in the QL in Scenario 1 at Lines AA′, BB′

and CC′ were 250, 1087 and 1034 m, respectively and were 410, 1201 and 1240 m, respectively in the TS. In Scenario 2, the x_t values in 2012 in the QL at Lines AA′, BB′ and CC′ were 252, 1286 and 1070 m, respectively and were 413, 1307 and 1270 m, respectively in the TS. Compare to the x_t values of Scenario 1 in 2012, the x_t values at Lines AA′, BB′ and CC′ in Scenario 2 were 0.6, 5.8 and 0.9 times larger in the QL and were 0.7, 4.1 and 1.8 times larger in the TS, relative to the x_t value of pre-development conditions in each respective observation lines. It was noticed that the relative impact of pumping on SWI in Line BB′ was higher than that in Lines AA′ and CC′ in both QL and TS. This is due to the location of Line B which is relatively closer to the pumping wells compared to the locations of Lines AA′ and CC′.

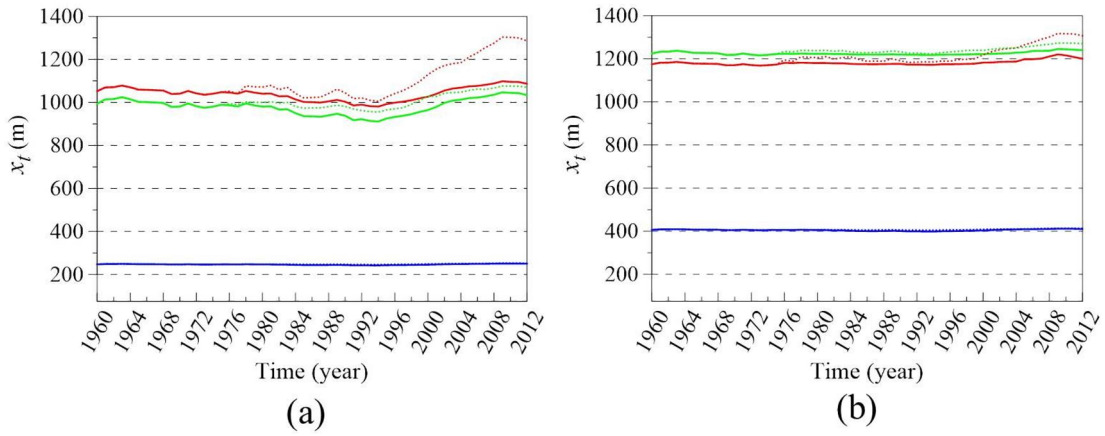

Figure 5.17. The transient locations of x_t in transect lines AA′ (blue line), BB′ (red line) and CC′ (green line) (see Figure 5.5) at the base of: (a) QL layer and (b) TS layer. Solid and dotted lines represent the results from Scenarios 1 and 2, respectively.

5.5.6. Seawater effects on the groundwater head behaviour near the coast

Figure 5.18 shows the transient fresh groundwater head differences in Layer 2 of QL resulted from the pumping effects during 1976 to 2012 in the density-dependent (Scenarios 1 and 2) and freshwater only regional models (Scenarios 3 and 4) in some selected piezometers around the coast (i.e., ULE205, ULE206, SLE5, SLE11 and SLE69). For the purpose of comparison, one observation well which is relatively far from the coast (i.e., ULE138) is also presented in Figure 5.18.

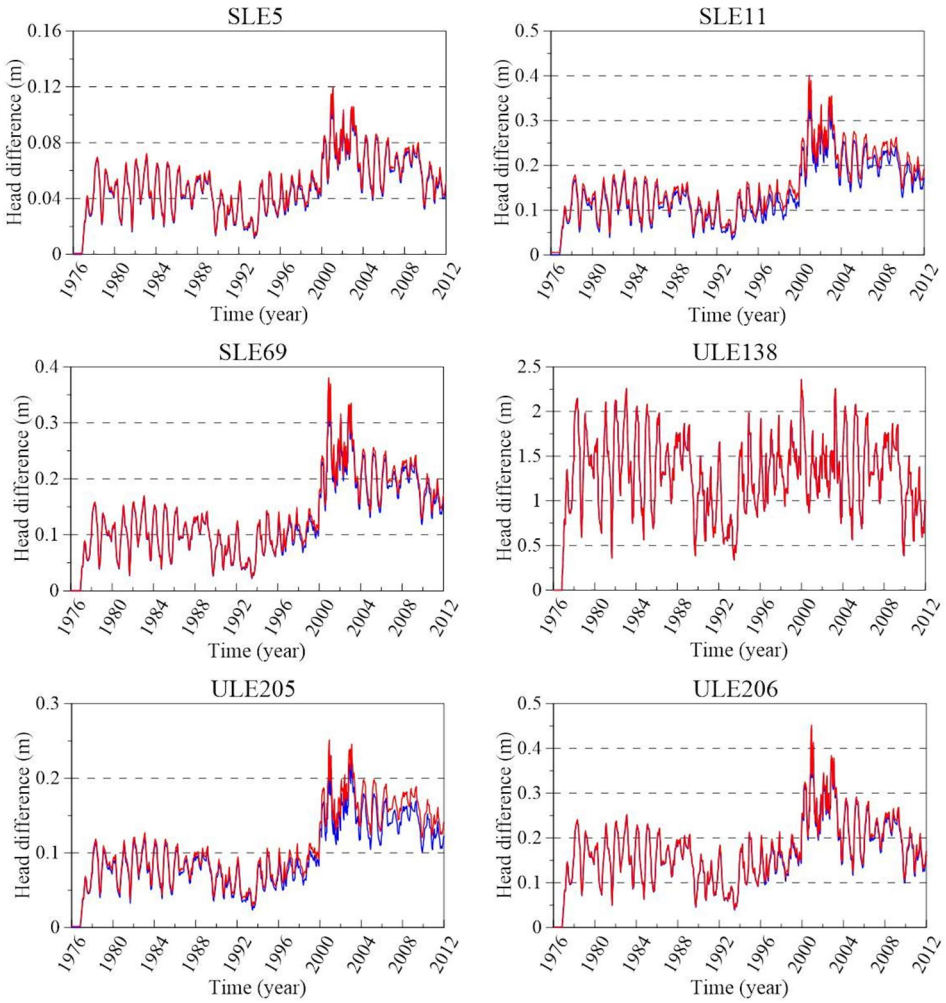

Figure 5.18. Comparison of transient fresh groundwater head differences resulted from the pumping effects in the density-dependent (red line) and freshwater only (blue line) regional models in some selected observation wells.

Figure 5.18 shows that the head differences resulted from the pumping effects from the density-dependent models (Scenarios 1 and 2) were slightly larger on average than that from the freshwater only models (Scenarios 3 and 4) in the selected observation wells near the coast i.e., ULE205 (1.44 cm), ULE206 (0.47 cm), SLE5 (0.19 cm), SLE11 (1.02 cm) and SLE69 (0.55 cm). Meanwhile, no head differences were observed in ULE138, as expected. These results are in accordance with the small scale 2D pre-numerical model results. This indicates that relative to the freshwater only model, involving seawater as performed in the density-dependent models (Scenarios 1 and 2) increased the effects of pumping on the fresh groundwater head response around the coast in the USB numerical model, particularly in the areas where seawater intrusion were predicted to be occurred. From selected observation wells, it was noticed that the

effect of pumping on the fresh groundwater head response above the freshwater-saltwater interface in the density-dependent model becomes larger as the relative salinity below in the well increases (see Figures 5.15 and 5.18). These results suggest that including seawater in the regional groundwater numerical model of coastal aquifers is critical, and ignoring it may lead to the underestimation of the effects of aquifer stresses on the groundwater head distributions around the coastal area.

5.6. Conclusion

Investigating the relationship between climate variability, anthropogenic stresses and the extent of SWI using numerical model is critical for developing an effective strategy to protect the groundwater resources in coastal aquifers. No regional SWI studies available to date made an effort to differentiate the effects of climate variations and pumping stresses on the magnitude of SWI, particularly when the patterns of SWI is involving the spatial and temporal variations of aquifer stresses. In this paper, the individual contribution of recharge variability and pumping stresses on the extent of SWI was examined under spatial and temporal variability conditions using regional SWI numerical model. The seawater effects on the fresh groundwater head behaviour near the coast were also investigated in this study.

The results perform a good agreement with the previous SWI studies in USB where reduced recharge and increased groundwater extraction have negative effects on the USB groundwater system, due to the decline of groundwater heads and increased salinities, even though these effects are small in terms of regional scale. The modelling results show that the effects of climate and pumping on the extent of SWI are highly varied in time and space. While the effects of pumping in USB are more pronounced than those of reduced recharge, the same relationship may not occur in aquifers where pumping is a much smaller proportion of the total recharge to the aquifer. At the end of simulation period (2012), the impact of pumping on the extent of SWI (in terms of 0.05 of relative salt concentration) at the coastal zones near the pumping wells in the QL and TS layers are shown to be 5.8 and 4.1 times higher to that of climate. In terms of the total salt mass in the aquifer, the effect of pumping on SWI in 2012 is shown to be 2.4 times higher relative to the climate. These results show the higher contribution of

pumping relative to the climate in increasing the magnitude of SWI in the USB coastal aquifer, and therefore a more careful pumping management is highly required to minimize this effect on the future for sustainable water resources in this area.

The results of numerical model also show that involving seawater to some extent affect the behaviour of groundwater head near the coast where the fresh groundwater head differences resulted from the pumping stresses are slightly higher (around 0.19 to 1.4 cm on average) compared to those in the freshwater numerical model only. The results of this study suggest that involving seawater in the regional groundwater numerical model is essential because it can influence the relative contributions of aquifer stresses on the groundwater head distributions around the coastal area. This study demonstrates the application of simple analysis to evaluate the individual impact of aquifer stresses on the extent of SWI and also the influence of seawater buoyancy in affecting the fresh groundwater head behaviour in the coastal zones.

6. CONCLUSION

This thesis encompasses a comprehensive evaluation of transient SWI where characteristics of passive and active SWI, and any new phenomenon related to these types of SWI are investigated using physical and numerical models. The results of this study offer insight into transient SWI processes (especially for active SWI) in response to FHD and can be used as a basis and a reference in understanding the transient behaviour of active SWI, given the lack of transient active SWI literatures exist and some evidences which showed that active SWI is occurring and threatens the coastal groundwater resources around the world.

The results in Chapter 2 showed that major WTS may occur under active SWI because of the cessation of fresh groundwater discharge to the sea. Minor WTS may occur with passive SWI under certain conditions i.e., increased dispersivity, increased hydraulic conductivity and decreased freshwater discharge. Particle tracking model results demonstrated that seawater circulation was present under passive SWI and ceased under active SWI conditions and it is clear that WTS is derived from the lateral movement of saltwater from the sea boundary. An analysis of four previously published SWI field cases showed that WTS may occur at rates up to 66 m/y. In this study, minor WTS was modelled in the Willunga basin which experiences passive SWI while major WTS was simulated in the other three field cases (i.e., Pioneer Valley unconfined aquifer, Korba aquifer and Cape Range Group aquifer) which undergo active SWI. Salinities at the watertable are mainly less than 50% of seawater in all field cases which indicates that WTS is mainly associated with brackish water from the mixing zone. The results suggest that the likelihood of WTS to occur in a real-world setting is high, particularly within aquifers where groundwater levels are lower than sea level.

The results in Chapter 3 demonstrated that Case 1 produces optimal matches to both numerical model results and sand-tank observations, in terms of both the saltwater wedge location and the upward freshwater leakage rate and distribution, albeit all sharp-interface models over-predict the extent of saltwater, both in steady-state and transient conditions. The restriction of upward freshwater leakage in Case 2 produces freshwater outflow faces at the sea boundary of the lower aquifer that are not otherwise expected

and the conversion of lower aquifer freshwater to upper aquifer saltwater in Case 3 causes an over-estimation of the extent of upper aquifer saltwater. For field-scale systems with low conductance between overlying aquifers (Case 3) produces an unstable situation of complete salinization of the upper aquifer, in contradiction to the other methods. Streamlines predicted by the dispersive model highlight that the assumptions of Case 1 are best matched to the physical processes of upward freshwater leakage in the aquifers considered here and this finding lead to the recommendation that Case 1 is the optimal approach for the treatment of upward freshwater leakage in sharp-interface models of layered aquifers.

The results in Chapter 4 revealed that under active SWI, the SWI response time-scales were influenced by both the initial and final boundary head differences. The freshwater-saltwater interface was found to be steeper under stronger advection (i.e., caused by the inland FHD), higher dispersivity and hydraulic conductivity, and lower aquifer thickness, seawater density and porosity. The interface movement was faster and the mixing zone was wider with larger hydraulic conductivity, seawater-freshwater density difference and aquifer thickness, and with lower porosity. Advection effects become more dominant on the interface movement relative to density effects as SWI becomes more active. It was observed that the rate of active SWI could be reasonably predicted using density-independent formulae when the advective transport rate was greater than 0.08 m/d. The results showed that dimensionless parameters (Peclet number and mixed convection ratio) from previous steady-state analyses offered only limited application to the controlling factors of passive SWI, and are not applicable to active SWI. Complex relationships were noticed between SWI variables and model parameters, whereby none of the SWI variables show the same type of response (i.e., rising, falling, etc.) to the change of parameter under both passive and active SWI conditions. This highlights significant differences between the controlling factors of active and steady-state SWI.

Finally, Chapter 5 showed reasonable agreement of the pre-development salinity distribution between the current model results and the results from the previous USB SWI studies. The modelling results showed that at the end of the simulation period in 2012, the effect of pumping on the extent of SWI in the Quaternary (QL) and Tertiary Sand (TS) layers of USB were shown to be larger, by 5.8 and 4.1 times, respectively,

relative to SWI arising from climate variability. In terms of total mass of salt in the aquifer, the effect of pumping on SWI in 2012 was 2.4 times higher than climate impacts. The results also showed that involving seawater in the numerical model modified the groundwater behaviour near the coast where the groundwater head differences resulted from the pumping effects were slightly larger (around 0.19 to 1.4 cm on average) relative to those without seawater simulated in the model.

Some future works related to this research are required. For example, there is a need to do field investigations of WTS phenomenon associated with active SWI. Furthermore, it is also important to conduct further explorations of active SWI characteristics which involve the aquifer heterogeneity, recharge and sea level rise in coastal aquifers.

REFERENCES

Abarca, E., J. Carrera, R. Held, X. Sanchez-Vila, M. Dentz, W. Kinzelbach and E. Vazquez-Sune (2004). Effective dispersion in seawater intrusion through heterogeneous aquifer. 18th Salt Water Intrusion Meeting, Cartagena, Spain, IGME, 31 May – 3 June 2004.

Abarca, E., J. Carrera, X. Sanchez-Vila and M. Dentz (2007). Anisotropic dispersive Henry problem. Advances in Water Resources 30: 913-926, doi: 10.1016/j.advwatres.2006.08.005.

Alcoe, D. (2009). Evaluating measures for sustainability of groundwater use in Uley South lens, Southern Eyre Peninsula, South Australia. Unpublished Honours Thesis. Flinders University. Adelaide. 66pp.

Allow, K. A. (2011). Seawater intrusion in Syrian coastal aquifers, past, present and future, case study. Arabian Journal of Geosciences 4: 645-653, doi: 10.1007/s12517-010-0261-8.

Ataie-Ashtiani, B. (1998). Contaminant transport in coastal aquifers. PhD thesis. University of Queensland. Brisbane. Australia.

Ayni, F. E., S. Cherif, A. Jrad and M. Trabelsi-Ayadi (2011). Impact of treated wastewater reuse on agriculture and aquifer recharge in a coastal area: Korba case study. Water Resources Management 25: 2251-2265, doi: 10.1007/s11269-011-9805-2.

Badaruddin, S., A. D. Werner and L. K. Morgan (2015). Watertable salinization due to seawater intrusion. Water Resources Research 51: 8397-8408, doi: 10.1002/2015WR017098.

Bakker M. (2006) Analytic solutions for interface flow in combined confined and semi-confined coastal aquifers. Advances in Water Resources 29: 417-25, doi: 10.1016/j.advwatres.2005.05.009.

Bakker, M., F. Schaars, J. D. Hughes, C. D. Langevin and A. M. Dausman (2013). Documentation of the seawater intrusion (SWI2) package for MODFLOW. U.S. Geological Survey Techniques and Methods. Book 6. Chapter A46. 47pp. http://pubs.usgs.gov/tm/6a46/.

Barnett, S. R. (1978). Eyre Peninsula groundwater survey - Uley South basin. Department of Mines and Energy. Report 78/22. Government of South Australia. Adelaide. 45pp.

Bear, J. and G. Dagan (1964). Moving interface in coastal aquifers. Journal of the Hydraulics Division 90: 193-216.

Bear, J. (1979). Hydraulics of Groundwater. McGraw-Hill. New York.

Bear, J., A. H. -D. Cheng, S. Sorek, D. Ouazar and I. Herrera (1999). Seawater Intrusion in coastal aquifers-concepts, methods and practices. Springer publication 14. 627pp.

Benson, D. A., A. E. Carey and S. W. Wheatcraft (1998). Numerical advective flux in highly variable velocity fields exemplified by saltwater intrusion, Journal of Contaminant Hydrology 34: 207-33, doi: 10.1016/S0169-7722(98)00093-X.

Bekesi, G., M. McGuire and D. Moiler (2009). Groundwater allocation using a groundwater level response management method-Gnangara groundwater system, Western Australia. Water Resources Management 23: 1665-1683, doi: 10.1007/s11269-008-9346-5.

Bocanegra, E., G. C. Da Silva Jr, E. Custodio, M. Manzano and S. Montenegro (2010). State of knowledge of coastal aquifer management in South America. Hydrogeology Journal 18: 261-267, doi: 10.1007/s10040-009-0520-5.

Bouzouf, B., D. Ouazar, M. Himi, I. Elmahi and F. Benkhaldoun (2001). Integrating hydrogeochemical and geophysical data for testing a finite volume based numerical model for saltwater intrusion. Transport in Porous Media 43: 179-194, doi: 10.1023/A:1010638200048.

Brovelli, A., X. Mao and D. A. Barry (2007). Numerical modelling of tidal influence on density-dependent contaminant transport. Water Resources Research 43: 1-15, doi: 10.1029/2006WR005173.

Bureau of Meteorology, 2010. SILO database. <http://www.bom.gov.au/silo/> (accessed 7 January, 2017).

Chang, S. W. and T. P. Clement (2013). Laboratory and numerical investigation of transport processes occurring above and within a saltwater wedge. Journal of Contaminant Hydrology 147: 14-24, doi: 10.1016/j.jconhyd.2013.02.005.

Chang, S. W. and T. P. Clement (2013). Laboratory and numerical investigation of transport processes occurring above and within a saltwater wedge. Journal of Contaminant Hydrology 147: 14-24, doi: 10.1016/j.jconhyd.2013.02.005.

Cheng, A. H. D., D. Halhal, A. Naji and D. Ouazar (2000). Pumping optimization in saltwater-intruded coastal aquifers. Water Resources Research 36: 2155-2165, doi: 10.1029/2000WR900149.

Chiang, W. H. and W. Kinzelbach (1994). PMPATH. An advective transport model for Processing Modflow and Modflow. Geological Survey of Hamburg. Germany.

Chiang, W. H. and W. Kinzelbach (1998). Processing MODFLOW – a simulation system for modelling groundwater flow and pollution. Hamburg. 342pp. <http://www. pmwin.net> (accessed 7 January, 2017).

Clarke, D. S., V. Berens and K. J. Dennis (2003). Uley South – Coffin Bay observation well network review. Department of Water, Land and Biodiversity Conservation. Report 2003/04. Government of South Australia. Adelaide. 118pp.

Clarke, D. S. (2005). Uley South observation well network review. Department of Water, Land and Biodiversity Conservation. Report 2005/06. Government of South Australia. Adelaide. 69pp.

Cobaner, M., R. Yurtal, A. Dogan and L. H. Motz (2012). Three dimensional simulation of seawater intrusion in coastal aquifers: A case study in the Goksu Deltaic Plain. Journal of Hydrology 464: 262-280, doi: 10.1016/j.jhydrol.2012.07.022.

Collins, M. A. (1971). Seawater intrusion in layered aquifers. Water Resources Research 7: 971-979.

Conte, S. D. and C. De Boor (1972). Elementary Numerical Analysis. McGraw-Hill. New York. 396pp.

Cook, S., P. Dixon-Jain, M. Hocking, B. Sundaram, L. K. Morgan, K. M. Ivkovic, A. D. Werner, R. Norman, L. Caruana and N. Garlapati (2013). A national-scale vulnerability assessment of SWI intrusion: Vulnerability Factor Analysis. Record 2013/08. Geoscience Australia Canberra and National Centre for Groundwater Research and Training. Adelaide.

Custodio, E. (2010). Coastal aquifers of Europe: an overview. Hydrogeology Journal 18: 269-280, doi: 10.1007/s10040-009-0496-1.

Dagan, G. and D. G. Zeitoun (1998). Seawater-freshwater interface in a stratified aquifer of random permeability distribution. Journal of Contaminant Hydrology 29: 185-203, doi: 10.1016/S0169-7722(97)00013-2.

Dausman, A.M., C. Langevin, M. Bakker and F. Schaars (2010). A comparison between SWI and SEAWAT - the importance of dispersion, inversion and vertical anisotropy. In proceedings: de Melo M. T. C., L. Lebbe, J. V. Cruz, R. Coutinho, C. Langevin and A. Buxo (Eds) SWIM21 21st Salt Water Intrusion Meeting. 21-25 June 2010. Azores. Portugal. ISBN: 978-972-97711-5-6, http://www.swim-site.nl/pdf/swim21/pages_271_274.pdf.

Davis, A., T. Munday and N. Somaratne (2013). Characterisation of a coastal aquifer system in the Eyre Peninsula, South Australia, using nuclear magnetic resonance methods. Groundwater in the Coastal Zones of the Asia-Pacific. Coastal Research Library 7: 89-120, doi: 10.1007/978-94-007-5648-9_6.

De Marsily, G.H., G. Lavedan, M. Boucher and G. Fasanino (1984). Interpretation of interference tests in a well field using geostatistical techniques to fit the permeability distribution in a reservoir model. In: Verly, G. et al. (Eds.). Geostatistics for natural resources characterization. Part 2. D. Reidel Pub. Co.

Doherty, J. (2013). Manual and Addendum for PEST: Model-Independent Parameter Estimation. Watermark Numerical Computing. Brisbane. Australia.

Dose, E. J., L. Stoeckl, G. J. Houben, H. L. Vacher, S. Vassolo, J. Dietrich and T. Himmelsbach (2014). Experiments and modeling of freshwater lenses in layered aquifers: Steady state interface geometry. Journal of Hydrology 509: 621-630, doi: 10.1016/j.jhydrol.2013.10.010.

Essaid, H. I. (1990). A multilayered sharp-interface model of coupled freshwater and saltwater flow in coastal systems: model development and application. Water Resources Research 16: 1431-1454.

Evans, S. L. (1997). Estimating long term recharge to thin, unconfined carbonate aquifers using conventional and environmental isotope techniques: Eyre Peninsula, South Australia. Incomplete MSc Thesis. Flinders University. Adelaide. 176pp.

Evans, R. S., N. Merrick and G. Gates (2004). Groundwater level response management-Strengths, weaknesses and opportunities. In: Balancing the basin,

the 9th Murray-Darling basin groundwater workshop 2004, Bendigo, 17-19 February 2004.

Ferguson, G. and T. Gleeson (2012). Vulnerability of coastal aquifers to groundwater use and climate change. Natural Climate Change 2: 342-345, doi: 10.1038/nclimate1413.

Feseker, T. (2007). Numerical studies on saltwater intrusion in a coastal aquifer in northwestern Germany. Hydrogeology Journal 15: 267-279, doi: 10.1007/s10040-006-0151-z.

Fetter, C. W. (2001). Applied hydrogeology. Fourth ed. Prentice Hall Inc. New Jersey. 598pp.

Fitts, C. R., J. Godwin, K. Feiner, C. McLane and S. Mullendore (2014). Analytic element modeling of steady interface flow in multilayer aquifers using AnAqSim. Ground Water 53: 432-439, doi: 10.1111/gwat.12225.

Fitzpatrick, A., K. Cahill and T. Munday (2009). Informing the hydrogeology of Coffin Bay, South Australia, through the constrained inversion of TEMPEST AEM Data. CSIRO. Adelaide. 159 pp.

Freeze, A. R. and J. A. Cherry (1979). Groundwater. Prentice-Hall Inc. Englewood Cliffs. New Jersey.

Glover, R. E. (1959). The pattern of freshwater flow in a coastal aquifer. Journal of Geophysical Research 64: 457-459.

Goswami, R. R. and T. P. Clement (2007). Laboratory-scale investigation of saltwater intrusion dynamics. Water Resources Research 43: 1-11, doi: 10.1029/2006WR005151.

Guo, W. and C. D. Langevin (2002). User's Guide to SEAWAT: A computer program for simulation of three-dimensional variable-density ground-water flow. USGS Techniques of Water Resources Investigations Book 6. Chapter A7.

Harbaugh, A.W., E. R. Banta, M. C. Hill and M. G. McDonald (2000). MODFLOW-2000, the U.S. Geological Survey modular ground-water model – User guide to modularisation concepts and ground-water flow process. U.S. Geological Survey open-file report 00-92. Reston. 130pp.

Harrington, N., S. Evans and D. Zulfic (2006). Uley Basin groundwater modelling project. Project overview and conceptual model development. Volume 1.

Department of Water, Land and Biodiversity Conservation. Report 2006/01. Government of South Australia. Adelaide. 116pp.

Henry, H. R. (1964). Effects of dispersion on salt encroachment in coastal aquifers. Sea Water in Coastal Aquifers. US Geological Survey Water Supply Paper 1613 – C: 70-84.

Held, R., S. Attinger and W. Kinzelbach (2005). Homogenization and effective parameters for the Henry problem in heterogeneous formations. Water Resources Research 41: 1-14, doi: 10.1029/2004WR003674.

Hunt, R. J., J. Luchette, W. A. Schreuder, J. O. Rumbaugh, J. Doherty, M. J. Tonkin and D. B. Rumbaugh (2010). Using a cloud to replenish parched groundwater modelling efforts. Ground Water 48: 360-365, doi: 10.1111/j.1745-6584.2010.00699.x.

Huyakorn, P. S., Y. S. Wu and N. S. Park (1996). Multiphase approach to the numerical solution of a sharp-interface saltwater intrusion problem. Water Resource Research 32: 93-102, doi: 10.1029/95WR02919.

Ibrahimi, M. K., T. Miyazaki, T. Nishimura and H. Imoto (2014). Contribution of shallow groundwater rapid fluctuation to soil salinization under arid and semiarid climate. Arabian Journal Geoscience 7: 3901-3911, doi: 10.1007/s12517-013-1084-1.

Intergovernmental Panel on Climate Change (IPCC) (2008). Climate change and water. IPCC Technical paper VI, http://www.ipcc.ch/ (accessed September 22, 2014).

Johnson, A. I. (1967). Specific yield: compilation of specific yields for various materials. USGS Open-FileReport. Albuquerque. 119pp, http://pubs.usgs.gov/wsp/1662d/ (accessed July 10, 2015).

Jakovovic, D., A. D. Werner and C. T. Simmons (2011). Numerical modelling of saltwater up-coning: Comparison with experimental laboratory observations. Journal of Hydrology 402: 261-273, doi: 10.1016/j.jhydrol.2011.03.021.

Jakovovic, D., V. E. A. Post, A. D. Werner, O. Männicke, J. L. Hutson and C. T. Simmons (2012). Tracer adsorption in sand-tank experiments of saltwater up-coning. Journal of Hydrology 414: 476-481, doi:10.1016/j.jhydrol.2011.11.024.

Kerrou, J. and P. Renard (2010). A numerical analysis of dimensionality and heterogeneity effects on advective dispersive seawater intrusion processes. Hydrogeology Journal 18: 55-72, doi: 10.1007/s10040-009-0533-0.

Klute, A. and C. Dirksen (1986). Hydraulic conductivity and diffusivity: laboratory methods. In: Methods of Soil Analysis, Part 1, Physical and Mineralogical Methods, Agronomy Monograph. Second edition. American Society of Agronomy and Soil Science Society of America 9: 687–734. Madison. Wisconsin. USA.

Knowling, M. J., A. D. Werner and D. Herckenrath (2015). Quantifying climate and pumping contributions to aquifer depletion using a highly parameterised groundwater model: Uley South Basin (South Australia). Journal of Hydrology 523: 515-530, doi: 10.1016/j.jhydrol.2015.01.081.

Koch, M. and G. Zhang (1970). Numerical modeling and management of saltwater seepage from coastal brackish canals in southeast Florida. WIT Transactions on Ecology and the Environment 25, doi: 10.2495/CENV980371.

Konz, M., P. Ackerer, A. Younes, P. Huggenberger and E. Zechner (2009). Two-dimensional stable-layered laboratory-scale experiments for testing density-coupled flow models. Water Resources Research 45, doi: 10.1029/2008WR007118.

Koussis, A. D., K. Mazi and G. Destouni (2012). Analytical single-potential, sharp-interface solutions for regional seawater intrusion in sloping unconfined coastal aquifer, with pumping and recharge. Journal of Hydrology 416: 1-11, doi: 10.1016/j.jhydrol.2011.11.012.

Kouzana, L., A. B. Mammou, and M. S. Felfoul (2009). Seawater intrusion and associated processes: case of the Korba aquifer (Cap-Bon, Tunisia). Comptes Rendus Geoscience 341: 21-35, doi: 10.1016/j.crte.2008.09.008.

Langevin, C. D., W. B. Shoemaker and W. Guo (2003). MODFLOW-2000, the US geological survey modular ground-water model-documentation of the SEAWAT-2000 version with the variable-density flow process (VDF) and the Integrated MT3DMS transport process (IMT). USGS Department of the Interior. http://fl.water.usgs.gov/PDF_files/ofr03_426_langevin.pdf (accessed April 13, 2016).

Langevin, C. D., D. T. Thorne Jr., A. M. Dausman, M. C. Sukop and W. Guo (2008). SEAWAT Version 4: a computer program for simulation of multi-species solute and heat transport (No. 6-A22). USGS Department of the Interior. http://pubs.usgs.gov/tm/tm6a22/pdf/tm6A22.pdf (accessed April 13, 2016).

Li, C. (2008) Water use by Malle-form Eucalyptus diversifolia in a semi-arid and karstic environment. Unpublished honours thesis. Flinders University. Adelaide. 65pp.

Lin, J., J. B. Snodsmith, C. Zheng and J. Wu (2009). A modelling study of seawater intrusion in Alabama Gulf Coast, USA. Environmental Geology 57: 119-130, doi: 10.1007/s00254-008-1288-y.

Liu, Y., X. Mao, J. Chen and D. A. Barry (2014). Influence of a coarse interlayer on seawater intrusion and contaminant migration in coastal aquifers. Hydrological Processes 28: 5162-5175, doi: 10.1002/hyp.10002.

Lu, C., P. K. Kitanidis and J. Luo (2009). Effects of kinetic mass transfer and transient flow conditions on widening mixing zones in coastal aquifers.Water Resources Research 45: 1-17, doi: 10.1029/2008WR007643.

Lu, C. and A. D. Werner (2013). Timescales of seawater intrusion and retreat. Advances in Water Resources 59: 39-51, doi: 10.1016/j.advwatres.2013.05.005.

Lu, C., Y. Chen, C. Zhang and J. Luo (2013). Steady-state freshwater–seawater mixing zone in stratified coastal aquifers. Journal of Hydrology 505: 24-34, doi: 10.1016/j.jhydrol.2013.09.017.

Luyun Jr, R., K. Momii and K. Nakagawa (2009). Laboratory-scale saltwater behaviour due to subsurface cut-off wall. Journal of Hydrology 377: 227-236, doi: 10.1016/j.jhydrol.2009.08.019.

Mahesha, A. (1995). Parametric studies on the advancing interface in coastal aquifers due to linear variation of the freshwater level. Water Resources Research 31: 2437-2442, doi: 10.1029/95WR02040.

Mahesha, A. (2001). Effect of strip recharge on sea water intrusion into aquifers. Hydrological Sciences 46: 199-210, doi: 10.1080/02626660109492816.

Mantoglou, A. (2003). Pumping management of coastal aquifers using analytical models of saltwater intrusion. Water Resources Research 39, doi: 10.1029/2002WR001891.

Mehdizadeh, S. S., A. D. Werner, F. Vafaie and S. Badaruddin (2014). Vertical leakage in sharp-interface seawater intrusion models of layered coastal aquifers. Journal of Hydrology 519: 1097-1107, doi: 10.1016/j.jhydrol.2014.08.027.

Michael, H. A., A. E. Mulligan and C. F. Harvey (2005). Seasonal oscillations in water exchange between aquifers and the coastal ocean. Nature 436: 1145-1148, doi: 10.1038/nature03935.

Morgan, L. K., A. D. Werner and C. T. Simmons (2012). On the interpretation of coastal aquifer water level trends and water balances: A precautionary note. Journal of Hydrology 470: 280-288, doi: 10.1016/j.jhydrol.2012.09.001.

Morgan, L. K., A. D. Werner, K. M. Ivkovic, H. Carey and B. Sundaram (2013a). A national-scale vulnerability assessment of seawater intrusion: First-order assessment of seawater intrusion for Australian case study sites. Record 2013/19. Geoscience Australia, Canberra and National Centre for Groundwater Research and Training. Adelaide.

Morgan, L. K., A. D. Werner, M. J. Morris and M. D. Teubner (2013b). Application of a rapid-assessment method of SWI: Willunga Basin, South Australia. In: Wetzelhuetter. Groundwater in the Coastal Zones of Asia-Pasific 7: 1-30, doi: 10.1007/978-94-007-5648-9_10.

Morgan, L. K., L. Stoeckl, A. D. Werner and V. E. Post (2013c). An assessment of seawater intrusion overshoot using physical and numerical modeling. Water Resources Research 49: 6522-6526, doi: 10.1002/wrcr.20526.

Morgan, L. K. and A. D. Werner (2015). A national inventory of seawater intrusion vulnerability for Australia. Journal of Hydrology: Regional Studies 4: 686-698, doi: 10.1016/j.ejrh.2015.10.005.

Morgan, L. K., M. Bakker and A. D. Werner (2015). Occurrence of seawater intrusion overshoot. Water Resources Research 51: 1989-1999, doi: 10.1002/2014WR016329.

Morton, W. H. and T. M. Steel (1968). Eyre Peninsula groundwater study Uley South Basin. Progress report No. 1 – Aquifer Evaluation. Department of Mines. Report 66/45. Government of South Australia. Adelaide.

Mualem, Y. and J. Bear (1974). The shape of the interface in steady flow in a stratified aquifer. Water Resources Research 10: 1207-1215, doi: 10.1029/WR010i006p01207.

Naff, R. L. and E. R. Banta (2008). The U.S. Geological Survey modular ground-water model-PCGN: a preconditioned conjugate gradient solver with improved nonlinear control. U.S. Geological Survey Open-File Report 2008. 44pp.

Natural Resources Committee (NRC) (2013). Eyre Peninsula water supply: Final report ‘‘Under the lens’’. Parliament of South Australia. Adelaide. 233pp.

Ogata, A. and R. B. Banks (1961). A solution of the differential equation of longitudinal dispersion in porous media. USGS Professional Paper 411-A, http://pubs.er.usgs.gov/publication/pp411A/ (accessed October 22, 2014).

Ojuri, O. and S. Ola (2010). Estimation of contaminant transport parameters for a tropical sand in a sand tank model. International Journal of Environmental Science and Technology 7: 385-394, doi: 10.1007/BF03326148.

Ordens, C. M., A. D. Werner, V. E. A. Post, J. L. Hutson, C. T. Simmons and B. M. Irvine (2012). Groundwater recharge to a sedimentary aquifer in the topographically closed Uley South Basin, South Australia. Hydrogeology Journal 20: 61-72, doi: 10.1007/s10040-011-0794-2.

Paniconi, C., I. Khlaifi, G. Lecca, A. Giacomelli and J. Tarhouni (2001). Modeling and analysis of seawater intrusion in the coastal aquifer of eastern Cap-Bon, Tunisia. Transport in porous media 43: 3-28, doi: 10.1023/A:1010600921912.

Pistiner, A. and M. Shapiro (1993). A model for a moving interface in a layered coastal aquifer. Water Resources Research 29: 329-340, doi: 10.1029/92WR01901.

Post, V. E. A., A. Vandenbohede, A. D. Werner, Maimun and M. D. Teubner (2013). Groundwater ages in coastal aquifers. Advances in Water Resources 57: 1-11, doi: 10.1016/j.advwatres.2013.03.011.

Prathapar, S. A., C. W. Robbins, W. S. Meyer and N. Jayawardane (1992). Models for estimating capillary rise in a heavy clay soil with a saline shallow water table. Irrigation Science 13: 1-7, doi: 10.1007/BF00190238.

Rumbaugh, J. O. and D. B. Rumbaugh (2007). Groundwater Vista. Reinholds. Pennsylvania: Environmental Solutions Inc. www.groundwatermodels.com. (accessed 7 January, 2017).

Schincariol, R. A. and F. W. Schwartz (1990). An experimental investigation of variable density Ffow and mixing in homogeneous and heterogeneous media. Water Resources Research 26: 2317-2329, doi: 10.1029/WR026i010p02317.

Schincariol, R. A. (1998). Dispersive mixing dynamics of dense miscible plumes: natural perturbation initiation by local-scale heterogeneities. Journal of Contaminant Hydrology 34: 247-271, doi: 10.1016/S0169-7722(98)00081-3.

Sebben, M. L., A. D. Werner and T. Graf (2015). Seawater intrusion in fractured coastal aquifers: A preliminary numerical investigation using a fractured Henry problem, Advances in Water Resources 85: 93-108, doi: 10.1016/j.advwatres.2015.09.013.

Shammas, M. I. and G. Jacks (2007). Seawater intrusion in the Salalah plain aquifer, Oman. Environmental Geology 53: 575-587, doi: 10.1007/s00254-007-0673-2.

Sherif, M. M. and V. P. Singh (1999). Effect of climate change on sea water intrusion in coastal aquifer. Hydrological Processes 13: 1277-1287, doi: 10.1002/(SICI)1099-1085(19990615)13:8<1277::AID-HYP765>3.0.CO;2-

Shi, L., L. Cui, N. Park and P. S. Huyakorn (2011). Applicability of a sharp-interface model for estimating steady-state salinity at pumping wells-validation against sand tank experiment. Journal of Contaminant Hydrology 124: 35-42, doi: 10.1016/j.jconhyd.2011.01.005.

Sibenaler, X. P (1976). Eyre Peninsula Groundwater Survey Uley South Basin. Progress Report No. 4: Aquifer Evaluation. Report book 76/30. South Australian Department of Mines. Adelaide. Australia.

Simmons, C. T., M. L. Pierini and J. L. Hutson (2002). Laboratory investigation of variable density flow and solute transport in unsaturated-saturated porous media. Transport in Porous Media 47: 215-244, doi: 10.1023/A:1015568724369.

Simpson, M. J. and T. P. Clement (2003). Theoretical analysis of the worthiness of henry and elder problems as benchmarks of density-dependent groundwater flow models. Advances in Water Resources 26: 17-31, doi: 10.1016/S0309-1708(02)00085-4.

Smith, A. J. (2004). Mixed convection and density-dependent seawater circulation in coastal aquifers. Water Resources Research 40: 1-16, doi: 10.1029/2003WR002977.

Vázquez-Suñé, E., E. Abarca, J. Carrera, B. Capino, D. Gámez, M. Pool, T. Simó, F. Batlle, J. M. Niñerola and X. Ibáñez (2006). Groundwater modelling as a tool for the European Water Framework Directive (WFD) application: the Llobregat case. Physics and Chemistry of the Earth 31: 1015-1029, doi:10.1016/j.pce.2006.07.008.

Verruijt, A. (1968). A note on the Ghyben-Herzberg formula. IASH Bulletin 13: 43-45.

Voss, C. I. and W. R. Souza (1987). Variable density flow and solute transport simulation of regional aquifers containing a narrow freshwater-saltwater transition zone. Water Resources Research 23: 1851-1866, doi: 10.1029/WR023i010p01851.

Ward, J. D., A. D. Werner and B. Howe (2009). Saltwater intrusion in Southern Eyre Peninsula. Report developed through the Eyre Peninsula Groundwater. Allocation and Planning Project. Government of South Australia. Eyre Peninsula Natural Resources Management Board. 56pp.

Watson, T. A., A. D. Werner and C. T. Simmons (2010). Transience of seawater intrusion in response to sea-level rise. Water Resources Research 46: 1-10, doi: 10.1029/2010WR009564.

Webb, M. D. and K. W. Howard (2011). Modelling the transient response of saline intrusion to rising sea-levels. Ground Water 49: 560-569, doi: 10.1111/j.1745-6584.2010.00758.x.

Werner, A. D. and D. A. Lockington (2004). The potential for soil salinization above aquifers impacted by seawater intrusion. In proceedings. 13th International Soil Conservation Organisation Conference: Conserving Soil and Water for Society: Sharing Solutions (Eds. Raine S. R, A. J. W. Biggs, N. W. Menzies, D. M. Freebairn and P.E. Tolmie). 4-9 July. Brisbane. ASSSI/IECA. Paper 790. 6pp.

Werner, A. D. and D. A. Lockington (2006). Tidal impacts on riparian salinities near estuaries. Journal of Hydrology 328: 511-22, doi: 10.1016/j.jhydrol.2005.12.011.

Werner, A. D. and M. R. Gallagher (2006). Characterisation of sea-water intrusion in the Pioneer Valley, Australia using hydrochemistry and three-dimensional numerical modelling. Hydrogeology Journal 14: 1452-1469, doi: 10.1007/s10040-006-0059-7.

Werner, A. D. and C. T. Simmons (2009). Impact of sea-level rise on sea water intrusion in coastal aquifers. Ground Water 47: 197-204, doi: 10.1111/j.1745-6584.2008.00535.x.

Werner, A. D., D. Jakovovic and C. T. Simmons (2009). Experimental observations of saltwater up-coning. Journal of Hydrology 373: 230-241, doi: 10.1016/j.jhydrol.2009.05.004.

Werner, A. D. (2010). A groundwater flow model of Uley South Basin, South Australia. Draft report prepared for the Eyre Peninsula Natural Resource Management Board by Flinders University. Adelaide. 105pp.

Werner, A. D., D. W. Alcoe, C. M. Ordens, J. L. Hutson, J. D. Ward and C. T. Simmons (2011). Current practice and future challenges in coastal aquifer management: flux-based and trigger-level approaches with application to an Australian case study. Water Resources Management 25:1831-1853, doi: 10.1007/s11269-011-9777-2.

Werner, A. D., J. D. Ward, L. K. Morgan, C. T. Simmons, N. I. Robinson and M. D. Teubner (2012). Vulnerability indicators of sea water intrusion. Ground Water 50: 48-58, doi: 10.1111/j.1745-6584.2011.00817.x.

Werner, A. D. and L. D. Dang (2013). Three-Dimensional Seawater Intrusion Modelling of Uley South Basin, South Australia. In Groundwater in the Coastal Zones of Asia-Pacific. Springer Netherlands, doi: 10.1007/978-94-007-5648-9_9.

Werner, A. D., M. Bakker, V. E. Post, A. Vandenbohede, C. Lu, B. Ataie-Ashtiani, C. T. Simmons and D. A. Barry (2013). Seawater intrusion processes, investigation and management: recent advances and future challenges. Advances in Water Resources 51: 3-26, doi: 10.1016/j.advwatres.2012.03.004.

Werner, A. D., Q. Zhang, L. Xue, B. D. Smerdon, X. Li, L. Yu, L. Li (2013b) An initial inventory and indexation of groundwater mega-depletion cases. Water Resources Management 27, 507-533, doi: 10.1007/s11269-012-0199-6.

Werner, A. D. (2014). Karst Aquifer Recharge: Comments on Somaratne, N. Characteristics of Point Recharge in Karst Aquifers. Water 6: 3727-3738, doi: 10.3390/w6123727.

Wu, J., Y. Xue, P. Liu, J. Wang, Q. Jiang and H. Shi (1993). Sea-water intrusion in the coastal Area of Laizhou Bay, China: 2. Sea-water intrusion monitoring. Ground Water 31: 740-745, doi: 10.1111/j.1745-6584.1993.tb00584.x.

Yakirevich, A., A. Melloul, S. Sorek, S. Shaath and V. Borisov (1998). Simulation of seawater intrusion into the Khan Yunis area of the Gaza Strip coastal aquifer. Hydrogeology Journal 6: 549-559, doi: 10.1007/s100400050175.

Zhang, Q., R. E. Volker and D. A. Lockington (2002). Experimental investigation of contaminant transport in coastal groundwater. Advances in Environmental

Research 6: 229-237, doi: 10.1016/S1093-0191(01)00054-5.

Zulfic, D., N. Harrington and S. Evans (2007). Uley basin groundwater modelling project. Groundwater flow model volume 2. Department of Water. Land and Biodiversity Conservation. Report DWLBC 2007/04. Government of South Australia. Adelaide. 128pp.

APPENDICES

Appendix 4.A. The values of linear regression and determination coefficient in Figure 4.10

Figure	FHD Δh_f	Number of data points	a	b	R^2
(-)	m	(-)	(-)	(-)	(-)
4.10a	2.00	3	-0.10	10.7	0.99
	2.50	4	2.42	9.48	0.99
	3.00	5	2.62	9.67	0.99
	3.50	6	3.17	9.48	0.99
	4.00	6	3.94	8.99	0.99
4.10b	2.00	3	0.73	12.4	0.99
	2.50	4	2.48	11.7	0.99
	3.00	5	3.43	11.3	0.99
	3.50	6	3.96	11.1	0.99
	4.00	6	4.61	10.7	0.99
4.10c	2.00	3	-11.5	48.9	0.98
	2.50	4	-4.37	44.1	0.97
	3.00	5	-0.50	41.3	0.97
	3.50	6	1.74	39.7	0.97
	4.00	6	2.21	39.5	0.97

Appendix 4.B. Passive SWI cases (at the initial steady-state and the second steady-state conditions after FHD)

Case	Initial θ (50% contour)	Final θ (50% contour)	Initial x_{toe} (50% contour)	Final x_{toe} (50% contour)	Initial W_{toe}	Final W_{toe}	Initial *Pe*	Final *Pe*	Initial *MCR*	Final *MCR*	Initial A_{SWI}	Final A_{SWI}	Initial Q_f	Final Q_f
1	9.240	4.290	169.0	386.2	31.50	130.2	0.009930	0.01034	0.06771	0.02486	0.000630	0.000251	0.54167	0.19265
5	9.240	4.290	169.0	386.2	31.50	130.2	0.009980	0.01047	0.06771	0.02325	0.000633	0.000254	0.27083	0.09635
9	9.240	4.290	169.0	386.2	31.50	130.2	0.009910	0.01027	0.06771	0.02486	0.000628	0.000249	1.08333	0.38537
13	8.310	3.530	198.6	470.5	8.000	45.00	0.001030	0.001154	0.06771	0.02486	0.0000660	0.0000280	0.54167	0.19268
17	17.20	9.540	92.50	186.5	94.50	183.0	0.09887	0.1021	0.06771	0.02486	0.00627	0.00248	0.54167	0.19273
21	12.23	5.760	131.5	292.5	21.40	81.00	0.009920	0.01032	0.08854	0.03471	0.000808	0.000346	0.56667	0.21521
25	8.050	3.440	208.5	490.5	44.50	193.0	0.009930	0.01035	0.05382	0.01829	0.000507	0.000186	0.51667	0.17016
29	9.710	4.790	140.2	286.7	27.20	79.20	0.01135	0.01184	0.06513	0.02886	0.000694	0.000332	0.45594	0.19480
33	9.120	3.730	190.1	475.2	34.50	187.4	0.008830	0.009170	0.06178	0.02254	0.000514	0.000202	0.55603	0.19719
37	9.240	4.290	169.0	386.2	31.50	130.2	0.009920	0.01031	0.06771	0.02486	0.000629	0.000250	0.54171	0.19270
41	9.240	4.290	169.0	386.2	31.50	130.2	0.009940	0.01036	0.06771	0.02486	0.000630	0.000251	0.54164	0.19260

Appendix 4.C. Active SWI cases (at 15 y after FHD)

Case	θ (50% contour)	x_{toe} (95% contour)	x_{toe} (50% contour)	x_{toe} (5% contour)	x_{tip} (95% contour)	x_{tip} (50% contour)	x_{tip} (5% contour)	W_{toe}	W_{tip}	Pe	A_{SWI}	MCR	Q_f
2	4.110	280.2	410.6	450.4	0.0	0.0	27.80	170.2	27.80	0.01077	0.000159	0.01502	0.11265
3	3.460	373.3	547.5	611.3	31.50	59.20	165.8	238.0	134.3	0.01097	0.000584	0.05626	0.40790
4	3.890	481.1	692.8	778.8	203.6	273.4	479.8	297.7	276.2	0.01133	0.00102	0.09902	0.69314
6	7.990	183.2	210.2	290.8	0.0	0.0	10.60	107.6	10.60	0.01099	0.000163	0.01502	0.05634
7	4.750	265.2	375.0	412.8	0.0	8.800	30.60	147.6	28.60	0.01103	0.000588	0.05626	0.20395
8	4.720	384.5	495.0	612.1	140.0	150.3	346.6	227.6	206.6	0.01137	0.00102	0.09901	0.34657
10	3.620	372.0	502.5	645.8	0.00	36.00	58.10	273.8	58.10	0.01065	0.000158	0.01502	0.22523
11	3.120	470.4	730.2	825.2	124.9	184.5	410.0	354.8	285.1	0.01094	0.000583	0.05626	0.81581
12	4.100	580.3	823.2	993.1	270.0	470.5	668.1	412.8	398.1	0.01131	0.00102	0.09902	1.38634
14	3.660	436.0	460.7	492.8	0.0	0.0	13.80	56.80	13.80	0.001283	1.898E-5	0.01502	0.11262
15	2.700	578.6	650.7	665.5	15.30	25.60	49.10	86.90	33.90	0.001154	6.145E-5	0.05626	0.40792
16	2.620	730.1	800.7	876.9	167.0	177.0	240.0	146.8	73.80	0.001167	0.000105	0.09902	0.69319
18	6.070	40.00	282.8	320.6	0.0	5.000	226.1	280.6	226.1	0.1056	0.00156	0.01502	0.11262
19	11.28	140.1	362.8	530.8	74.60	214.9	461.4	390.6	386.8	0.1091	0.00581	0.05626	0.40785
20	45.71	237.3	452.8	723.9	226.0	425.0	710.2	486.6	484.2	0.1129	0.0102	0.09902	0.69315
22	4.350	251.2	387.8	394.2	0.0	0.0	20.00	143.0	20.00	0.01083	0.000160	0.01502	0.09009
23	3.840	347.3	497.8	552.3	34.90	58.10	155.1	205.0	120.1	0.01097	0.000684	0.06645	0.38538
24	4.100	460.0	687.8	720.5	207.1	290.2	447.0	260.5	234.0	0.01133	0.00121	0.1198	0.67065
26	3.630	307.2	464.8	508.5	0.0	0.0	31.00	201.3	31.00	0.01073	0.000159	0.01502	0.13514
27	3.160	397.2	594.8	668.6	30.30	61.00	182.0	271.3	151.7	0.01096	0.000517	0.04947	0.43043
28	3.180	502.1	814.8	836.0	203.4	301.0	512.0	333.9	308.6	0.01133	0.000890	0.08520	0.71569
30	4.130	240.2	360.0	390.0	0.0	0.0	21.00	150.0	21.00	0.01238	0.000225	0.01850	0.12025
31	3.520	313.2	470.0	534.2	30.00	51.00	160.0	221.0	130.0	0.01271	0.000810	0.06809	0.42555
32	3.740	418.4	650.0	688.4	205.2	268.0	425.2	270.0	220.0	0.01321	0.00142	0.1201	0.72082
34	3.990	310.3	480.0	520.3	0.0	0.0	31.00	210.0	31.00	0.009502	0.000141	0.01507	0.12813
35	3.390	431.3	610.0	680.3	35.1	62.00	159.1	249.0	124.0	0.009641	0.000492	0.05375	0.44344
36	3.720	514.6	817.5	854.6	200.0	302.0	500.0	340.0	300.0	0.009917	0.000849	0.09359	0.74873
38	3.590	337.5	480.0	537.5	0.0	10.00	35.00	200.0	35.00	0.01073	0.000159	0.01502	0.11268
39	3.380	426.5	634.0	715.5	65.20	100.0	271.2	288.5	206.0	0.01096	0.000584	0.05626	0.40792
40	3.400	543.0	750.0	888.0	270.5	355.0	600	345.0	329.5	0.01133	0.00102	0.09902	0.69317
42	7.670	200.0	219.0	315.0	0.0	0.0	15.0	115.0	15.0	0.01081	0.000160	0.01502	0.11262

43	4.270	332.6	482.0	535.6	10.0	25.0	60.0	203.0	50.0	0.01098	0.000585	0.05626	0.40788
44	3.260	436.3	510.0	696.3	159.0	213.0	384.0	260.0	225.0	0.01134	0.00102	0.09902	0.69312
45	3.380	337.1	503.4	562.3	0.0	4.0	45.0	225.2	45.0	0.01081	0.000411	0.03955	0.29167
46	4.840	235.0	336.5	363.2	0.0	0.0	12.2	128.2	12.2	0.01099	5.971E-5	0.00546	0.04167
47	5.090	232.5	331.5	356.5	0.0	0.0	12.0	124	12	0.01099	5.971E-5	0.00546	0.04167
48	4.220	275.4	400.0	438.2	0.0	0.0	26.0	162.8	26	0.01077	0.000159	0.01502	0.11265
49	3.550	325.3	478.0	530.1	0.0	3.0	39.0	204.8	39	0.01081	0.000411	0.03955	0.29167
50	3.400	385.5	572.6	644.2	39.00	68.0	194.3	258.7	155.3	0.01097	0.000584	0.05626	0.40790
51	3.530	437.5	645.0	728.6	125.0	179.7	367.5	291.1	242.5	0.01114	0.000898	0.08772	0.62500
52	5.140	230.0	328.0	352.5	0.0	0.0	12.6	122.5	12.6	0.01099	5.971E-5	0.00546	0.04167
53	4.290	272.0	393.5	431.0	0.0	0.0	25.3	159	25.3	0.01077	0.000159	0.01502	0.11265
54	3.640	319.8	466.5	516.0	0.0	3.0	37.5	196.2	37.5	0.01081	0.000411	0.03955	0.29167
55	3.790	494.0	718.5	814.0	217.5	288.0	515.0	320	297.5	0.01133	0.00102	0.09902	0.69314
56	5.000	229.5	326.0	350.7	0.0	0.0	12.7	121.2	12.7	0.01099	5.971E-5	0.00546	0.04167
57	4.180	269.2	391.0	426.5	0.0	0.0	24.3	157.3	24.3	0.01077	0.000159	0.01502	0.11265
58	3.740	315.5	459.6	508.3	0.0	1.0	36.5	192.8	36.5	0.01081	0.000411	0.03955	0.29167
59	3.460	367.0	535.5	597.4	28.00	47.0	144.1	230.4	116.1	0.01097	0.000584	0.05626	0.40790
60	5.030	228.5	324.0	349.0	0.0	0.0	11.5	120.5	11.5	0.01099	5.971E-5	0.00546	0.04167
61	4.210	268.0	387.5	424.0	0.0	0.0	23.4	156	23.4	0.01077	0.000159	0.01502	0.11265
62	3.780	313.2	456.4	504.0	0.0	2.0	35.5	190.8	35.5	0.01081	0.000411	0.03955	0.29167
63	3.530	363.0	528.0	588.5	25.00	45.0	135.0	225.5	110.0	0.01097	0.000584	0.05626	0.40790
64	3.610	418.5	606.7	678.5	108.0	154.5	317.0	260	209	0.01114	0.000898	0.08772	0.62500
65	9.210	1613	2700	3725	1517	2475	3625	2112	2108	0.08736	0.00311	0.03691	5.5455

Appendix 4.D. The values of linear regression and determination coefficient in Figure 4.12

Figure	FHD Δh_f	Number of data points	a	b	R^2
(-)	m	(-)	(-)	(-)	(-)
4.12a	5.40	5	1.43	1.94	0.99
	5.80	5	1.78	1.68	0.99
	6.20	5	2.03	1.44	0.99
	6.60	5	2.25	1.20	0.99
	7.00	5	2.46	0.93	0.99
4.12b	5.40	5	2.43	5.35	0.99
	5.80	5	2.91	4.93	0.99
	6.20	5	3.18	4.61	0.99
	6.60	5	3.40	4.54	0.99
	7.00	5	3.75	4.13	0.99
4.12c	5.40	5	1.63	24.86	0.98
	5.80	5	1.90	24.53	0.98
	6.20	5	2.10	24.23	0.98
	6.60	5	2.34	24.16	0.98
	7.00	5	2.57	23.97	0.98